

EXPERIMENTAL INVESTIGATION OF DYNAMIC DELAMINATION IN
CURVED COMPOSITE LAMINATES

A THESIS SUBMITTED TO
THE GRADUATE SCHOOL OF NATURAL AND APPLIED SCIENCES
OF
MIDDLE EAST TECHNICAL UNIVERSITY

BY

IMREN UYAR

IN PARTIAL FULLFILLMENT OF THE REQUIREMENTS
FOR
THE DEGREE OF MASTER OF SCIENCE
IN
AEROSPACE ENGINEERING

SEPTEMBER 2014

Approval of the thesis:

**EXPERIMENTAL INVESTIGATION OF DYNAMIC DELAMINATION IN
CURVED COMPOSITE LAMINATES**

submitted by **İMREN UYAR** in partial fulfillment of the requirements for the degree
of **Master in Aerospace Engineering Department, Middle East Technical
University** by,

Prof. Dr. Canan Özgen
Dean, Graduate School of **Natural and Applied Sciences**

Prof. Dr. Ozan Tekinalp
Head of Department, **Aerospace Engineering**

Assoc. Prof. Dr. Demirkan Çöker
Supervisor, **Aerospace Engineering Dept., METU**

Examining Committee Members:

Prof. Dr. Altan Kayran
Aerospace Engineering Dept., METU

Assoc. Prof. Dr. Demirkan Çöker
Aerospace Engineering Dept., METU

Prof. Dr. Levend Parnas
Mechanical Engineering Dept., METU

Assoc. Prof. Dr. Melih Papila
Material Science & Engineering Dept., Sabancı Uni.

Assist. Prof. Dr. Ercan Gürses
Aerospace Engineering Dept., METU

Date: 05.09.2014

I hereby declare that all information in this document has been obtained and presented in accordance with academic rules and ethical conduct. I also declare that, as required by these rules and conduct, I have fully cited and referenced all material and results that are not original to this work.

Name, Last name: Imren Uyar

Signature:

ABSTRACT

EXPERIMENTAL INVESTIGATION OF DYNAMIC DELAMINATION IN CURVED COMPOSITE LAMINATES

Uyar, İmren

M.S., Department of Aerospace Engineering

Supervisor: Assoc. Prof. Dr. Demirkan Çöker

September 2014, 121 pages

In the aerospace industry, high demand for lightweight structures is fostering the use of composite laminates in a wide variety of shapes, as primary load carrying elements. However, once a composite laminate takes a highly curved shape, such as an L-shape, high interlaminar stresses induced in the curved region causes dynamic delamination formation. This thesis discusses the experimental investigation of delamination in L-shaped CFRP composite laminates under quasi-static shear loading. An experimental setup is designed to apply pure quasi-static shear loading. Three lay-up configurations are investigated: [0/90] fabric, uni-directional [0] and cross-ply [90/0] CFRP composite laminates. The effect of material lay-up, inner radius and thickness on the failure process is studied. The load displacement curves are recorded and the subsequent dynamic delamination is captured with a million fps high-speed camera. The failed specimens are analyzed under a microscope. A single delamination is found to grow in a single load drop for [0/90] fabric laminate. Multiple delaminations in a single load drop are observed in the failure of the unidirectional laminate whereas a sequential delamination at each discrete load drop is seen in the cross-ply laminate. The geometrical constraints such as the thickness and the inner radius are also found to be affecting the failure process. Delamination in all cases is observed to be propagating in the arms at the intersonic speed of 2200 m/s. This study presents the first known experimental evidence of intersonic delamination in composite laminates.

KEYWORDS: Composite materials, fracture mechanics, delamination, high speed monitoring, dynamic failure.

ÖZ

DİRSEK YAPILI KOMPOZİT LAMİNALARDA GÖRÜLEN DİNAMİK DELAMİNASYONUN DENEYSEL YÖNTEMLERLE İNCELENMESİ

Uyar, İmren

Yüksek Lisans, Havacılık ve Uzay Mühendisliği

Tez Yöneticisi: Doç. Dr. Demirkan Çöker

Eylül 2014, 121 sayfa

Havacılık sektöründe hafif yapılar için oluşan yüksek talep, kompozit malzemenin çeşitli geometrilerde özellikle de birincil yük taşıma elemanlarında kullanımını teşvik etmektedir. Ancak, kompozit laminatlar ile bükümlü bir geometri oluşturulduğunda (örneğin L-şekil), laminatlar arası kavisli bölgede geometriden dolayı oluşan yüksek açma gerilimleri dinamik delaminasyon oluşmasına neden olur. Bu tezde, dinamik delaminasyonun L-sekilli KETP kompozit laminatlarda sanki-statik kesme kuvveti altında deneysel incelemesi yapılmıştır. Sanki-statik yük uygulamak için deneysel düzenek tasarlanmıştır. Deneysel sırasıyla [0/90] dokuma, [0] tek yönlü ve [90/0] çapraz katlı olmak üzere üç farklı dizilimde numuneler incelenmiştir. Dizilim farklılığı, iç çap ve kalınlık parametrelerinin kırılma mekanizması üzerindeki etkisi makroölçekte ve orta ölçekte çalışılmıştır. Dinamik delaminasyon olayı saniyede milyon kare çekebilen bir kamera ile çekilmiş ve karşılık gelen yük-deplasman grafiği kaydedilmiştir. Deneysel yapılmış numuneler mikroskop altında incelenmiştir. [0] tek yönlü laminatlarda tek yük düşüşüne karşılık gelen çoklu delaminasyon gözlenirken, [90/0] çapraz katlı laminatlarda çoklu yük düşüşüne karşılık gelen sıralı delaminasyon oluşumu gözlenmiştir. Kalınlık ve iç çap gibi geometrik değişkenlerin de kırılma mekanizması üzerine etkisi olduğu bulunmuştur. Laminatlardaki çatlak ilerleme hızları yüksek hızlı kamera fotoğrafları kullanılarak hesaplandı. Delaminasyon hızları L-şeklin kollarına doğru intersonik (2200 m/s) düzeylere ulaşmıştır. Bu durum, intersonic delaminasyonun ilk bilinen deneysel kayıdır.

ANAHTAR KELİMELER: Kompozit malzeme, kırılma mekanizması, delaminasyon, yüksek hızlı görüntüleme, dinamik kırılma.

To my family...

ACKNOWLEDGEMENTS

Foremost, I would like to express my sincere gratitude to my advisor Assoc. Prof. Demirkan Çöker for the continuous support of my M. S. study and research, for his patience, motivation, enthusiasm, and immense knowledge. His guidance helped me in all the time of research and writing of this thesis. I also thank for offering me the scholarship opportunities in his groups and leading me working on diverse exciting project. I could not have imagined having a better advisor and mentor for my M. S. study.

Besides my advisor, I would like to thank the rest of my thesis committee: Prof. Altan Kayran, Prof. Levend Parnas, and Assoc Prof. Melih Papila and Assist. Prof. Ercan Gürses , for their encouragement, insightful comments, and hard questions.

I would like to acknowledge the Ministry of Science, Industry and Technology and Turkish Aerospace Industries (TAI) (Grant# 00785.STZ.2011–1) for the financial support of this work.

My sincere thanks also goes to Assist. Prof. Oğuz Uzol for offering me opportunities to work at a great work environment with RUZGEM / METUWIND infrastructure.

In addition, a thank you to Kubilay Demiralan, Irfan Karaali, Emin Erkan Aşık and Ahmet Uyar, who help me during experimental fixture, specimen manufacturing and microscope analysis.

I thank my fellow lab-mates in Coker Lab: Dr. Burak Gözlüklü, Denizhan Yavaş, Miray Aydan Arca, Başar Kütükoğlu and Aydın Amireghbali, for the stimulating discussions, for the sleepless nights we were working together before deadlines, and for all the fun we have had in the last three years. Also I thank my friends in Aerospace Engineering Department: Senem Ayşe Haser, Ezgi Anık, Türküler Seferberoğlu, Caner Kahvecioğlu and Özgür Harputlu. In particular, I am grateful to Merve Karlı (a.k.a ‘Cey’) who has read and commented on my thesis.

My special thank goes to Emre Yılmaz and Miray Aydan Arca who always willing to help, give their best suggestions, cheering me up and stood by me through the good times and the bad.

Last but not the least; I would like to thank my family: my parents Münevver Uyar and İsmail Mazhar Uyar, for giving birth to me at the first place and supporting me spiritually throughout my life.

TABLE OF CONTENTS

ABSTRACT.....	v
ÖZ.....	vi
ACKNOWLEDGEMENTS.....	viii
TABLE OF CONTENTS.....	ix
LIST OF TABLES.....	xii
LIST OF FIGURES.....	xiii
LIST OF SYMBOLS.....	xxvii
ABBREVIATIONS.....	xxxiv
CHAPTERS	
1.INTRODUCTION.....	1
1.1. What is a “composite”?.....	1
1.2. Laminated Composite Material.....	2
1.3. Composite Structures in Aircraft Industry.....	5
1.4. L-Shaped Composite Structures.....	9
1.5. Stress State of an L-shaped Member.....	15
1.6. Delamination Problem in Curved Composite Structures.....	16
1.7. High Speed Monitoring System.....	18
1.8. Scope of the Study.....	20
2.LITERATURE SURVEY.....	21
2.1. Historical Background.....	21

2.1.1. Delamination Problem in L-shaped Structures.....	21
3.METHOD	43
3.1. Material.....	43
3.2. Manufacturing Process of L-beams	46
3.3. Geometry and Laminate Properties	48
3.3.1. Geometry of L-shaped beams.....	48
3.3.2. Calculation of Laminate Properties	49
3.3.3. Material Wave Speed Calculation	52
3.3.4. Error Analysis Method for Velocity Calculation	53
3.4. Fixture and Experimental Setup	54
3.4.1. Fixture Design and Loading Condition	54
3.4.2. Experimental Setup.....	56
3.5. Microstructural Analysis	57
4.EXPERIMENTAL RESULTS	61
4.1. Stress Fields	61
4.2. Experimental Results of [0/90] Fabric Lay-up	63
4.3. Experimental Results of [0] Uni-Directional Lay-up	73
4.4. Experimental Results of [90/0] Cross-ply Lay-up.....	76
4.4.1. Part 1- [90/0] Cross-ply Lay-up with 17 plies and 10 mm inner radius	76
4.4.2. [90/0] Cross-ply Lay-up with 10 mm inner radius and different thicknesses.	83
4.4.3. Part 3 - [90/0] Cross-ply Specimen with 17 Plies and 5mm inner radius	91
5.DISCUSSION.....	95

5.1.	Effect of the Material	95
5.2.	Effect of the Lay-Up	99
5.3.	Effect of Thickness	101
5.4.	Effect of Inner Radius	104
6.	SUMMARY AND CONCLUSIONS	107
6.1.	Summary	107
6.2.	Conclusions.....	108
6.3.	Future Work.....	110
	REFERENCES	113
	APPENDICES	119
A.	MEASUREMENT DETAILS OF EXPERIMENTS.....	119
B.	LOAD-DISPLACEMENT CURVES OF EXPERIMENTS.....	120

LIST OF TABLES

TABLES

Table 1.4.1 Types of composite panel stiffening methods [16].....	14
Table 3.1.1 The laminate orientation and the material type of the specimens used in the experiments.	44
Table 3.1.2 Lamina Properties of the pre-preg materials.....	45
Table 3.3.1 Orientation, ply numbers, and geometrical constraints of specimens using in shear loading experiments.....	49
Table 3.3.2 Laminate properties calculated for three lay-up using in experiments. ...	52
Table 3.3.3 Wave speeds of L-shaped composite laminates.....	53
Table A.1 Measurement details of experiments.....	119

LIST OF FIGURES

FIGURES

Figure 1.2.1 (a) Composite fiber comparison (b) Composite usage of commercial aircrafts [9].	4
Figure 1.2.2 Composite fiber orientation rules [44].	5
Figure 1.3.1 Aircraft components of NASA ACEE program using composite materials [9].	6
Figure 1.3.2 Percentage of total structural weight attributed to composites by years [10].	7
Figure 1.3.3 Evolution of composite applications at Airbus by year and model (By courtesy of AVALON Consultancy Services LTD.).	8
Figure 1.3.4 Composite structure content of the Boeing 787 [10].	8
Figure 1.4.1 Typical transport and fighter airplane wings [16].	10
Figure 1.4.2 (a) Types of skin-stringer panels [16] (b) Closed view of Boeing 787 interior stringer panel [18].	11
Figure 1.4.3 Typical integral stiffened panels [16].	11
Figure 1.4.4 Typical spar cap sections [16].	12
Figure 1.4.5 Typical rib construction [16].	12
Figure 1.4.6 (a) Typical semi-monocoque stiffened shell (L-1001) [17], (b) Typical Interior Frame of Boeing-787 [19], (c) Typical transport skin-stringer panels for different aircraft models [17].	13
Figure 1.4.7 (a) Blade (b) Unsymmetrical bulb (c) J-stiffener (d) I-Stiffener [16].	14
Figure 1.5.1 Types of reaction forces on L-shaped member.	16
Figure 1.6.1 Delamination Initiation Locations [16].	17
Figure 1.6.2 (a) Three fracture modes lead to delamination [23] (b) Potential delamination critical location [16].	17
Figure 1.7.1 High speed camera pictures taken with Photron SA5 camera (a) water balloon explosion (7000fps) (b) Perfume spray (10000fps) (c) Delamination in composite laminate (465000 fps).	19

Figure 2.1.1 The effect of inner radius and bend angle on strength for different lay-ups [31].	22
Figure 2.1.2 (Continued) The effect of inner radius and bend angle on strength for different lay-ups [31].	23
Figure 2.1.3 The effect of the length to thickness ratio on the strength [31].	23
Figure 2.1.4 The effect of stacking sequence on the strength [31].	24
Figure 2.1.5 Possible failure mechanisms of composite curved structures [34].	26
Figure 2.1.6 (a) Loading fixture (b) Delamination pictures taken during experiment [24].	27
Figure 2.1.7 Damage in curved laminate (a) Layup-A (b) Layup-B [21].	29
Figure 2.1.8 Single-L structure positioned between rib and base [35].	31
Figure 2.1.9 Joint structure and test details. (a) Loading arrangement (b) Strain gauge positions [35].	32
Figure 2.1.10 The predicted failure mechanism including delamination, compressive and tensile matrix cracking [35].	33
Figure 2.1.11 Predicted delamination process in the L-shaped laminate; delamination initiation curve and delamination propagation curve (top), structural response (bottom) [38].	36
Figure 2.1.12 Measured and predicted structural response for L-shaped laminates without initial delaminations [38].	37
Figure 2.1.13 The stress contours during delamination initiation and propagation [42].	38
Figure 2.1.14 (a) Specimen configurations (b) Load displacement curves (c) Delamination in curved region [43].	40
Figure 2.1.15 The radial stress along the thickness direction [43].	41
Figure 3.1.1 [0/90] Fabric specimen showing in thickness plane. (b) Micrograph of the specimen from x-z plane.	45
Figure 3.1.2 (a) [0] UD specimen showing in thickness plane (b) Micrograph of the specimen from x-z plane (c) Micrograph of the specimen from y-z plane.	45
Figure 3.1.3 (a) [90/0] UD specimen showing in thickness plane. (b) Micrograph of the specimen from x-z plane.	46

Figure 3.2.1 (a) Schematic of manufacturing process of composite laminate with hand lay-up technique (b) Hand-layup over the male tool (c) Preparation for vacuum bagging (d) Vacuum bagging process (e) After manufacturing process.....	47
Figure 3.3.1 (a) The geometry of L-shaped specimen (b) The composite specimens for three different lay-up.	48
Figure 3.3.2 Example for crack length calculation.	54
Figure 3.4.1 (a) Schematic of the loading fixture for perpendicular loading of the arm (b) Photo of the fixture and specimen before the experiment.	54
Figure 3.4.2 (a) Proposed and used loading fixtures to simulate the loading perpendicular to the upper arm of the L-shaped specimens. (b) Comparison of fixtures with the finite element analysis in terms of stiffness.	55
Figure 3.4.3 Experimental Setup.....	57
Figure 3.5.1 (a) Monitored area (b) Cutting process (c) Cold molding with vacuum extractor (d) Grinding and polishing process (e) The final view of microscope samples.	59
Figure 3.5.2 (a) Monitoring process with Leica DMi1 microscope (a) Micrographs of specimens.	59
Figure 4.1.1 Numerically predicted normal (S_{33}), shear (S_{13}) and longitudinal (S_{11}) stress distributions in the [0/90] fabric L-shaped composite laminate prior to delamination initiation [17].	62
Figure 4.1.2 Numerically predicted normal (S_{33}), shear (S_{13}) and longitudinal (S_{11}) stress distributions in the [90/0] cross-ply L-shaped composite laminate prior to delamination initiation [53].	63
Figure 4.2.1 Load-displacement curves for [0/90] weave fabric tests.	64
Figure 4.2.2 The cracked surface of F2 after failure.	65
Figure 4.2.3 Photograph of the L-beam fabric specimen in the test fixture (a) before starting the shear loading test and (b) after the failure.	65
Figure 4.2.4. High speed camera images of the (0/90) _{6s} fabric CFRP L-beam laminate: (a-g) 15.7 mm by 17.5 mm field of view in the curved region at 1.9 μ s time interval showing delamination initiation and propagation (experiment F2), (h-i) 32.0 mm by 16.4 mm field of view in the vertical arm with 2.7 μ s time intervals showing delamination propagation (experiment F6).	67

Figure 4.2.5. Crack length as a function of time for the left crack tip (solid symbols) in the curved region (Experiment F2) and the arm (Experiment F6) and the right crack tip (open symbols) in the curved region only (Experiments F1 and F2).....	68
Figure 4.2.6. Crack Tip Speeds as a function of time for the left crack tip (solid symbols) in the curved region (Experiment F2) and the arm (Experiment F6) and the right crack tip (open symbols) in the curved region only (Experiments F1 and F2).	69
Figure 4.2.7 Micrograph of a [0/90] fabric specimen in general view.	70
Figure 4.2.8 Micrograph of a [0/90] fabric specimen with close-up of cracked regions (a) Cracked surface near the legs (b) Cracked surface near the middle part of curvature.....	71
Figure 4.3.1 [0] ₁₇ specimen load displacement curve under perpendicular loading.	73
Figure 4.3.2 High speed images of Specimen 1 taken at 620000 fps.	74
Figure 4.3.3 Picture of the [0] UD specimen after failure.	75
Figure 4.3.4 (a) The right crack tip progress during delamination propagation (b) Crack tip speed history for the initial crack of [0] ₁₇ specimen under perpendicular loading.....	75
Figure 4.4.1 Load displacement of the [90/0] specimens curve under perpendicular loading.....	76
Figure 4.4.2 [90/0] cross-ply progressive damage pictures taken at 465000 fps (a) 1 st load drop (b) 2 nd load drop (c) 3 rd load drop	78
Figure 4.4.3 Picture of the [90/0] cross-ply specimen taken after the failure.....	78
Figure 4.4.4 (a) The right and left crack tip progress during delamination propagation (b) Crack tip speed history for initial crack of [90/0] specimen under perpendicular loading.....	79
Figure 4.4.5 Micrograph of the curved region of the [90/0] cross-ply laminate.....	82
Figure 4.4.6 Specimens with variable thicknesses.....	83
Figure 4.4.7 7-ply specimen results (a) Load-displacement curves (b) High speed camera images ($\Delta t=2.38 \mu s$).....	84
Figure 4.4.8 11-ply specimen results (a) Load-displacement curves (b) High speed images ($\Delta t=2.38 \mu s$).	84
Figure 4.4.9 Load- Displacement curves of the 21-ply specimens.....	85
Figure 4.4.10 21-ply specimen results ($\Delta t=2.38 \mu s$).....	85

Figure 4.4.11 Load-displacement curves of the 25-ply specimen.....	87
Figure 4.4.12 High speed camera results of the 25-ply specimens ($\Delta t=2.38 \mu s$).....	87
Figure 4.4.13 (a) Right Crack length vs. time graph with respect to the crack nucleation point for 7, 11 and 21-ply laminates. (b) Right crack tip speed for 7, 11 and 21-ply laminates.	88
Figure 4.4.14 (a) Left Crack length vs. time graph with respect to the crack nucleation point for 7,11 and 21-ply laminates. (b) Left crack tip speed for 7, 11 and 21-ply laminates.	89
Figure 4.4.15 The crack initiation locations for (a) 11-ply specimen (b) 21-ply specimen.....	90
Figure 4.4.16 Load-displacement curves of 5mm inner radius experiments.	91
Figure 4.4.17 High speed camera pictures for specimen 2 ($\Delta t=2.38 \mu s$).	92
Figure 4.4.18 The angular position of the first delamination with respect to the center of the curvature.....	93
Figure 4.4.19 (a) Right and Left crack length vs. time (b) Right and left crack tip speeds vs. time for 5mm inner radius specimen-2.	93
Figure 5.1.1 The texture difference between the Fabric and UD laminate for 90/0 orientation.....	96
Figure 5.1.2 The load-displacement curves of the fabric and UD specimens.....	97
Figure 5.1.3 The high speed images of the Fabric [0/90] laminate with the micrograph of the curved region.	97
Figure 5.1.4 The high speed images of the UD [0/90] laminate with the micrograph of the curved region.....	98
Figure 5.2.1 Load-displacement curves of [0] and [90/0] specimens.	99
Figure 5.2.2 Failure mechanism of [0] UD laminate.	100
Figure 5.2.3 Failure mechanism od [90/0] cross-piled laminate.....	101
Figure 5.3.1 Load displacement curve of specimens with variable thickness	101
Figure 5.3.2 The angle between lateral and longitudinal displacement with respect to load application.	103
Figure 5.3.3 Normalized load displacement curve of specimens with variable thickness.....	103

Figure 5.3.4 Comparison of initial delamination failure high speed pictures of [90/0] cross-ply specimens.	103
Figure 5.4.1 Comparison of load-displacement curves for 5mm and 10 mm inner radii.	105
Figure 5.4.2 (a) 5-mm inner radius and 10-mm inner radius specimens after testing (b) Snapshot of first delaminations during first load drop.	106
Figure B.1 [0/90] fabric lay-up experiments.....	120
Figure B.2 [0] uni-directional lay-up experiments.....	120
Figure B.3 [90/0] cross-ply lay-up experiments.	121

LIST OF SYMBOLS

a	Crack Length
A_{ij} (i,j=1,2,6)	Extensional stiffness matrix components
c_1^{\parallel}	The dilatational wave speed of the material parallel to fibers
c_1^{\perp}	The dilatational wave speed of the material perpendicular to fibers
c_s	The Shear wave speed of the material
c_R	Rayleigh wave speed of the material
c_{ij}	Stiffness matrix components
C'_{ij} (i,j=1,2,6)	Reduced stiffness matrix components
d	Displacement in y-direction
E_i	Elastic modulus
G	Energy release rate
G^I	Mode-I energy release rate
G^{II}	Mode-II energy release rate
G_{ij} ($i \neq j$)	Shear modulus
L_1	Left arm
L_2	Right arm
P	Axial load parallel to the right arm
R_i	Inner Radius
S_{11}	Numerically predicted longitudinal stress
S_{13}	Numerically predicted shear stress
S_{33}	Numerically predicted normal stress
M	Moment loading
u_3	Displacements along width direction
V	Shear load perpendicular to the right arm
v	Crack tip velocity
t	Time
t	Thickness

w	Width
x	Displacement in x direction
ρ	Density
$\nu_{ij} (i \neq j)$	Poisson ratio
σ_r	Radial stress
$\tau_{r\theta}$	Shear stress
σ_{11}	The radial normal stress
σ_{13}	The shear stress
σ_{ij}	Stress components
θ	Angle of the specimen with respect to x direction
Δa	Displacement error
Δv	Velocity error
x,y,z	Coordinate axes

ABBREVIATIONS

ACEE	Aircraft Energy Efficiency
ASTM	American Society for Testing of Materials
CFRP	Carbon Fiber Reinforced Polymer
CZE	Cohesive Zone Elements
DCB	Double Cantilever Beam
ECT	Edge Cracked Torsion
FAA	Federal Aviation Administration
FEA	Finite Element Analysis
FEM	Finite Element Modeling
FPF	First Ply Failure
FRP	Fiber Reinforced Polymer
KETP	Karbon Elyaf Takviyeli Polimer
LEFM	Linear Elastic Fracture Mechanics
MMB	Mixed Mode Bending
NASA	National Aeronautics and Space Administration
NDI	Non-Destructive Inspection
NM	Nautical Miles
UD	Uni-Directional
VCCT	Virtual Crack Closure Technique

CHAPTER 1

INTRODUCTION

In this chapter, the composite material usage in aircraft industry, specifically in L-shaped geometry, is discussed. Firstly, the word “composite“ is defined and the laminated composite materials are mentioned in detail. Secondly, the structures that consist of composite material are explained and examples of the L-shaped structures are given. Thirdly, the mechanical load on the L-shaped parts is defined, where the box structures in a wing are taken as reference. By this way, the delamination problem in the curved composite laminates is defined. Finally, the scope of this thesis is introduced.

1.1. What is a “composite”?

The history of the word “composite” dates back to 1400 BC. It is derived from the Latin word “compositus” which is the past participle form of “componere“(from com- “together” +ponere “to place”[1] and means “placed together”. Basically, the meaning of composite is the combination of two or more materials with different physical or chemical properties that, when combined, produce a new material with different physical characteristics from the constituents [2]. The main factor that distinguishes composites from alloys is that the constituent materials stay separate within the finished structure at the macro scale because they are chemically and physically different. The aim of manufacturing “composed” material is to create stronger, lighter or cheaper product than its homogeneous counterparts.

In early times, a combination of wood, bone, reed and animal glue were composed to build strong and durable bows and arrow shafts [3]. The most famous example in the history was composite Mongolian bows, which provided Genghis Khan with an extremely powerful and accurate weapon, and it was regarded as the most powerful weapon until the invention of gunpowder [3]. In the 20th century, the natural resins

were replaced with the plastic based materials like vinyl, polystyrene, polyester and phenolic. The synthetic materials enlarged composite usage to different areas. In structural applications, reinforcement became an important issue to provide strength and rigidity [3]. In 1935, Owens Corning introduced the first glass fiber [3]. When the fiberglass was mixed with a plastic polymer, extremely strong and lightweight structures were created.

In the 1970s, the composite industry began to mature. Better plastic resins and improved reinforcing fibers were developed. DuPont developed an aramid fiber known as Kevlar, which has become the standard in armors due to its high impact resistance [4]. Carbon fiber was also developed around this time. Although the carbon-reinforced polymers (CFRP) were expensive to produce, they were commonly used when strength-to-weight ratio and rigidity were needed in components such as aircraft wings or fuselage, automotive parts and sporting goods [4].

Compared with the isotropic or organic materials, the main advantage of the composite material is the weight saving. In addition, several important benefits of composites include non-corrosiveness, non-conductivity, flexibility, low maintenance, long life and design flexibility. Due to these advantages, fiber reinforced polymers (FRP) are commonly used in aerospace industry, marine industry, automotive components, military based equipment and wind turbine blades. Currently, there is an increasing trend in composite industry to use composite materials in complex shapes.

1.2. Laminated Composite Material

In this study, the word “composite” refers to “laminated composite” which consists of fibers and epoxy parts that mix together in a specified orientation and amount to achieve specific structural properties. The strength of composites depends on the composition, orientation, length and shape of the fibers the properties of the matrix and the quality of the bond between the fiber and epoxy parts [9]. The stiffness and strength properties of the laminate highly depend on fibers. The composite material is only strong and stiff in the direction of fibers [44]. Therefore, the fiber dominates the field in term of volume, properties and design versatility [17]. The major types of composite fibers are compared in the following paragraph.

Fiberglass: It is often used for secondary structures on aircraft like fairings, radomes and wing tips. The major reason for using the fiberglass is its lower cost compared with the other composite materials and the dielectric nature of fibers. The primary field of application is the aircraft parts that do not have to carry heavy loads or operate under critical stress. Two types of fiberglass are available: E-glass (electrical glass) and S-glass or S2-glass (structural fiberglass). S-glass has higher strength whereas E-glass has outstanding dielectric property [44].

Kevlar (Aramid fiber): Kevlar is DuPont's product name for aramid fibers [44]. There are two type of aramid fibers used in aircraft industry; Kevlar 49 with high stiffness and Kevlar 29 with low stiffness. These aramid fibers have been used for structural applications since 1970s. The high specific tensile strength and high toughness of the material with low density increased the percentage of usage day by day (Figure 1.2.1). It is famous with it's the tensile strength compared to steel. At the same weight, the Kevlar is five times stronger than steel. Another advantage of aramid fibers is their high resistance to damage impact since the material is important for the areas prone to damage impact. The main disadvantages of the aramid fibers are their general weakness in compression and hygroscopy.

Boron: Boron fibers are very stiff and have high tensile and compressive strength. Boron fibers have limited application areas due to the high manufacturing costs and large fiber diameters. The general application area of boron fibers is repairing cracked aluminum aircraft skins because the thermal expansion of boron is close to aluminum [44].

Graphite /Carbon fiber: Carbon and graphite fibers have the hexagonal layer network which is present in carbon. In graphite fibers, the manufacturing time and cost is relatively high and the bonding between planes is weak. Due to this observation, the later explanations belong to carbon fibers. Carbon fibers are 3 to 10 times stronger than the glass fiber [44]. Due to their high strength-to-weight ratio and stiffness-to-weight ratio, they are used in matrix systems for high-performance structures such as stabilizers, fuselage, wing primary and secondary structures and flight control parts. Also, the fatigue limits of carbon fibers are better than aluminum or steel counterparts with superior vibration damping [9]. However, the conductive capacity is lower than aluminum which requires lightning protection mesh or coating

in case of a lightning strike. Another disadvantage is the high cost of carbon fiber manufacturing [44].

The main characteristics of carbon fibers and the advantages are explained. A brief advantage/disadvantage comparison chart is shown in Figure 1.2.1a. Carbon fibers have the best average value among the three main fiber types. In addition, the composite usage in commercial aircraft between 1950-1990 is shown in Figure 1.2.1b. The glassfiber parts were replaced with the carbon fiber and graphite-Kevlar hybrid fibers. Due to these reasons, carbon fiber type reinforcement is chosen to be analyzed in this thesis.

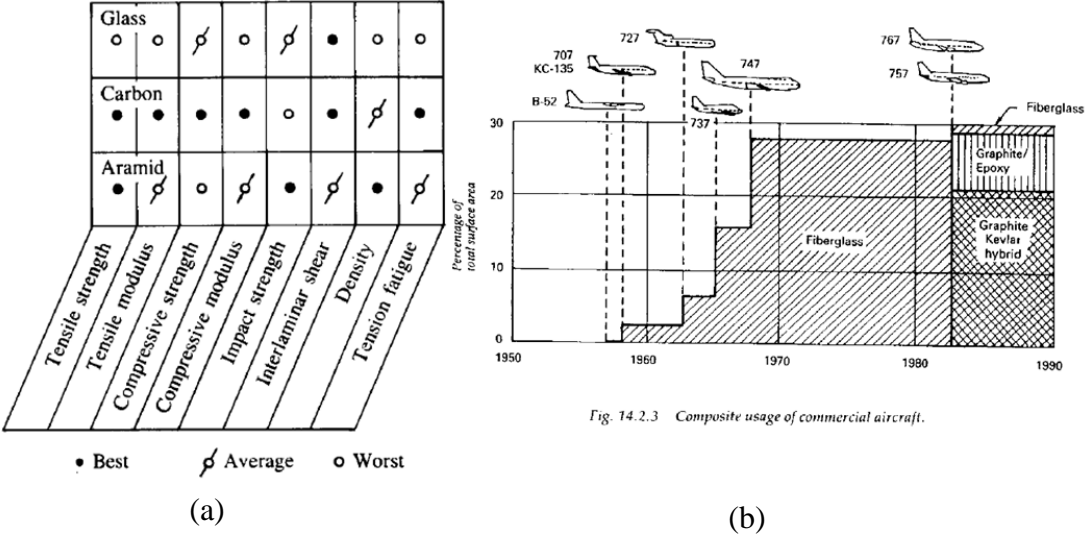


Fig. 14.2.3 Composite usage of commercial aircraft.

Figure 1.2.1 (a) Composite fiber comparison (b) Composite usage of commercial aircrafts [9].

The main types of fibers are explained in previous paragraphs. These fibers are grouped as unidirectional tape, woven fabrics and pre-preg for manufacturing. Unidirectional type forms include fibers only in one direction. Properties of transverse direction of fibers highly depend on the matrix material. Therefore, the fibers are oriented in specified directions in each ply to withstand the longitudinal and transverse loadings. Woven fabrics have more complex shape than the unidirectional tapes. In this case, fiber bundles are knitted or weaved in plain or different harness types, repetitively. On the other hand, the pre-preg forms include unidirectional or woven fibers impregnated with resin, which can be laid up in plies and cured. In pre-pregs, the partially cured epoxy preserves the orientation and

alignment of fibers during the lay-up which provides a close control of strength and weight in the finished component [9].

The fiber reinforcement is placed to produce optimum mechanical properties and dimensional stability. In the design of fiber stacking, the composite materials have their own nomenclature and coding rules. In this part, the global directions and coding system of composites are introduced. The 0° fiber direction refers to the x-direction which is the longitudinal direction of fibers. The 90° refers to the y-direction which is transverse to the fibers in unidirectional case (Figure 1.2.2a). In multidirectional stacking laminates, the warp clock method is used to entitle the stacking sequence. Warp indicates the longitudinal fibers of a fabric (Figure 1.2.2b) [44]. A classic example of multilayered composite is shown in Figure 1.2.2c. 0° layers are parallel to the x-axis and 90° layers are parallel to the y-axis.

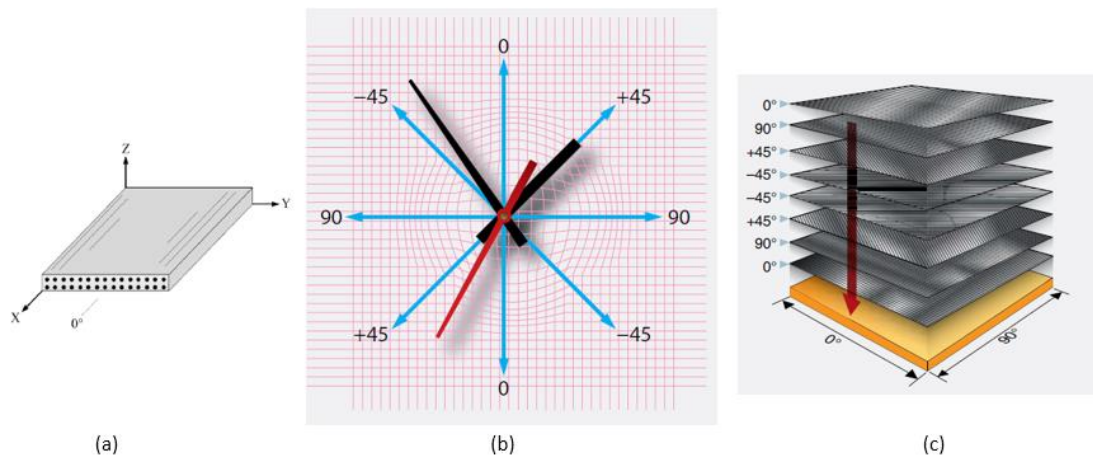


Figure 1.2.2 Composite fiber orientation rules [44].

1.3. Composite Structures in Aircraft Industry

Composite material usage in aircraft industry is an increasing demand since manufacturers look for ways to reduce weight, increase strength and durability and improve performance of an aircraft. Composite materials are being used in transport airplane components for decades which are typically formed by carbon or glass fibers with epoxy. The first composite aircraft in history is accepted the British two-seated small airplane Bristol Scout in the 1910s [5], the usage of composites in large transport aircrafts was not seen until the early 60s [6]. After this time, there was an increasing trend of composite usage in general aviation. The main reason is the

reduction of weight in airplane parts compared to the equivalent metal structures [7]. A Federal Aviation Administration (FAA) Advanced Materials Research Program report had shown that for every pound of weight saved on a commercial aircraft, there is a US\$100,000-300,000 cost saving over the service life of that aircraft [7,8,9].

A major breakthrough had occurred with the increased composite usage in aircraft industry in 1970s. NASA had spent more than \$60 million dollars on the Aircraft Efficiency (ACEE) Program for the designing, manufacturing and testing of composites [9]. The ACEE program expanded the scope of the commercial transport applications, which include three secondary (L-1011 Ailerons, 727 Elevators, DC-10 Rudder) and three primary structure products (L-11011 Vertical fin, 737 Horizontal tail, DC-10 Vertical fin) (Figure 1.3.1).

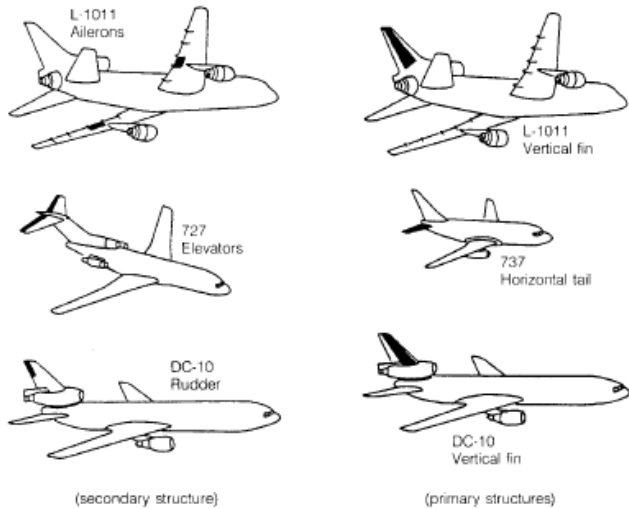


Figure 1.3.1 Aircraft components of NASA ACEE program using composite materials [9].

After this project, the composite material usage accelerated as shown in Figure 1.3.2, where commercial airplane models over time by the percentage of composites [11]. Prior to the mid-1980s, airplane manufacturers continued to use composite materials in transport category airplanes in secondary structures (e.g., wing edges) and control surfaces (e.g. ailerons).

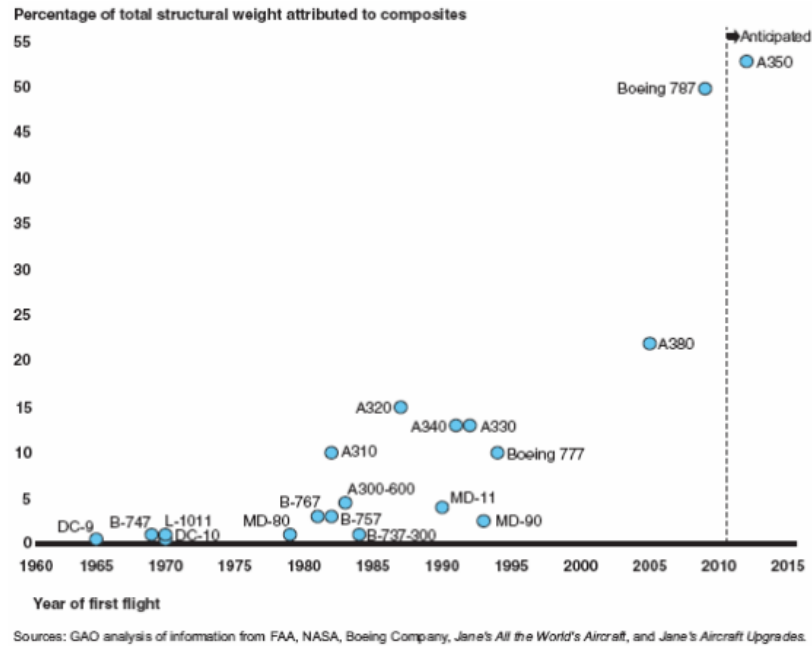


Figure 1.3.2 Percentage of total structural weight attributed to composites by years [10].

Airbus started to use composite sub-structures in the mid-80s with A310 spoilers, airbrakes and rudder parts. In 1988, Airbus introduced the A320, the first airplane in production with an all-composite tail section (Figure 1.3.3) and, in 1995, the Boeing Company introduced the Boeing 777, also with a composite tail section [10]. In the aircraft industry, an important example to enlarging the usage of composites is the Boeing 787 Dreamliner. In which 50 percent of the airplane by weight (Figure 1.3.4) was produced with composite material (excluding engines) [10]. The capacity of the aircraft is remarkable. The Boeing 787 Dreamliner is 10,000 lbs lighter and burns 20% less fuel than a comparably sized all-aluminum aircraft [11]. It will carry 210-290 passengers on routes of 7650 NM to 8500NM [11]. Another important example for the composite industry is Airbus A380 which consists of a composite center wing box, wing ribs, a rear unpressed fuselage and cross beams. In 2006, the experts claimed that “the Airbus A380 is scheduled to enter service with an airframe that is 25% composite by weight, including an all-composite center wing box” [12].

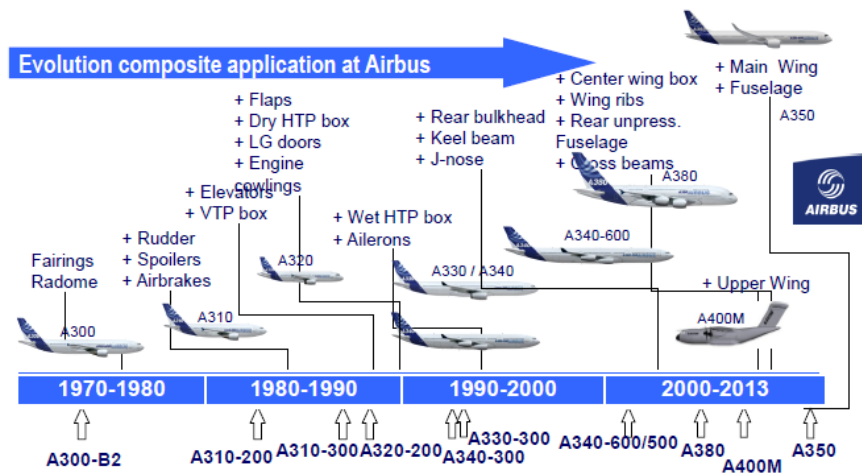


Figure 1.3.3 Evolution of composite applications at Airbus by year and model (By courtesy of AVALON Consultancy Services LTD.).

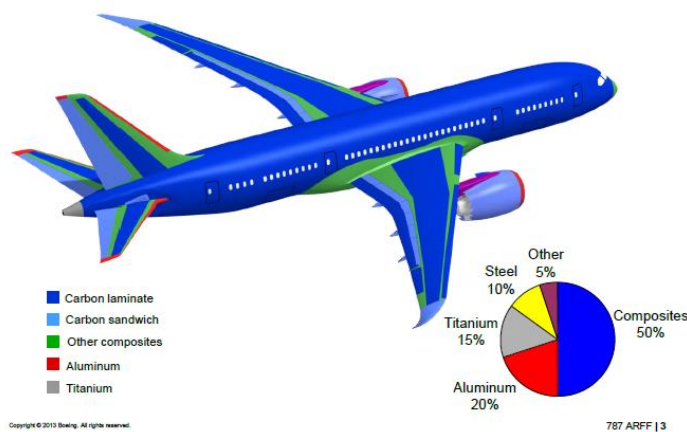


Figure 1.3.4 Composite structure content of the Boeing 787 [10].

The increased use of the composite materials has created a strong demand for non-destructive inspection (NDI) of composite structures, both in the fabrication process and for the in-service inspections [13]. Since composites have a laminated nature and their damage mechanisms are different than the metals, they are subjected to their own distinct problems. For instance, delaminations and matrix cracks are common damage modes, which nucleate the inner part of the structure and are not visible on the damage surface. This fact is also a problem for inspection and because of that, aircraft manufacturers use sensors inside the structure to detect the damage. Another important challenge with composites is computer simulations. The non-uniform properties due to heterogeneity, the variability of composite parameters such as ply

orientations and the number of plies make an analysis on computer difficult. Besides, the increasing stiffness of the material requires non-linear analysis and the dynamic fracture mechanisms of composites need explicit solutions. With comprehensive simulations and more reliable manufacturing options of composites, the aviation industry has integrated composite structures into the aircraft design at an accelerated pace [14]. But, the lack of knowledge on failure mechanisms and composite testing enforce the industry to become conservative in design [14]. It is necessary to make progress in testing mechanisms and numerical analyses to customize a new technology and make it safe [15].

1.4. L-Shaped Composite Structures

In this part, the interior structure members of aircrafts are introduced and the L-shaped parts of these members are emphasized. In general, the basic functions of an aircraft's structure are to transmit and resist the applied loads (flight loads, body loads, landing loads, propulsion system loads etc.) and provide the aerodynamic shape of the airplane. These functions are carried with thin shell structures, namely skin of wing and fuselage. The most critical part of an airplane is the wing box structure, which must be light and strong to create lift and withstand the bending moment [16]. The wing box structures are strengthened with the longitudinal stiffening members to transverse frames and make it possible to resist bending, tensile/compression, torsional and shear loads without any elastic instability. Box structures or torque box structures are the general names of the load carrying sub-structures of a wing, which consists of ribs, spars and stringers [16]. There are several arrangements of these members for modern high-speed airplanes: thick box beam structure (high aspect ratio wings), which is built up with two or three spars and multi-spar box structure (low aspect ratio wings) with thin airfoil (Figure 1.4.1).

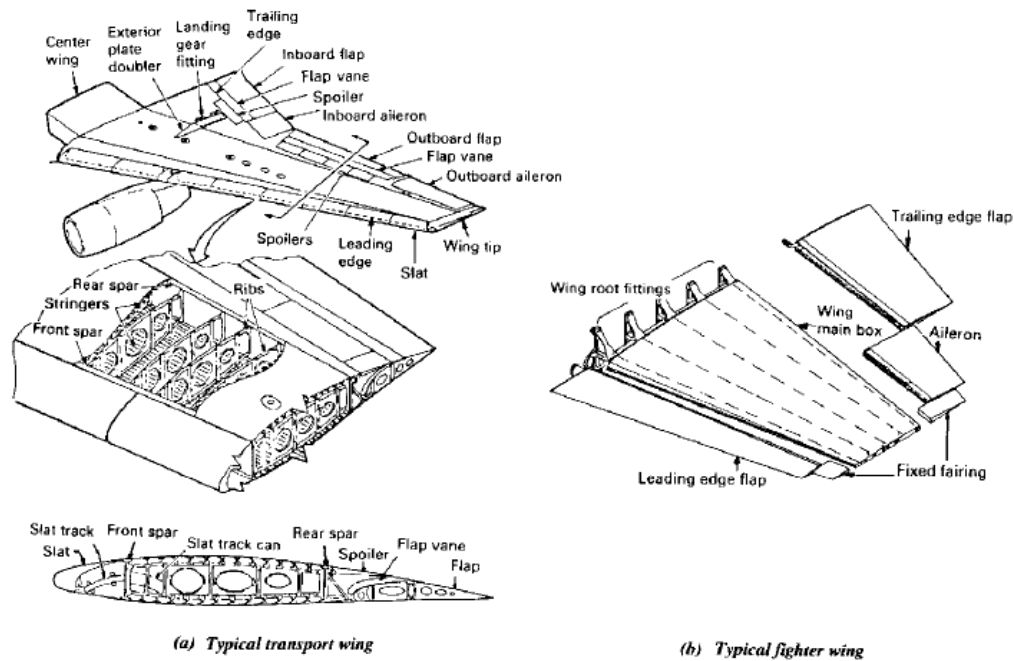


Figure 1.4.1 Typical transport and fighter airplane wings [16].

In a typical wing cross section, L-shaped parts are placed into the wing covers as the extension of spars/ ribs that are laid through the skin or as a separate part which connect the rib to the skin (i.e. stringers). By definition, three different forms as L-shaped parts appear, which are flange of a spar/rib, L-Bracket and back-to-back configuration [17]. Some examples are explained below.

Skin-Stringer Panels

The most common wing covers of transports are skin-stringer panels (Figure 1.4.2a) [16]. The machined skins are combined with machined stringers, riveted, bolted or bonded by adhesive. This is the most efficient structural mechanism to save weight [16]. In Figure 1.3.2b, a closed shot of the typical interior stringer of the Boeing 787 is shown which is formed as L-shaped and bolted to the skin [18].

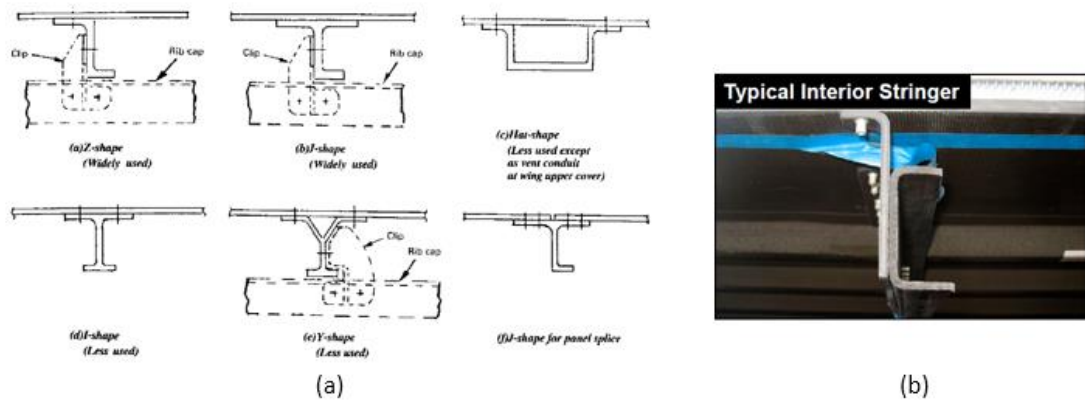


Figure 1.4.2 (a) Types of skin-stringer panels [16] (b) Closed view of Boeing 787 interior stringer panel [18].

Integrally Stiffened Panels

Integrally stiffened panels are another solution for lightweight and high-strength construction which is composed of skins and stiffeners into one-piece panel section. By this way, the number of the basic assembly members is reduced and the skin has smoother surface. In Figure 1.4.3, several different sections of integrally stiffened panels are shown.

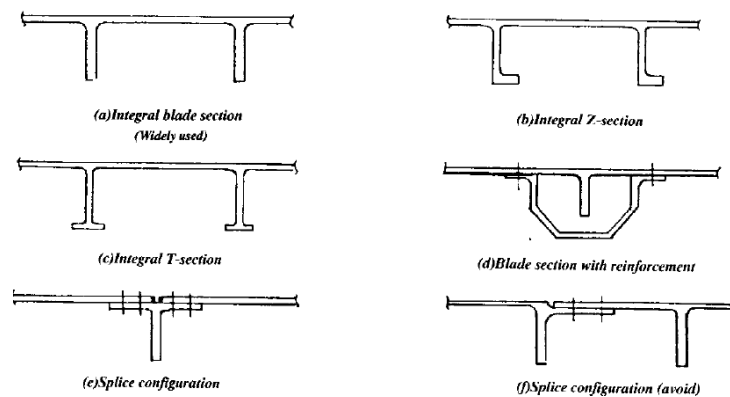


Figure 1.4.3 Typical integral stiffened panels [16].

Spar Caps

Spar cap sections are always used with a beam web composed of flat sheet. The air loads acting on the wing are directly transmitted to ribs. And, the ribs transmit the loads in shear to the spar webs and distribute the load between them according to the web stiffness [16]. Some of the spar cap sections are shown in Figure 1.4.4. The use

of spars reduces the stress on the ribs and also provides a better support for the spanwise bending material [16].

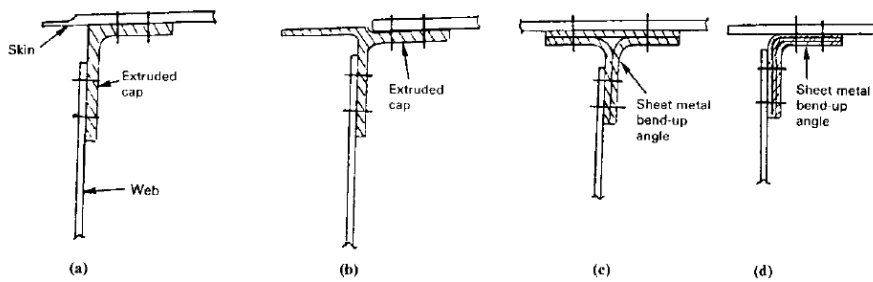


Figure 1.4.4 Typical spar cap sections [16].

Ribs and Bulkheads

Wings have to be strengthened in the chord direction for aerodynamic reasons. Hence, ribs are used to hold the cover panel, to contour shape, and also to limit the length of skin-stringer or integrally stiffened panels to an efficient column compressive strength (Figure 1.4.5). Another important task of ribs is to distribute or transfer the applied loads. Typical wing rib parts are caps, stiffeners and webs [16]. Rib bulkheads are also placed in the flaps, ailerons, landing gear support and tank ends for the same reasons.

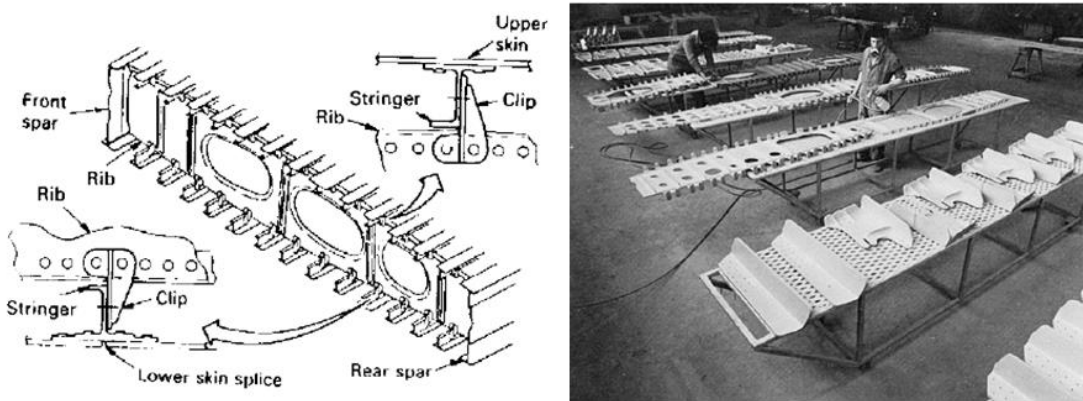


Figure 1.4.5 Typical rib construction [16].

Another important stiffened shell part of an airplane is fuselage, which is commonly referred to semi-monocoque construction. The stiffened material has the same logic with the wing structure. The fuselage as a beam contains longitudinal elements (longerons and stringers) and transverse elements (frames and bulkheads) to maintain the shape of the fuselage and prevent the general instability in the structure (Figure

1.4.6a). The longerons carry the fuselage axial load-moment combination. The fuselage skin, on the other hand, carries the shear due to cabin pressure and external transverse and torsional forces. Stringers are placed to the inner part of the fuselage skin to carry axial loads induced by the bending moment (Figure 1.4.6b) [16]. Generally, the interior structure of the fuselage is mounted with the L-shaped extensions to the skin (Figure 1.4.6c).

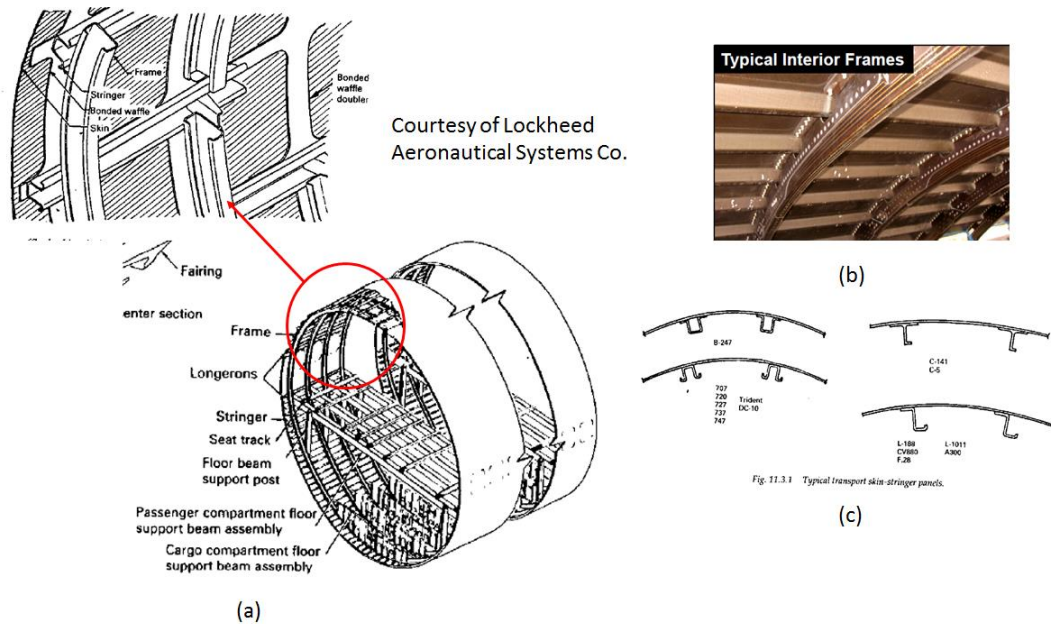


Figure 1.4.6 (a) Typical semi-monocoque stiffened shell (L-1001) [17], (b) Typical Interior Frame of Boeing-787 [19], (c) Typical transport skin-stringer panels for different aircraft models [17].

The load carrying member of the airplane parts were manufactured with the aluminum alloys and isotropic counterparts. After the 80s, there has been an increasing demand to replace the metallic sub-structures with composites as discussed in section 1.3 [10]. New advances in the composite manufacturing technology and the high demand for the lightweight structures are promoting the growth of composite usage in a wide variety of ways, including load carrying members such as L-shaped ribs. Several currently used composite panel stiffening methods and their advantages/disadvantages are described in Table 1.4.1 [16].

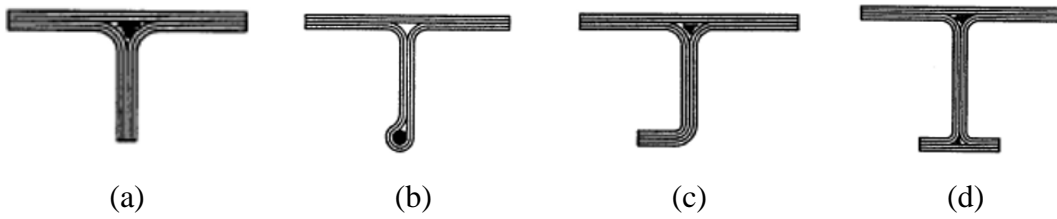


Figure 1.4.7 (a) Blade (b) Unsymmetrical bulb (c) J-stiffener (d) I-Stiffener [16].

Table 1.4.1 Types of composite panel stiffening methods [16].

	Pros	Cons
Blade stiffened panel (Figure 1.4.7a)	Simple to fabricate, easy to stabilize at frame or rib, simple tie-in at frame and rib	Inefficient in bending, edge wrapping may be needed to prevent delamination, marginal torsional stability under axial loading
Bulb panel (Figure 1.4.7b)	Fair in bending, Fair tie-in at frame or rib	Difficult to splice, difficult to fabricate because of possible compaction of bulb
J-stiffened panel (Figure 1.4.7c)	Simple tie-in at frame or rib, double skin flange improves peel and post-buckling strength	Torsionally unstable, difficult to fabricate compared to blade
I-stiffened panel (Figure 1.4.7d)	Symmetric cross-section improves torsional stability; double flanges improve peel and post buckling strength	More difficult to fabricate, splicing difficult because of narrow flanges, difficult tie-in at frame or rib

1.5. Stress State of an L-shaped Member

A typical stiffened member of a wing is subjected to three main kinds of loading, namely the axial load which is parallel to the arm (P), the shear load, which is perpendicular to the arm (V), and the moment (M) (Figure 1.5.1). These loads are the structural response of sub-structures to the external loads. In his thesis, Aki Vanttinen explained the external loads applied to a wing substructure [19]. The origins of the loads were explained as follows;

- Shear loads in the web
- Loads applied to the rib caps due to the bending of ribs
- Shear attachment of the rib to spar and wing covers
- Redistributes concentrated loads: such as nacelle and landing gear loads to wing spars and cover panels.
- Support members: such as skin-stringer panels in compression and shear.
- Inertia loads: fuel, structure, equipment, external stores (missiles, rockets etc.)
- Tension attachment of wing covers to the rib (combined shear and tension loading)
- Crushing loads applied to the rib: when a wing box is subjected to bending loads, the bending of the box as a whole tends to produce inward acting loads on the wing ribs. Since the inward acting loads are oppositely directed on the tension and compression side, they tend to compress the ribs.
- Shear flow distribution on a rib bordering a cut-out
- Additional loads normal to the rib from items such as fuel pressure, slosh etc [16].

These loads are applied to the L-shaped parts of the ribs and create a complex stress state at the curved region, which is a combination of shear (Mode-II), opening (Mode-I) and longitudinal stresses. The combination of these stresses creates delamination, which is the separation of layers.

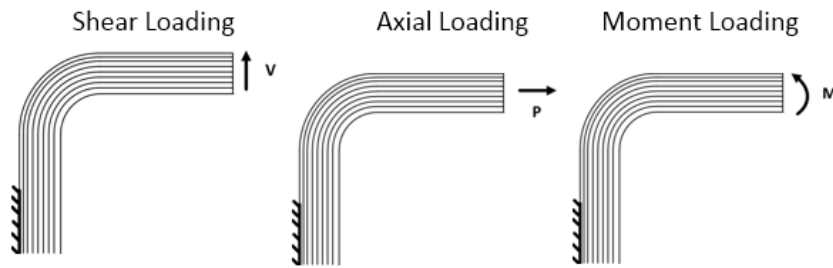


Figure 1.5.1 Types of reaction forces on L-shaped member.

1.6. Delamination Problem in Curved Composite Structures

The composite material usage in aircraft industry is an increasing trend and laminated composites are being used in complex shapes as load carrying members. These parts are exposed to the complex external loads, which were explained in section 1.5. Since composites have a laminated nature, it is important to understand how loads are shared among the plies. These shared loads are causing various types of failure modes. Thus, it is also critical to distinguish the resin and fiber dominated failures. In a curved region of laminates, the primary failure mode is delamination [20, 21]. Delamination, by definition, is the separation of one or more layers according to the low-through-thickness strengths of composites and it causes a reduction in the stiffness of the specimen. The L-shaped brackets of Airbus A380 wings pose as one of the important examples of the delamination problem. According to the New York Times article, cracks are found in the L-shaped brackets that connect the wings' aluminum skin to its structural ribs, which are made of a combination of metal and composite material [23].

In designs, it is important to avoid delamination in the probable locations that are prone to delamination. Some of the delamination nucleation points which are due to manufacturing defects, out-of-plane loads and ignoring the rules of laminate geometry are shown in Figure 1.6.1 [16]. In most applications, multi-oriented composites are used. The material property mismatch between the layers may create singular stresses at the free edge and cause edge delamination [21, 22]. Singular interlaminar stresses are placed around the notch (or hole), into the laminated structure, which may lead to delamination. The reduction points of thickness (i.e. ply

drops) and the regions subjected to the opening stresses are other reasons for delamination [23].

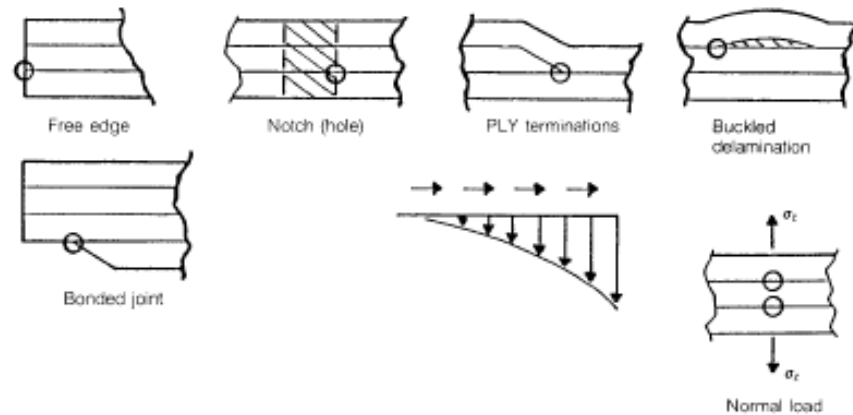


Figure 1.6.1 Delamination Initiation Locations [16].

The curved part of the laminate is considered as critical location for lamina failures (Figure 1.6.2b) [16]. Generally, all three failure modes (Mode-I (opening), II (sliding shear) and III (tearing)) are seen in the delamination initiation and propagation (Figure 1.6.2a). Thus, to characterize delamination, mixed-mode failure analysis has to be conducted. The interlaminar toughness associated with the fracture modes and the corresponding strain energy release rates must be characterized [24]

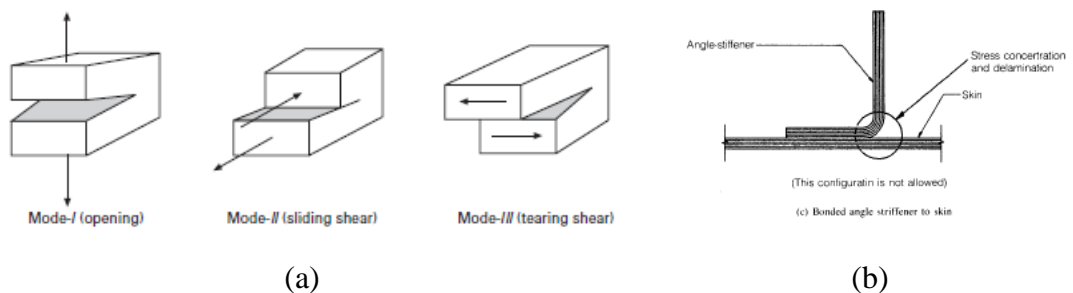


Figure 1.6.2 (a) Three fracture modes lead to delamination [23] (b) Potential delamination critical location [16].

Test methods to characterize the material strength are tabulated in Composite Materials Handbook 17 [25], which shows the coupon test methodology of composite laminates. American Society for Testing of Materials (ASTM) standards was used in most of the tests. Tensile tests for the composite laminates were conducted using the method of ASTM D638. Mode-I and II fracture toughness

values were established with double cantilever beam tests (DCB) and Mixed mode-I and II (mixed mode bending MMB). For pure Mode II and III, there is no standard test method available. Therefore, End Notched Flexure test (ENF) [26,27] for Mode-II and the Edge Cracked Torsion (ECT) [28,29,30] test for Mode III are generally used.

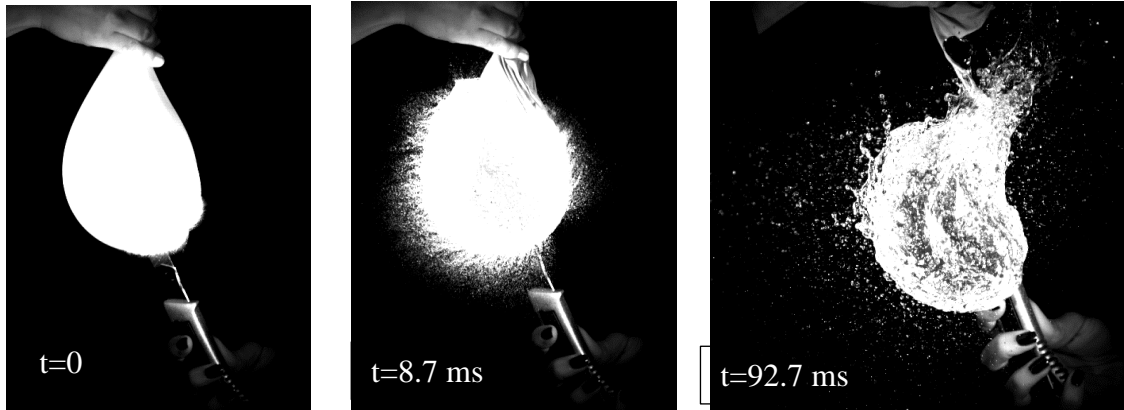
Understanding the fracture mechanism of composites and designing new parts require the knowledge of composite analyses. To characterize the delamination mechanism, standard coupon tests are not enough. The microstructural analysis and the component test must be established. The full scale testing methods (Static, fatigue and damage tolerance) need also to be conducted [16].

1.7. High Speed Monitoring System

In this thesis, the experiments are monitored with high speed camera system. To understand the high speed imaging, it is important to understand the fundamentals of the photography mechanism [50]. For this purpose, some of the factors of capturing mechanism are identified at this section. The first factor is the camera's aperture, which is a circular hole that shrinks or expands to arrange the amount of light. The second factor is the shutter speed which defines the rate at which camera film is exposed to light. The longer the shutter time is, the amount of light reflected onto the film increases [48]. The range of the shutter speed is between a second and 1/2.000.000 seconds depending on the frame rate in our case. The challenge of the high-speed photography is that it depends on how quickly the film is exposed to light. Because of this, the lighting mechanism has a great importance. Once the object passes through the frame, the lighting unit enables the burst of light. In addition to these factors, a photographer has to be aware of some concepts to get a clear photograph from the camera, which are detection, synchronization and imaging [48]. Because the actions can be fast moving and unpredictable, they need to be detected remotely. In our case, the high speed camera system has an external trigger. The camera system displays the live images continuously but its capacity for recording is limited to 16 GB RAM. Thus, the triggering mechanism is set to capture the dynamic event. Photron Fastcam SA5 camera system was used in the experiments. The resolution of the camera is 1MP up to 7000 fps. 10,913 frames can

be recorded at the maximum resolution which corresponds to approximately 1,5 sec recording time. When the frame rates (i.e. speed) increase, the resolution decreases. For example, at 620.000 fps, the measuring area decreases to 64x56 pixels. This provides the increase in the total record time up to 5.15 sec, which corresponds to 3.193.000 frames in total. In Figure 1.7.1, some examples of the shots taken during the high-speed experiments in our lab with Photron Fastcam SA5 are shown.

Water Balloon Explosion @ 7,000 fps



Parfume Spray @ 10,000 fps



Delamination in composite structures @465,000 fps

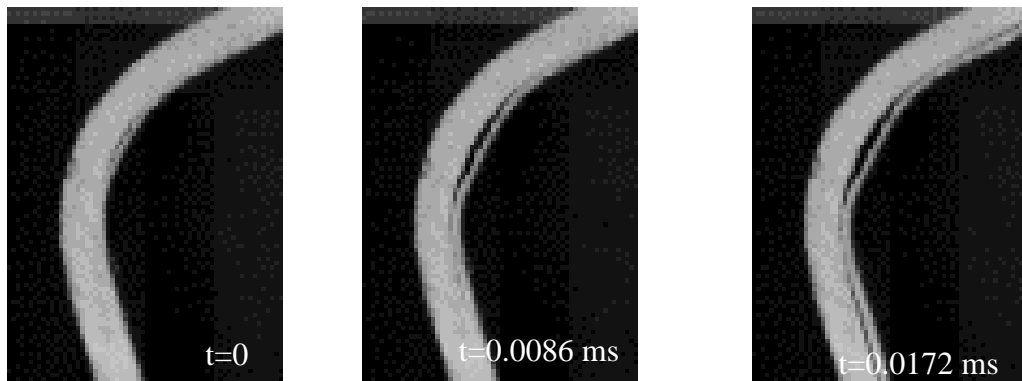


Figure 1.7.1 High speed camera pictures taken with Photron SA5 camera (a) water balloon explosion (7000fps) (b) Perfume spray (10000fps) (c) Delamination in composite laminate (465000 fps).

1.8. Scope of the Study

Laminated composite structures are used in the aircraft industry in different configurations as discussed in the previous sections. In the planar structures like skin and fuselage, the composite material usage dates back to 60s. However, the usage of composites in complex shaped structures is a new concept and needs to be investigated. The weakness of the composite materials under out of plane loadings limits the usage of composites. Therefore, the failure mechanism of the composite parts has to be fully understood. The composite structures are placed in the sub-structures as curved parts. One of the critical configurations for these curved parts is called the “L-shaped”. In section 1.4, the L-shaped parts in aircraft structures are mentioned in detail. Also, the out of plane loads cause the separation of layers, which is a primary failure mode of the L-shaped parts. In this work, the failure mechanism, which is focused on, is delamination. In chapter 2, previous studies that are related to the delamination problem of the curved composite parts will be discussed. In the light of these studies, the delamination is thought to be a dynamic event which propagates on the sub-Rayleigh wave speed of the material. In order to monitor such a dynamic event, a high speed camera system is integrated. The loading case is chosen as the quasi-static shear loading, which was also commonly discussed in the previous literature. In chapter 3, the experimental method will be discussed. The material used in this study, the variables and the measuring techniques will be clarified. In chapter 4 and 5, the results related to experiments will be explained and several concepts will be discussed. Firstly, the dynamic failure mechanism of the delamination problem will be shown. Secondly, the effect of the material on the failure mechanism will be discussed. In this part, the [90/0] UD fibers and the [0/90] weave pre-pregs will be compared. In the third part, the [90/0] (cross-ply) layup and the [0] (uni-directional) layup will be used in the experiments and the effect of the lay-up on the failure mechanism will be discussed. In the fourth part, the effect of thickness on the failure mechanism will be discussed. Thus, specimens with the same orientation are used in five different thicknesses. In the fifth part, the effect of inner radius on the failure mechanism will be discussed. The specimens are manufactured with 5mm and 10 mm inner radii. The aim is to explain dynamic failure mechanism of composites.

CHAPTER 2

LITERATURE SURVEY

2.1. Historical Background

There are numerous studies in literature for ‘delamination’ problem.

2.1.1. Delamination Problem in L-shaped Structures

In this part, studies on delamination problem were discussed in chronological order.

In the paper “The strengths of Fiber Reinforced Composite Bends”, Chang and Springer (1986) conducted numerical and analytical studies to predict the stress-strain field of bend composite parts and the strength of bends made of fiber reinforced composites. For the in-plane failure, Tsai-Hill criterion was used and for out-of-plane failure the Chang-Springer criterion was used. The effect of geometry and ply orientation on failure mode was discussed. The objective of this study was to develop an analytical technique, which calculates the stresses and strains of bends or elbows (curved structures) and estimates the maximum load before the specimens fail. The problem was constructed on unidirectional fibers and the lay-up was chosen as symmetric with respect to the mid-plane. When the angle of the curvature part of the structure was 90° , it was called elbow, and when it was smaller or larger than 90° , it was called bend.

The analysis consists of two parts. In the first part, the stress-strain calculation was conducted and in the second part the failure conditions were established []. In the stress analysis, the thickness to width ratio was assumed small in bends. Thus the displacements along width direction (u_3) were neglected. The stress-strain expression was derived with respect to the plane strain theory. In the second part, the effects of geometry on the bend strength were investigated. Numerical results with five different ply orientations were generated for unidirectional graphite-epoxy laminates. The basic assumption for the strength calculation was that the bend failed

when either in plane failure or delamination failure occurred [31]. The effect of the inner radius of the curved region and the bend angle for five different layups are shown in [Figure 2.1.2-3].

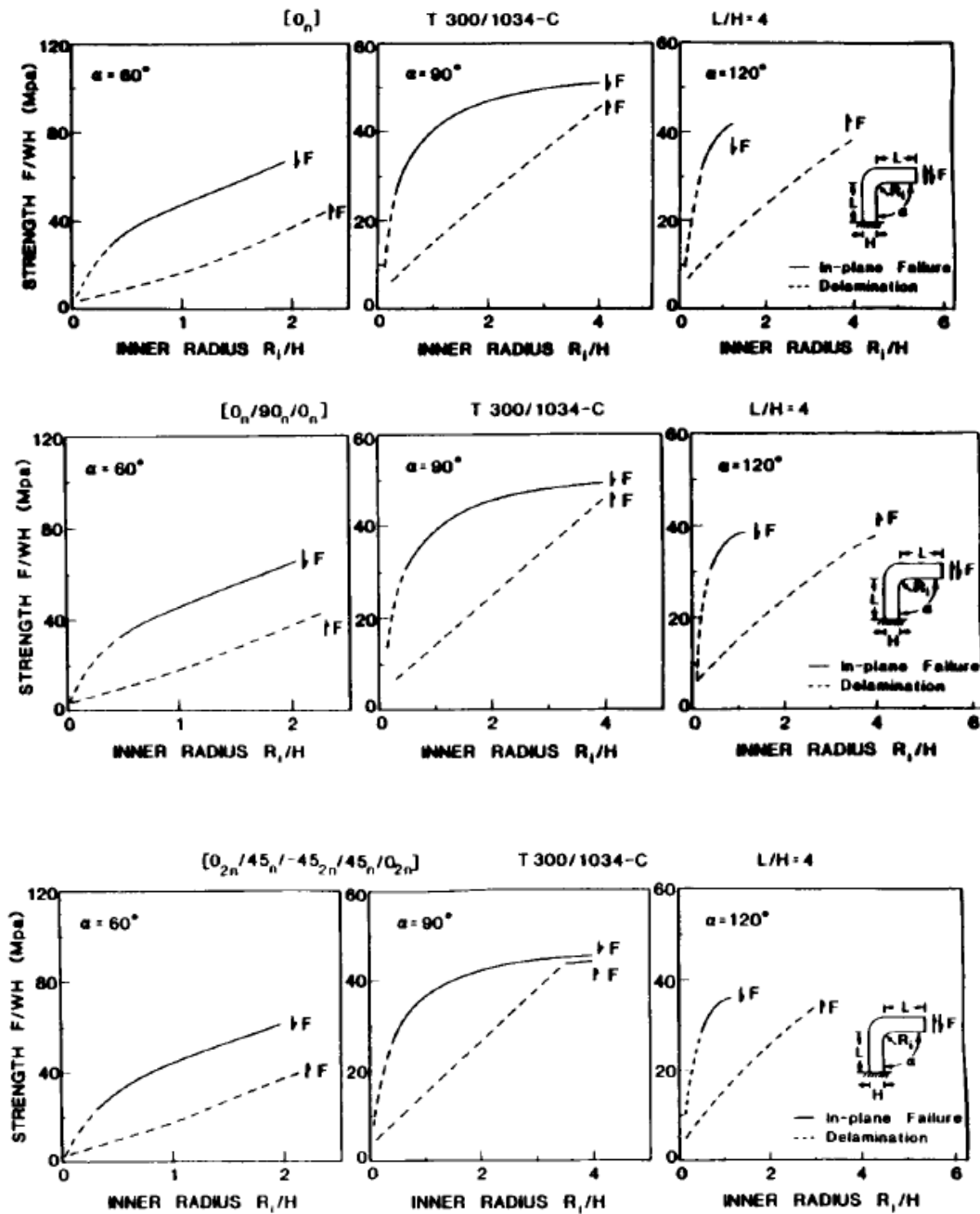


Figure 2.1.1 The effect of inner radius and bend angle on strength for different layups [31].

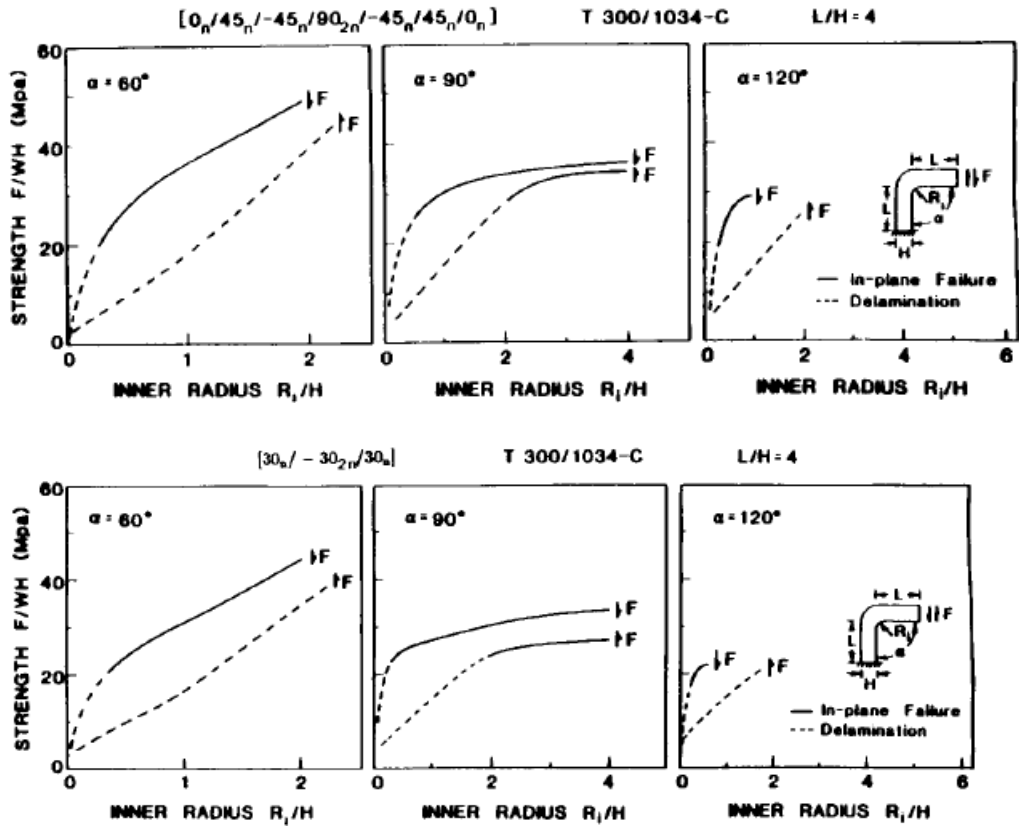


Figure 2.1.2 (Continued) The effect of inner radius and bend angle on strength for different lay-ups [31].

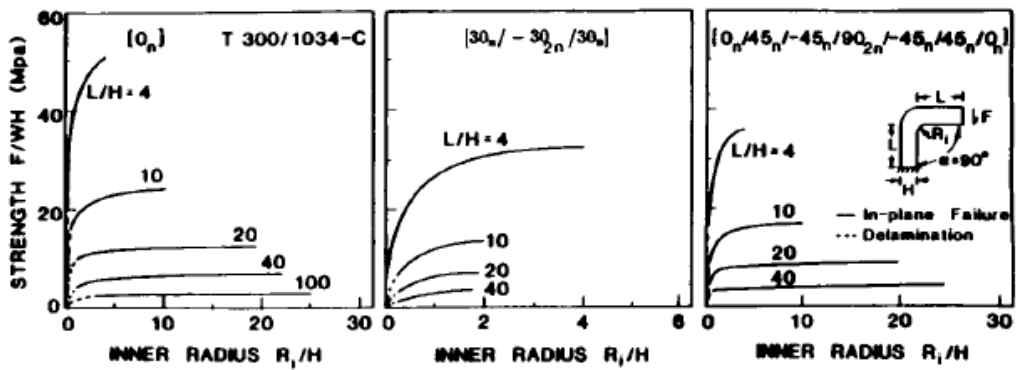


Figure 2.1.3 The effect of the length to thickness ratio on the strength [31].

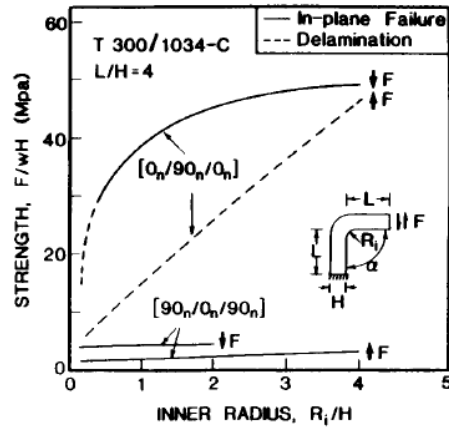


Figure 2.1.4 The effect of stacking sequence on the strength [31].

First comment was that the magnitudes of the inner radius and the bend angle affect the strength as well as the ply orientation [31]. But the critical outcome was that failure is generally due to delamination for small radius to thickness ratios. On the other hand, in higher ratios, the failure mode is changed to in plane under inward bending moment. If the bending moment was outward, the failure mode was always delamination [31]. In addition to these, the highest strain values were obtained in pure 0° fiber orientation and 90° bend angle. Drawing another comparison from the graphs, the bend was weaker for outward acting moments than it was for inward acting moments [31]. A final comparison for the two cross-ply stacking sequence points to the fact that laminates stacking starting with 0° orientation i.e. $[0/90/0]$ were much stronger than laminates stacking starting with 90° orientation i.e. $[90/0/90]$. The importance of this paper is that it was an anti-thesis for the approach, which claims that ‘the stacking sequence is negligible for 2-D flat laminates’. When the laminated structures become curved, the stacking sequence plays an important role in strength and failure mechanisms.

The paper ‘Failure in Composite Angle Structures Part I: Initial Failure’ was written by C.T. Sun and S. R. Kelly (1988). In their paper, they studied the failure mechanisms of composite angle structures both experimentally and analytically. They concluded that, there were two possible failure modes, i.e., initial transverse matrix cracking due to bending stress and final delamination due to through-the-thickness normal stress in curved region [32]. They mentioned that the delamination leads to the complete loss of bending stiffness causing total failure. In some cases, the initial failure mode was matrix cracking in a lamina. But, the small cracks

generally required additional energy to force the matrix crack to become a delamination.

Three different stacking were chosen for experiments including graphite/epoxy and fiberglass/epoxy materials. The pre-pregs were placed to give 0° and 90° orientation. The 0° and 90° plies were grouped by two or three in stacking. The reason was to highlight the different failure modes. In the experimental set-up, the curved specimen was mounted on a fixed grip from the lower leg. In the upper part, specimen was both bolted and clamped to the hinge mechanism. An optical microscope recorded the onset of the damage.

According to the results, the stacking differences affected the initial failure mechanism; matrix cracking was followed by delamination or directly delamination was grown. By means of that, the curved composite laminates had two distinct failure modes which are, in-plane failure and out of plane failure [32]. In the curved region, tensile radial stresses were higher due to geometry, which tends to separate layers. However, the groups of 0° plies near the surface of the layup, where the bending stresses are critical, causes initial failure was bending failure. The small bending cracks needed additional load to cause gross failure mode, which is delamination.

In the paper “Delamination Failure in a Unidirectional Curved Composite Laminate”, Martin (1990) investigated delamination failure numerically and experimentally in a unidirectional curved composite laminate. The idea was to predict the maximum load a unidirectional laminate can sustain. The delamination failure occurred unstably and developed through the curved part, which caused the complete loss of bending stiffness [20]. Delamination failure was assumed to be starting at the location of the highest radial stress in the curved region and a closed form elasticity solution with 2-D FEA was developed to find the location of the highest radial stress [20]. The energy release rate (G) variation was determined with respect to delamination growth. On the basis of these analyses the delamination was predicted to propagate from the curved part to the leg of the laminate under interlaminar tension failure. Another conclusion was about the radial stress in the curved region which was maximum at the inner sublaminates after the initial delamination. These stresses

caused a new delamination formation at the inner part of the curved region without an increase in the applied load.

In the introduction part, possible failure types of laminated structures are shown with the typical usage of curved parts in macro scale (Figure 2.1.5). The main cause of delamination failure was explained as the material property mismatch due to the multi directional lay-up in composite laminate, which cause singular interlaminar stresses [34]. Another source of delamination was explained to be the transverse tension cracking across the width [34]. These stresses caused delamination induce by matrix cracking at this location. A final description of delamination formation was interlaminar tension failure caused by the bending of curved laminate.

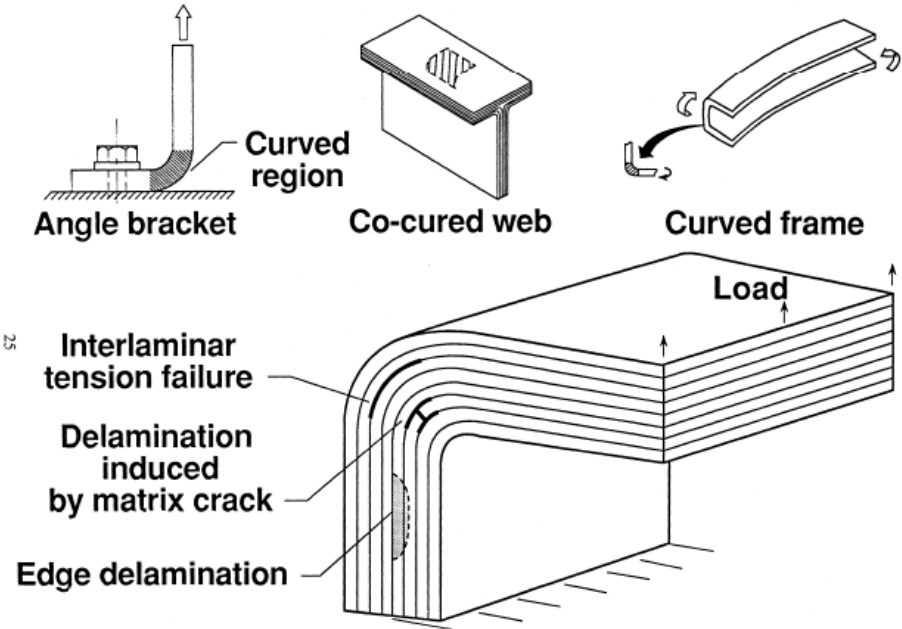


Figure 2.1.5 Possible failure mechanisms of composite curved structures [34].

In experiments, 24 plies of unidirectional graphite/epoxy curved laminates were used. The fracture toughness tests were conducted and the average properties were calculated. From the calculations the specimens were assumed as transversely isotropic. As a result of the calculations, the specimens were found to be transversely isotropic.

During the experiments, small load cell (890N) was used to accurately monitor the small load changes due to matrix cracking [20]. The lower part of the curved

laminates was clamped to the ground and the upper side was clamped in a hinge system which was free to pivot (Figure 2.1.6a). As an author comments, the displacement change during experiments was small due to the high stiffness of UD curved laminates. Because of this, the load applied via hinged was considered to be vertical. In the results, the maximum load per unit width and the place of first delamination initiation was tabulated. There were two important outcomes of this result. First, the maximum failure load, which was highly changeable, varied from 7N/mm to 14N/mm. Second, the delamination initiation place, which is 49-46% of total thickness, was nearly the same for each experiment. A picture of the occurrence of delamination is shown in (Figure 2.1.6b). It is shown that a single delamination is initiated at 48% of the thickness and a second delamination is initiated at 23% of the thickness. Finally, multiple delamination growth was shown and the longest delamination in the picture was defined as the first delamination.

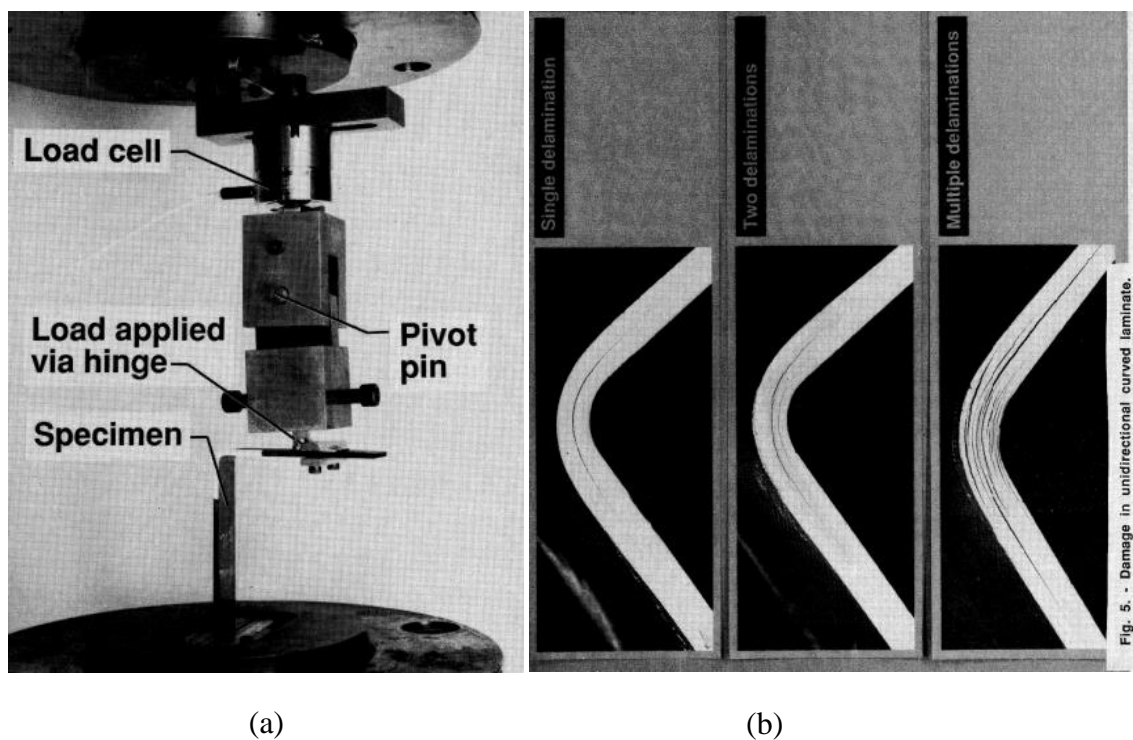


Figure 2.1.6 (a) Loading fixture (b) Delamination pictures taken during experiment [24].

In the analytical results, the radial, transverse shear and tangential stresses were calculated and the normalized distributions of stresses with respect to thickness at 25° from the lower arm were plotted. The highest radial stresses were placed in 42%

of thickness and the radial stress was found to be an order of magnitude higher than the transverse shear stresses through the thickness [20]. Besides, the tangential stresses were found to be maximum at the inner part of the curved region. In addition, elasticity solution for radial stresses was compared with FEA. Between 20° and 60°, they had a good balance.

In the next step of analytical calculations, the energy release rate (G) variation was calculated separately for both crack tips. Mode-I and Mode-II energy release rates were calculated separately to find out which mode is dominant in the crack front. In the left direction, G^I (Mode-I energy release rate) reached the maximum value at 22° and mode-II energy release rate values were ineffective when compared with the mode-I [20]. Same energy release rate tendency was obtained in the right crack tip. The magnitudes were different and the place of maximum G was 50°. The differences between these two crack tips were explained with G^{II} values. These explanations show the delamination growth in both arms individually. There is no explanation about the simultaneous crack growth. However, there are some explanations under the assumption that the crack grows in both arms equally. Near the crack nucleation point, the crack propagates in both directions equally but in large angles, the energy release on the left of left arm was higher than on the right one. From this information, a G criterion was developed. According to Martin's approach, if G value were greater than 2%, then the delamination would have grown at that direction. Otherwise, delamination grows in both directions equally. It is also noted that the delamination growth is unstable up to 60° due to the positive energy release rate values. In numerical analysis, after the initial delamination growth, the maximum radial stress in cracked specimen was obtained at the sublaminar of the structure without any load increase. Same phenomenon was shown in the experimental pictures.

In the last step, the failure load was predicted. From the stress analysis, the failure damage criterion was obtained, which is based on the assumption that the 'delamination occurs when radial stresses are equal to the interlaminar normal strength.'

In the NASA technical report "Damage prediction in cross-ply curved composite laminates", Martin and Jackson conducted an analytical and experimental work to

predict the delamination onset and growth in cross-ply curved composite laminate under static and fatigue loading. In analytical work, a closed form stress analysis was conducted to determine the stress distribution before failure. The strain energy release rate (G) was calculated with FEM. In the report, the focused failure type was delamination emanating from a matrix crack. Experimentally, cross-ply curved laminate were tested for static and fatigue loading for a comparison with the analytical results. Interlaminar tension delamination was predicted by comparing the maximum radial stress with the interlaminar tensile strength and the life data of composite. The matrix cracking was predicted by comparing the maximum radial and tangential stress in a 90° ply. And finally, delamination onset from a matrix crack was predicted by comparing the G values to the fracture toughness data [21].

In the cross-ply testing, the lay-up was chosen as $[0_4/90_3/0_5]_s$ (Lay-up A). Although, it was mentioned that the lay-up is not structurally applicable, it was chosen because the matrix cracks would occur in the tension loaded (90°) plies and the delamination would grow from them. Another lay-up in the experiments was $[0_4/90_3/0/90_2/0_2]_s$ (Lay-up B) (Figure 2.1.7)

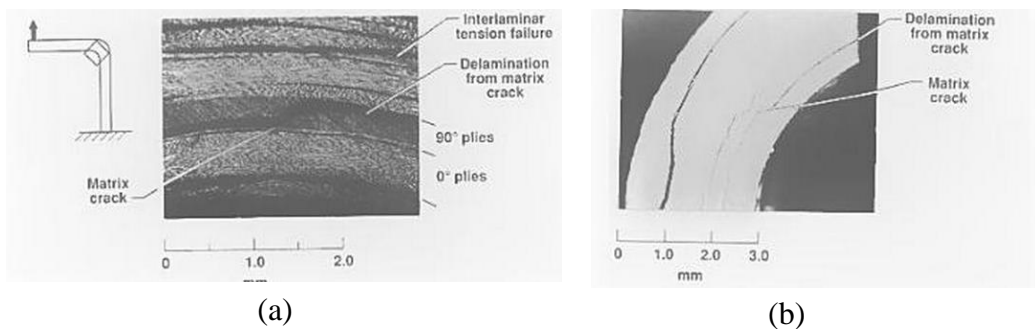


Figure 2.1.7 Damage in curved laminate (a) Layup-A (b) Layup-B [21].

In the report, some of the delamination pictures are shown. In the (Figure 2.1.7a) an interlaminar tension failure in the 0° plies and an oblique matrix crack in the tension-loaded 90° plies in lay-up A are seen. It was claimed that the sequence of occurrence was not known. In Figure 2.1.7b, a straight matrix crack was seen again at the 90° plies. Although it was not experimentally proved, it was thought that the matrix crack had occurred before the delamination.

In the report, the crack initiation path was to be determined with stress energy release rate analysis. Martin used a technique to characterize the path along curved region which consisted of comparing the values of G at each crack front and growing the delamination at the location of highest G . Based on this technique, he concluded that the strain energy release rate value (G) was highest at the inner right part of the curved region under previously described loading [20]. The unstable crack growth behavior was also explained with the upward trend of G values from the center to the leg of the specimen.

In the discussion part, several important outcomes were explained. For example, it was mentioned that the matrix cracks in laminate can be avoided by choosing the lay-up so that the tangential stresses in the 90° plies are not highly tensile. Another suggestion was to minimize free edge delamination by choosing the lay-ups with $90^\circ/0^\circ$ or $+45^\circ/-45^\circ$ interfaces where the radial stress is low [21].

In the paper ‘Composite failure prediction of single-L joint structures under bending’, Feih and Shercliff (2004) conducted experimental and numerical analysis on L-shaped joint members. Primary function of these parts is to transmit flexural, tensile and shear loads between two main parts [35]. The aim of the paper was to investigate failure predictions at adhesive bonding parts and curved parts of the joint members [35]. For this reason, they used specimens bonded to the base and to the rib structure. Between the L-part and the base, there is a peel fillet part in varied size and thickness. In the mechanical testing part, they applied transverse displacement on the joint rib part to create tensile loading on the inner part of the L-shaped part [35]. Although they described the loading scenario as ‘displacement controlled bending’, the loading case was the same with the shear loading which applied perpendicularly to the free arm (Figure 2.1.8)

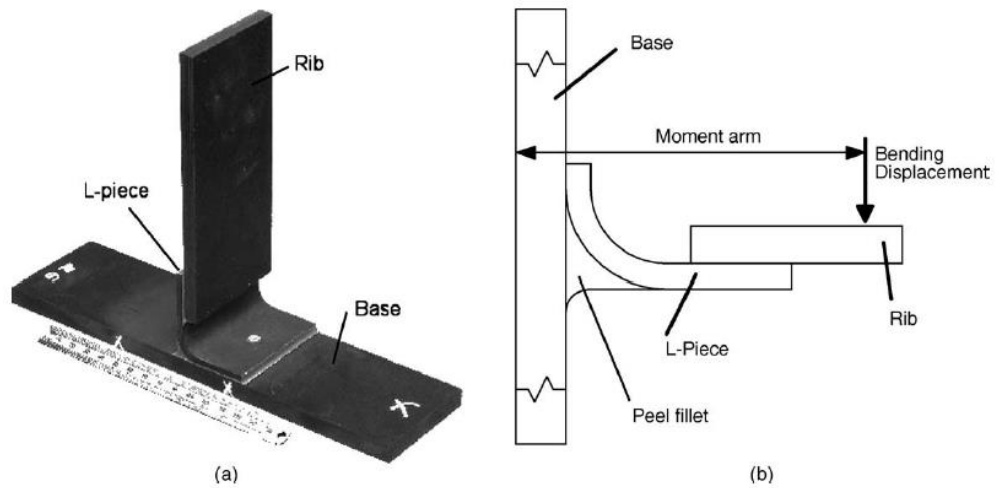


Figure 2.1.8 Single-L structure positioned between rib and base [35].

The material chosen was AS4-8552 uni-directional carbon fiber pre-pregs with HTA/977-2 epoxy matrix. In the laminate property calculations, the lamina is assumed to be transversely isotropic. Different lay-ups are chosen for the base, the rib and the L-shaped part. The sequence of L-shaped part is $[45/0/-45/90/45/0/-45/0]_s$ with 9 mm inner radius. After manufacturing process, they had 4mm thickness for 16 layers. They claim that the reason why they chose such a sequence and separated the $\mp 45^\circ$ plies by 0° and 90° plies is to minimize the interlaminar shear stress between the plies [35].

In the fixture, they clamped the base part of the specimen on a fixed plate, which restricted all movements in x- and y- directions. The strain recording method was chosen as strain gauge measurement. The data was compared with the numerical results. The strain gauge placement is shown in (Figure 2.1.9). There were six strain gauges. Two of them were placed on the rear side of the base plate, one of them was placed on rib section and the rest were on the L section. Although this method was highly efficient when it was compared with the numerical results, it only monitored local strain fields. Their first important observation was that the peel fillet details do not play an important role in the failure mechanisms [35]. In their experiments, variable failure loads, failure displacements and stiffness values were observed. The elastic stiffness in the experiments was in 10 % variation. On the other hand, the average strain gauge values were in good agreement with the numerical results.

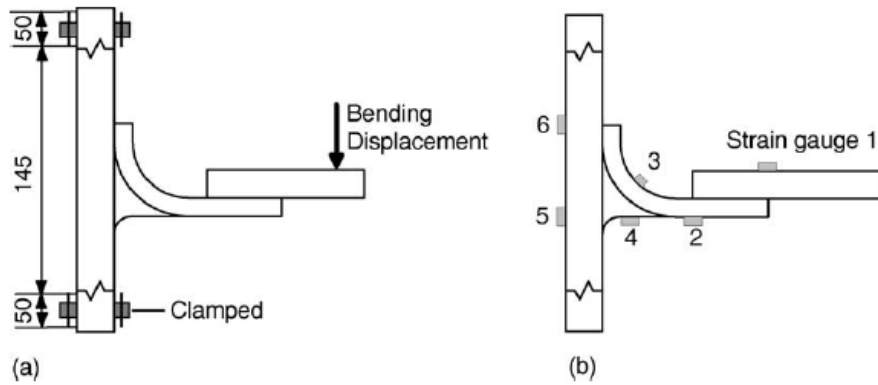


Figure 2.1.9 Joint structure and test details. (a) Loading arrangement (b) Strain gauge positions [35].

The preliminary analyses showed that the inner side of the curved region of the L-shaped laminate fails under tensile matrix cracking while the upper side fails under compressive matrix cracking. The effects of matrix cracks were obtained from the difference between strain gauge data. When the strain gauge data were compared with the numerical results, there were two important outcomes, which are summarized in the results. First, the numerical analysis without damage development was non-linear due to the elastic-plastic behavior of the adhesive. Second, contrary to the experimental data, no sudden jumps were observed in the numerical strain gauge values [35].

According to the failure model predictions, the initial failure mode was determined as tensile matrix cracking at the inner part of the L-shaped part which occurred in the 45° plies. The reason was that the 45° plies carry higher transverse stresses during loading. At the second stage, delamination initiation was predicted. Several failure criteria were combined at this stage to obtain the onset of delamination. In Figure 2.1.10, the predicted delamination location is shown which occur between the second (0°) and the third (45°) plies [35]. So the sequence of failure is summarized as follows: The initial failure mode was tensile matrix cracking while the second failure mode was compressive matrix cracking and final failure mode was delamination.

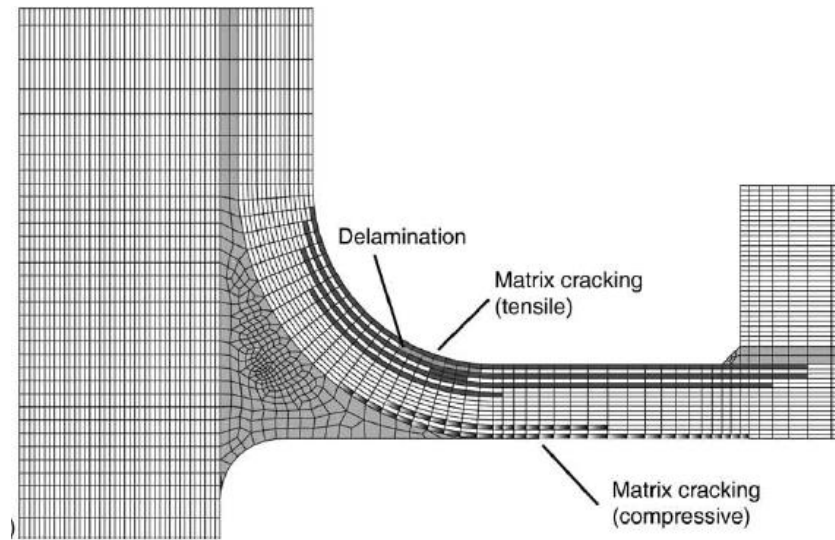


Figure 2.1.10 The predicted failure mechanism including delamination, compressive and tensile matrix cracking [35].

In his thesis (2004), Aki Vanttinen proposed a comprehensive study related to the delamination problem in rib foot corners. The main purpose of the thesis was to find a strength prediction method for the curved composite parts [19]. The strength analysis was conducted with 90° angled carbon fiber reinforced specimens. The typical loads and stress states at the curved part of the structure were presented. It is proposed that the out of plane stresses caused delamination which was calculated with a method developed by Lekhnitskii [36]. The applied loads were calculated from the numerical code and five different failure criteria are considered in the study. ASTM D6415 standard test method was conducted for out-of-plane tensile strength testing. And the out-of-plane shear strength was obtained with a newly designed testing method. In the final analysis, Puck Failure criterion was used for the prediction of the failure load [19].

In the introduction part, the most common application for the L-shaped parts was explained to be rib structures. The different rib structures were introduced well and the stress state of ribs was clarified. It was mentioned that the out-of plane shear and tensile stresses both cause delamination and that it was hard to separate them. The rib foot corner was defined as the L-shaped part that is bolted to the skin panel.

In the explanation of stress state of the rib foot corner, Vanttinen showed the radial stress (σ_r) and shear stress ($\tau_{r\theta}$) distributions through the curvature. The radial

stresses reached their maximum level at the angle 0° . It changes from tension to compression at the angle 37° . On the other hand; the shear stress reached its maximum level at 90° . Due to the change in the in-plane tension, the out-of-plane shear stresses decreased through the curvature [36].

In the experimental work, L-pull tests were conducted. The specified name of the test method comes from the shape of the specimen. The lower leg of the L-beam was bolted to the table and the upper part loaded parallel to the upper arm (i.e. pulled). Despite to the fact that it was not understood clearly, the lower plate was free to move in horizontal direction, although not frictionless. The angular displacement was restricted. This test was conducted to clarify the failure mode of composites under the specified loading conditions. The specimens were varied in stacking which include 0° , 45° and 90° oriented plies. In the analysis part, it was found out that the stacking sequence and the change in the corner radius had minor effects on the strength of the L-pull specimen. But it is worth to mention that the stacking sequences were the different combinations of 0° , 45° and 90° oriented plies, so it was not the comparison of uni-directional laminate stacking. However, the fiber volume fraction change had an important effect on the increasing strengths [19]. In the analysis, it was criticized that the numerical clamped boundary condition was not very accurate because in the experiments it was seen that structural response was elastic [19].

In the main part of the thesis, the critical failure loads with the critical positions were tabulated for different lay-ups. The loads were compared with the Tsai-Hill and Puck failure criteria based solutions. The failure angles are predicted with the Puck failure criterion, which was the interaction of out-of-plane shear and out-of-plane tension failure modes. The compressive radial stress were embedded in the failure criteria, since it was known by virtue of Kroll and Hufenbach that these stresses increased the fracture toughness against the out-of-plane shear due to the increased material internal friction [37].

In the paper “Computational and experimental investigation of delamination in L-shaped laminated composite components”, Wimmer et. al. (2009) conducted numerical and experimental study to understand the formation of delamination and growth of existing delaminations in L-shaped carbon reinforced epoxy resin. They

designed a test setup, which gives the dominant failure mode as delamination [38]. They had two types of test specimens (with and without the initial crack). Also the experimental results were compared with the numerical simulations. The main goal was to determine delamination growth with maximum principal strains, growth stability and structural response.

Due to the weakness of laminated structure strength in thickness direction, curved parts had delamination problems under loading. Delamination significantly changed the structural stiffness and the load carrying capacity of the specimen. Thus, it was considered as being one of the critical failure modes in laminated structures [39,40]. It is mentioned that the general failure behavior of composite structures was brittle. So, the local non-linearities around the delamination front can be neglected and Linear Elastic Fracture Mechanics (LEFM) can be used [41]. In the numerical work, based on LEFM, the Virtual Crack Closure Technique (VCCT) was used. In FEM analysis, Cohesive Zone Elements (CZE) had been developed [38].

In the terminology of their paper, the term ‘delamination emergence’ is defined as an initial delamination, which is formed in an intact interface [38]. In this paper, the delamination emergence and growth of unidirectional CFRP under quasi-static loading is being investigated in two steps. In the first step, specimens without any initial crack were tested and numerical simulations were conducted to discuss delamination emergence. In the second step, delamination stability was tested with specimens that have varied in initial crack length.

In computational part, strength/energy approach was used for delamination initiation prediction and semi-analytical approach was used for prediction of delamination growth. Also the phenomenon ‘delamination kinking’ was discussed. In crack kinking analysis, they wanted to discover when the delamination propagates between 0° and 90° layers, when the delamination front is oriented parallel to the 90° fibers or grows into the 0° ply through the fibers. Based on the failure criteria, they concluded that the crack had kink tendency under mode-I dominated mixed mode failures, proportional to the mode-II and mode-I stress intensity factor.

In the experiments, L-shaped structure was built up by UD 0° - 90° laminate. The ply sequence was determined according to the consistency with numerical results. From

the comparisons, the sequence was selected as $[0_3/90_3/0_3/90_3/0_3]$ i.e. the 0° and 90° layers were grouped by three [38]. The fixture was designed to create shear loading. The lower part of the specimen was bolted and clamped to a fixed part and the upper part of the fixture applied displacement loading perpendicular to the upper arm. In experiments, the local strain field was measured with 3D digital image correlation system. At this stage, it is important to emphasize that Wimmer’s paper was a numerically based study. The experimental studies were only used for the load-displacement curve comparison and primitive strain field visualization.

According to the numerical analysis, they computed the stresses with Puck FPF criterion. The crack initiation location was determined between 9th and 10th plies from the inner side within 30 plies. Another analysis was conducted and the critical initial delamination length with respect to delamination emergence load was calculated. The non-linear response of delamination was estimated by knowing the size and the location of critical initial delamination numerically (Figure 2.1.11) [38]. In the Figure 2.1.11, the dynamic response of delamination is shown. Load-displacement curve had a sudden drop with respect to the increase of the delaminated area.

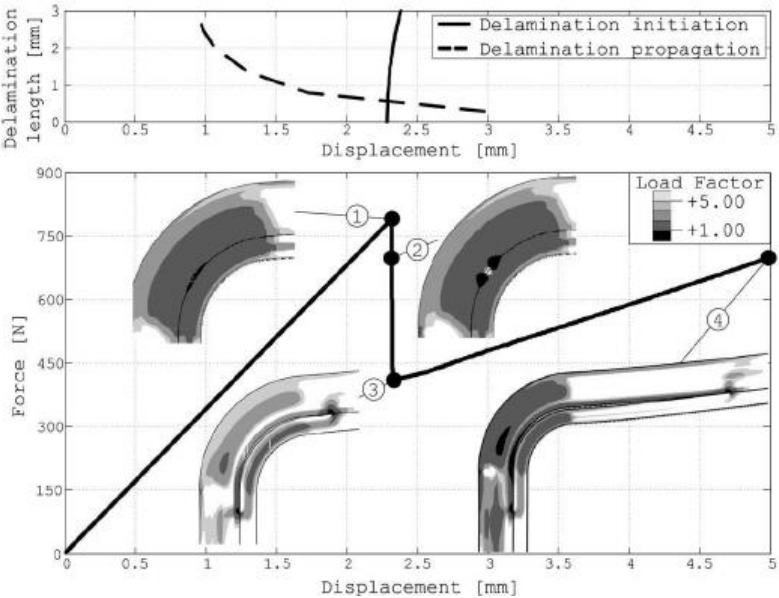


Figure 2.1.11 Predicted delamination process in the L-shaped laminate; delamination initiation curve and delamination propagation curve (top), structural response (bottom) [38].

Another important outcome of the numerical analysis was about the relation between initial delamination length and equilibrium load. Different initial lengths were analyzed and beginning from 1 mm initial crack length, the structural response was obtained to be unstable with the highest equilibrium load. Since the initial crack length was increasing, the equilibrium load and the corresponding displacement were decreasing. However, the delamination growth was still unstable. They continued to increase the initial crack length up to 5mm and they found out that the delamination growth was stable for large initial delamination sizes.

In the experimental results, the load-displacement curves of three specimens without the initial crack were shown and compared with the numerical predictions. Besides, instantaneous load drop with respect to unstable delamination growth was observed. But the elastic stiffness and the maximum loads varied (Figure 2.1.12). The variation between the experimental results was stemming from the manufacturing imperfections and the slipping problem between fixture and specimen during loading. In the second part, initial cracked specimens were tested. The kinking problem was seen in all specimens. According to the results, the delamination was initiated from the Teflon tape area and had grown across the 90° ply, and then had grown along the opponent interface.

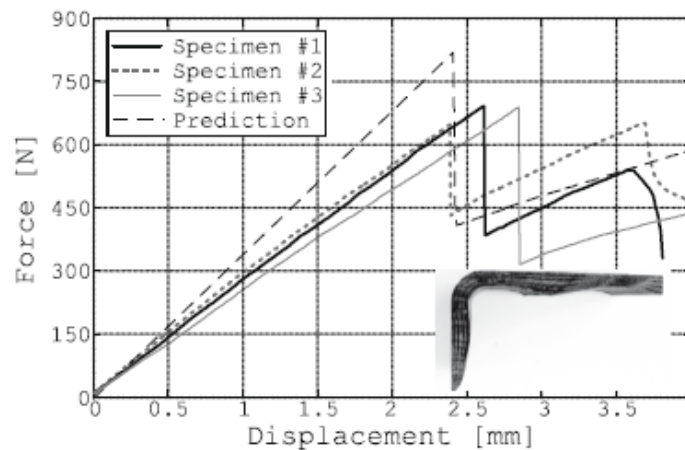


Figure 2.1.12 Measured and predicted structural response for L-shaped laminates without initial delaminations [38].

In the paper “Modeling of the dynamic delamination of L-shaped unidirectional laminated composites”, Gozluklu and Coker (2012) conducted numerical study to

understand the dynamic delamination growth of existing delaminations in L-shaped carbon reinforced epoxy resin. The delamination problem in L-shaped composite beams was investigated with 2-D explicit FEM model. The model consisted of 24 plies of CFRP unidirectional laminate with 1 mm pre-crack at the center of the curved part. The analysis was conducted with quasi-static axial loading that was applied parallel to the arm while the other arm was clamped. This loading type created different types of dominating stress states at the crack tips. One crack tip had opening stress dominated region and the other had shear dominated stress region. In the second step, the thickness of the specimen was changed and a second delamination growth was observed at the arm in this thicker laminate [42]. In the study, the radial normal stress (σ_{11}) and the shear stress (σ_{13}) were investigated through the thickness direction. The related stress distributions were calculated without pre-crack through the thickness. In addition, the stress state prior to the crack growth was calculated. The results show that the left side of the crack was under Mode-I dominance and the right side was under Mode-II dominance (Figure 2.1.13)

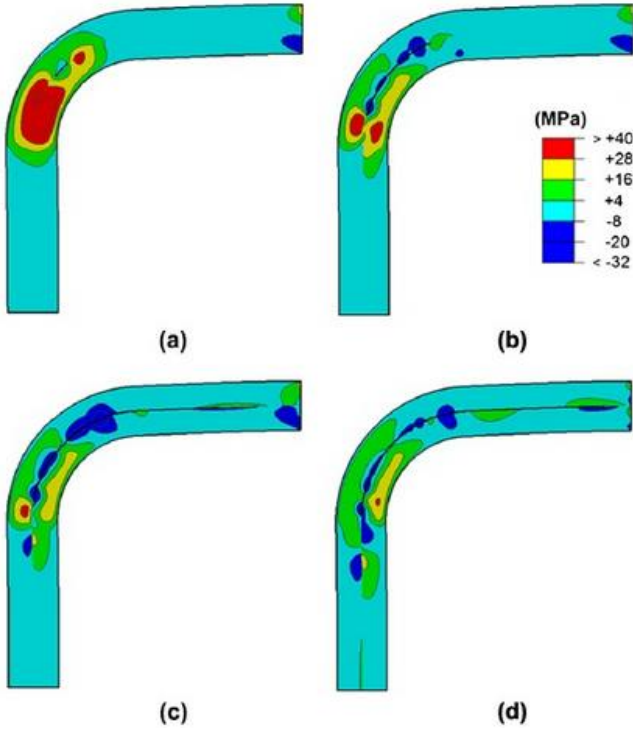


Figure 2.1.13 The stress contours during delamination initiation and propagation [42].

The innovative side of this study stemmed from the dynamic delamination growth under the mixed-mode stress state [42]. The FEM analysis was conducted both implicitly and explicitly. The load-displacement curves were compared. First, the crack growth was found to be dynamic, so it was claimed that the implicit analysis did not work during delamination propagation. The crack tip speeds were calculated differently in each crack tip, thus the mode-mixity influenced the crack tip speed regimes. Also, in the shear dominant region, the crack tip speed is higher. The dynamic effect of the crack was also shown from the perspective of energy. The kinetic energy distribution was found to be negligibly small up to the crack propagation and reached immediately to 40-50% of the Energy Release Rate value that indicates the importance of dynamic effects. When the same numerical analysis was conducted with a thicker laminate, another shear stress concentrated area was obtained at the arm, and there was a secondary crack nucleated from this point and merged with the pre-crack. It follows that, the shear dominance increases with thickness.

In the proceedings 'Failure analysis of woven fabric curved laminate with variable thickness', Zhang, Liu and Wang conducted an experimental and numerical work on the failure mechanism of the curved woven fabric laminates subjected to quasi-static loads. Four different stacking sequences were tested and they had three major outcomes. First, the failure mode for all specimens was delamination. Second, the failure location was close to the inner part and the failure was unstable and delamination growth was instantaneous [43]. In the numerical calculations, 3D FEM analysis was conducted using ABAQUS software and the circumferential stress distributions were obtained. It is seen that the radial stresses mostly intensify in the delamination area and radial stresses are high between different stacking angles.

In the experimental studies, four different stacking sequences were used. Each specimen included ($\pm 45^\circ$), (0° , 90°) woven plies with variable thickness. In the fixture, one leg of the specimen was clamped to the stationary of the loading machine and the other leg was bolted to the test jig. The load was applied by this moving part. A classical tensile testing fixture turned into the shear loading condition by this way.

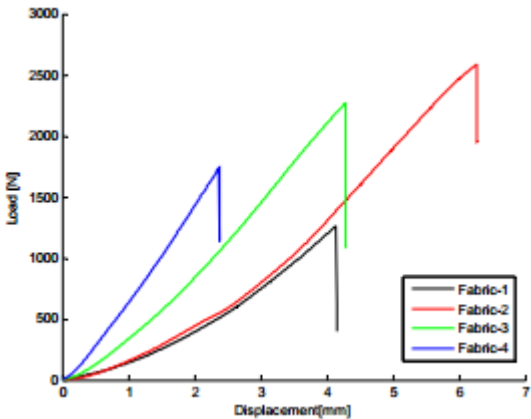
In their results, they did not hear any audible sound before failure and it is mentioned that high level breaking sound was heard during failure. The failure modes of all the

specimens are delamination [43]. But, the location of delamination was different for all cases. In two cases, delamination is initiated in the inner side of the laminate; and in the other cases, it started in the middle section of the thickness. In load displacement curves the stiffness of the laminate increases along with the increasing thickness [43]. But interestingly, the maximum value results did not depended this rule; the thickest laminate had the smaller maximum load than the other specimens [43] (Figure 2.1.14).

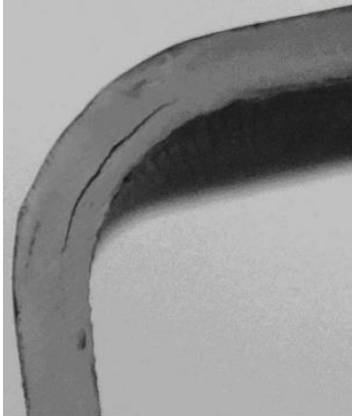
In numerical studies, they calculated the radial and tangential stress distribution along the circumferential direction. According to the results, radial stresses are maximum about 30° on the right of the lower side of the curved part and the tangential stress, which reached its maximum value 90° on the right of the lower part (i.e. beginning of the upper arm), was zero at this point. Another comparison included ply number vs. radial stress and tangential distributions. For different thicknesses, the radial stress distributions had similar trend. It was maximum between (0, 90) and (±45) layers at the inner part. It was shown that the differences in thickness do not affect the maximum radial stress value (Figure 2.1.15) [43].

Specimen No.	Stacking sequence
Fabric-1	$[(\pm 45)/(0,90)/(\pm 45)_3]_s$
Fabric-2	$[(\pm 45)/(0,90)/(\pm 45)_4]_s$
Fabric-3	$[(\pm 45)/(\pm 45)/(0,90)/(\pm 45)_4]_s$
Fabric-4	$[(\pm 45)/(0,90)/(\pm 45)/(0,90)/(\pm 45)_4]_s$

(a)



(b)



(c)

Figure 2.1.14 (a) Specimen configurations (b) Load displacement curves (c) Delamination in curved region [43].

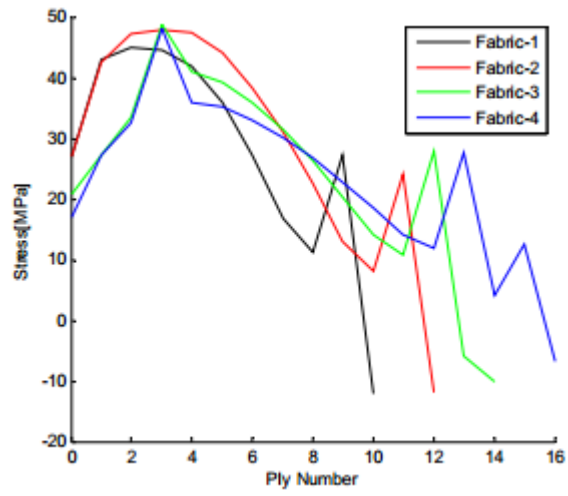


Figure 2.1.15 The radial stress along the thickness direction [43].

CHAPTER 3

METHOD

In this chapter, the experimental procedure is discussed. Firstly, the materials used in specimen manufacturing are introduced and the microscopic structures of the materials in the laminate are shown. Also, in this part, the manufacturing process of L-beams is explained. Secondly, the L-shaped geometry is introduced and the geometrical constraints of the laminates are tabulated. Therefore, laminate properties with the material wave speeds are calculated. Thirdly, the loading mechanism and fixture design process are summarized. And the parts of experimental setup are introduced especially the high speed camera details are discussed. Finally, the basic principles of the high speed monitoring and digital microscopy are explained. And, the specimen preparation steps for such a microscopic analysis procedure are itemized.

3.1. Material

In this study, three different laminate configurations are used, namely [0/90] fabric laminate with 12 plies, [0] UD laminate with 17 plies and [90/0] cross-ply laminate with 17 plies (Table 3.1.1). The first layup is a [0/90] fabric consisting of 12 plies of 5 harness satin weave fabric layers (Figure 3.1.1). The material is HexPly® AS4/8552 5HS carbon fabric pre-preg, which has 0.28 mm cured thickness. In this material form, carbon fibers bundled and woven repeatedly to float over four bundles, then under one. The satin weave produces a construction with low resistance to shear distortion and is thus easily molded (draped) over the complex shapes [52]. Because of these reasons, it is chosen for manufacturing the curved

geometries. The 12 plies of the specimen cannot be seen clearly in micrograph (Figure 3.1.1b) because of the meandering effect of the 5 harness satin texture plies.

The second lay-up is [0] UD which consists of 17 plies of 0° positioned UD pre-pregs (Figure 3.1.2). The unidirectional plies are laid through the thickness direction. HexPly® AS4/8552 UD carbon pre-pregs are used having 0.18 mm cured thickness. In this case, the micrographs are taken from both thickness (Figure 3.1.2b) and width (Figure 3.1.2c) directions. It is observed that the unidirectional pre-pregs, laid through the same direction, distort the laminated view of the composite specimen. In Figure 3.1.2c, this effect is seen clearly in width direction as waviness.

The third lay-up is bi-directional (cross-ply) lay-up, which has eight 0° and nine 90° plies in the order of 90/0 and 17 plies in total, beginning and ending with 90° fibers (Figure 3.1.3). In this case, the plies are easily recognized, even in the picture taken from the thickness direction by a regular camera (Figure 3.1.3a). Using pre-pregs in different orientations enables to create clear interfaces between the plies. In the cross-ply case, specimens are manufactured with different thicknesses and inner radii rather than discussed above. But, the lay-up of the all cross-ply laminates are same. In the specimen geometry part, all the specimens with geometrical configurations are shown. In this part, only the materials are discussed. In Table 3.1.2 the lamina properties of the pre-preg materials (HexPly® AS4/8552 5HS and HexPly® AS4/8552 UD) used in specimens are tabulated.

Table 3.1.1 The laminate orientation and the material type of the specimens used in the experiments.

Laminate Orientation	Number of Plies	Material	Type
$[0/90]_{6s}$	12	HexPly® AS4/8552 5HS	Weave Fabric Pre-Preg
$[0]_{17}$	17	HexPly® AS4/8552	UD Pre-Preg
$[(90/0)_4, \bar{90}]_s$	17	HexPly® AS4/8552	UD Pre-Preg

Table 3.1.2 Lamina Properties of the pre-preg materials.

	E11 (GPa)	E22 (GPa)	E33 (GPa)	v13	v12	v23	G12 (GPa)	G13 (GPa)	G23 (GPa)	ρ (gr/cm ³)
AS4/8552 UD	135	8.5	8.5	0.29	0.29	0.05	4.2	4.2	4.2	1.58
AS4/8552 5HS	55.7	55.7	62	0.30	0.05	0.30	4.2	3.7	3.7	1.57

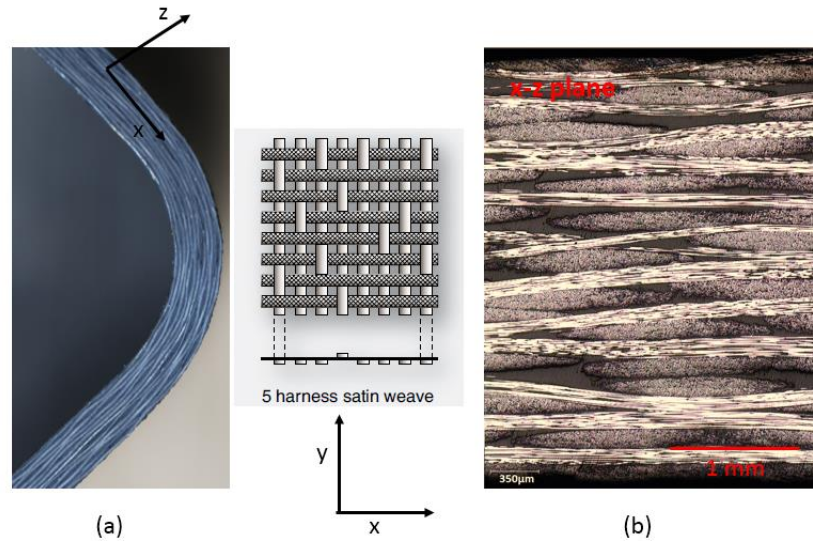


Figure 3.1.1 [0/90] Fabric specimen showing in thickness plane. (b) Micrograph of the specimen from x-z plane.

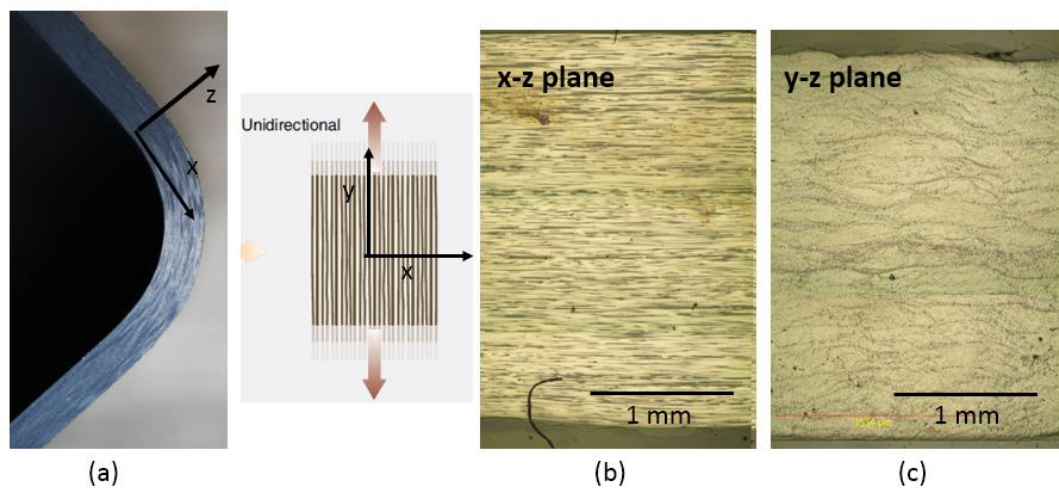


Figure 3.1.2 (a) [0] UD specimen showing in thickness plane (b) Micrograph of the specimen from x-z plane (c) Micrograph of the specimen from y-z plane.

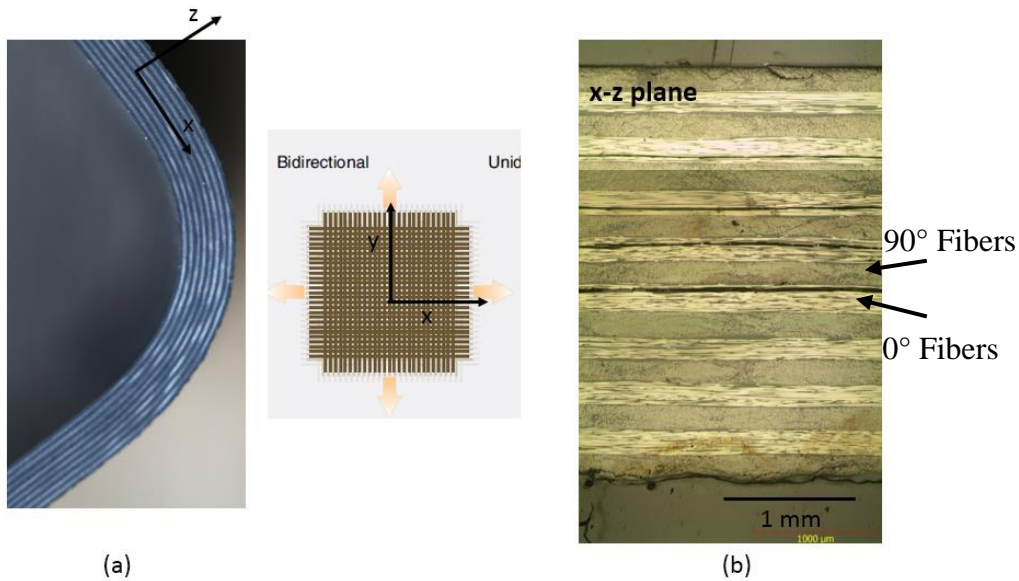


Figure 3.1.3 (a) [90/0] UD specimen showing in thickness plane. (b) Micrograph of the specimen from x-z plane.

3.2. Manufacturing Process of L-beams

The L-shaped specimens were manufactured using hand lay-up with the vacuum bagging technique. Right-angled aluminum male tool was used. Bagging systems for autoclave forming technique is frequently used in fabricating composite airframe components. When pre-pregs are combined with this technique, the production time and the manufacturing difficulties are decreased. The primary purpose of the bagging system is to hold the laminate in position and extract the excess quantity of epoxy [9]. It is critical to use sufficient amount of epoxy in composite manufacturing to prevent the over-stiffing of the material. In Figure 3.2.1a, a simple schematic shows the sequence of the bagging system. Before laying-up the pre-pregs, the tool is covered with the release agent. In our case Loctite Frekote 770-NC was used as a release agent to prepare the tool for the lay-up process [46]. When it comes to increasing the surface quality, the peel ply can be used at the inner and outer part of the laminate. But, we did not use in our case because the test specimen is not a surface component of an airplane. After the lay-up process of pre-pregs (Figure 3.2.1b), the bleeder and breather plies are placed (Figure 3.2.1c). The last stage is nylon bagging which is impermeable. On the nylon bagging, two or three small holes are opened and the vacuum gage ports are placed. A vacuum vent line and a pressure

gauge are mounted on these ports (Figure 3.2.1d). Specimens in the vacuum bag are sent to the autoclave for the curing process (Figure 3.2.1d). Autoclave pressure is applied to the outer surface of the bag. This pressure strengthened the mechanism to hold the composite materials stable during melting and curing. The autoclave is pressurized to 6.9 bar at the room temperature, then the temperature is increased to 180 °C with a rate of 0.5-3.0 °C/min at the constant pressure. The specimens are cured in autoclave for 180 minutes at the temperature 180 °C and pressure of 6.9 bars. Finally the temperature is decreased to room temperature with a rate of 0.5-3.0 °C/min, while the pressure is decreased gradually. The total curing time is approximately 10 hours [46]. After the autoclave process, the cured curved composite laminates are ready to be cut into specimen dimensions (Figure 3.2.1e). In the following section the final geometry of specimens are explained.

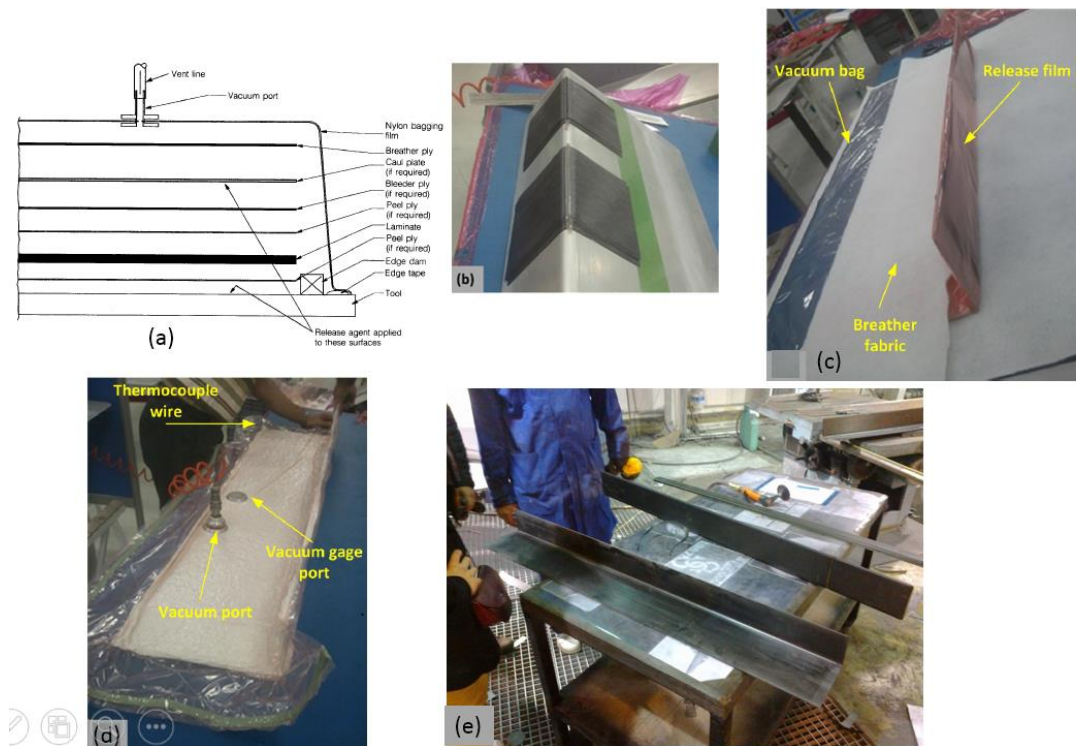


Figure 3.2.1 (a) Schematic of manufacturing process of composite laminate with hand lay-up technique (b) Hand-layup over the male tool (c) Preparation for vacuum bagging (d) Vacuum bagging process (e) After manufacturing process.

3.3. Geometry and Laminate Properties

3.3.1. Geometry of L-shaped beams

Manufactured L-shaped beams are in tool length size after curing (Figure 3.2.1). First step is to separate into 3cm-width pieces which refers flanges and brackets of the aircraft. In this thesis, the experimental procedure is conducted like coupon testing. The whole-scale testing is not conducted. The experimental set-up and fixture are suitable for coupon testing.

The geometry of the L-shaped composite specimen and the coordinate axes with respect to the composite specimen are shown in Figure 3.3.1a. The L-shaped brackets are formed of 90 mm lower arm, 150 mm upper arm, 10 mm inner radius, 30 mm width and 3 mm thickness. However, 12-layered fabric laminate has 3.36 mm thickness. A final version of L-shaped composite parts and the thickness vision of three different layers are also shown in Figure 3.3.1b.

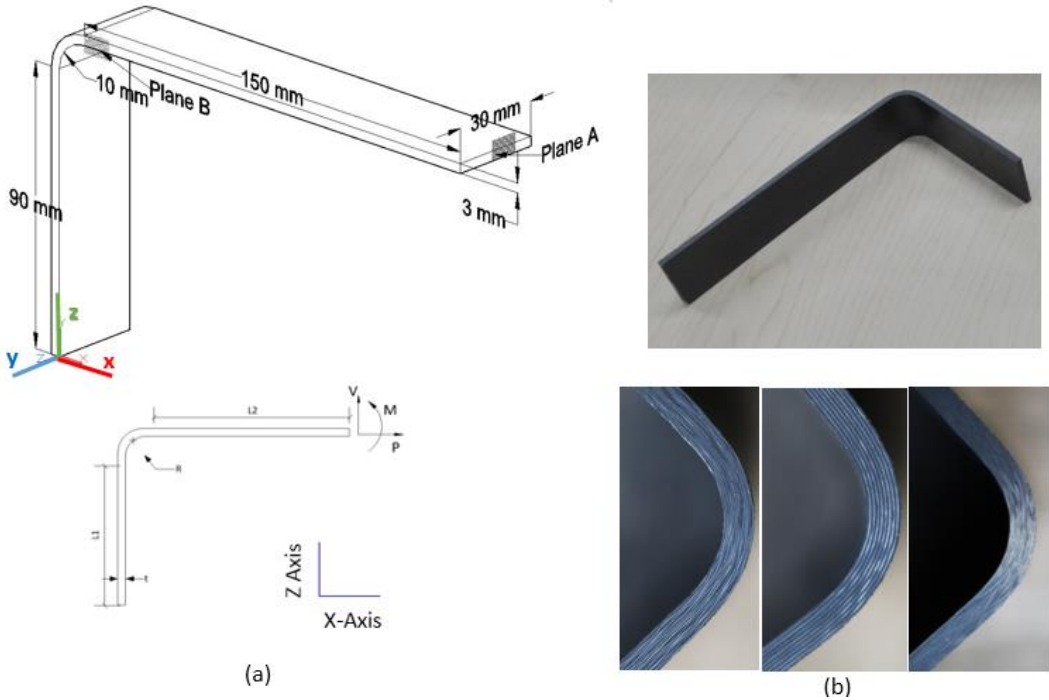


Figure 3.3.1 (a) The geometry of L-shaped specimen (b) The composite specimens for three different lay-up.

Table 3.3.1 Orientation, ply numbers, and geometrical constraints of specimens using in shear loading experiments.

Orientation	# of Plies	t (mm)	R_i (mm)	L_1 (mm)	L_2 (mm)	w (mm)
$[0/90]_{6s}$	12	3.36	10	90	150	30
$[0]_{17}$	17	3.18	10	90	150	30
$[(90/0)_4, \bar{90}]_s$	17	3.18	10	90	150	30
$[(90/0)_5, \bar{90}]_s$	21	3.95	10	90	150	30
$[(90/0)_6, \bar{90}]_s$	25	4.67	10	90	150	30
$[90/0]_{11}$	11	2.10	10	90	150	30
$[90/0]_7$	7	1.33	10	90	150	30
$[(90/0)_4, \bar{90}]_s$	17	3.18	5	90	150	30

L-shaped specimens were manufactured with some variable properties like number of plies, orientation and inner radius to use in shear loading experiments. In Table 3.3.1, the specimens are tabulated and dimensions are shown. Three different orientations are using as disused before which are uni-directional, cross-ply and 0/90 fabric orientations. The outer dimensions of the specimens keep same for reliable comparison. For the further comparisons with cross-ply laminates, the thickness of the laminates is changed (i.e. number of plies are changed) and the inner radius of the specimens is changed to 5mm. The experimental results and discussions about the differences are in next chapters.

3.3.2. Calculation of Laminate Properties

The coordinate axes with respect to composite specimen are shown in Figure 3.3.1a. To calculate the laminate properties of the material, the fiber distribution in the epoxy matrix is checked from the micrographs which are shown in Figure 3.1.1, Figure 3.1.2, Figure 3.1.3. $[0]_{17}$ and $[0/90]_{6s}$ lay-ups are assumed to be transversely

isotropic and $[(90/0)_4, \overline{90}]_s$ are assumed to be orthotropic. It is important to mention the assumption for the calculation for laminated composites.

- The laminate thickness (3mm) is very small compared to its other dimensions. For example, the thickness-to-width ratio of the composite is 1/10.
- The layers of the laminate are perfectly bonded.
- The lamina and laminate are linear elastic.

For orthotropic case, the relation between stresses and strains are shown as [48], in transversely isotropic case $c_{55}=c_{66}$,

$$\begin{bmatrix} \sigma_1 = \sigma_{11} \\ \sigma_2 = \sigma_{22} \\ \sigma_3 = \sigma_{33} \\ \sigma_4 = \sigma_{23} \\ \sigma_5 = \sigma_{13} \\ \sigma_6 = \sigma_{12} \end{bmatrix} = \begin{bmatrix} c_{11} & c_{12} & c_{12} & 0 & 0 & 0 \\ c_{12} & c_{22} & c_{23} & 0 & 0 & 0 \\ c_{12} & c_{23} & c_{22} & 0 & 0 & 0 \\ 0 & 0 & 0 & c_{44} & 0 & 0 \\ 0 & 0 & 0 & 0 & c_{55} & 0 \\ 0 & 0 & 0 & 0 & 0 & c_{66} \end{bmatrix} \begin{bmatrix} \epsilon_1 = \epsilon_{11} \\ \epsilon_2 = \epsilon_{22} \\ \epsilon_3 = \epsilon_{33} \\ \epsilon_4 = \epsilon_{23} \\ \epsilon_5 = \epsilon_{13} \\ \epsilon_6 = \epsilon_{12} \end{bmatrix} \quad (1)$$

The stiffness matrix has five independent parameters which are related to mechanical moduli of material (E_1 , E_2 , μ_{23} , μ_{12} and ν_{12}). The stiffness matrix components for orthotropic case expressed as,

$$c_{11} = \frac{1 - \nu_{23}\nu_{32}}{E_2 E_3 \Delta} \quad (2)$$

$$c_{22} = \frac{1 - \nu_{13}\nu_{31}}{E_1 E_3 \Delta} \quad (3)$$

$$c_{12} = \frac{\nu_{21} - \nu_{31}\nu_{23}}{E_2 E_3 \Delta} \quad (4)$$

$$c_{66} = G_{12} \quad (5)$$

$$\Delta = \frac{1 - \nu_{21}\nu_{12} - \nu_{23}\nu_{32} - \nu_{31}\nu_{13} - 2\nu_{21}\nu_{32}\nu_{13}}{E_1 E_2 E_3} \quad (6)$$

Under plane stress assumption, the stiffness matrix components are expressed with following equations for both transversely isotropic and orthotropic cases,

$$c'_{11} = \frac{E_1}{1 - \nu_{21}\nu_{12}} = c_{11} - \frac{c_{12}^2}{c_{22}} \quad (7)$$

$$\mathbf{c}'_{22} = \frac{\mathbf{E}_2}{\mathbf{1} - \mathbf{v}_{21}\mathbf{v}_{12}} = \mathbf{c}_{22} - \frac{\mathbf{c}_{23}^2}{\mathbf{c}_{22}} \quad (8)$$

$$\mathbf{c}'_{12} = \frac{\mathbf{v}_{21}\mathbf{E}_1}{\mathbf{1} - \mathbf{v}_{21}\mathbf{v}_{12}} = \mathbf{c}_{12} - \frac{\mathbf{c}_{12}\mathbf{c}_{23}}{\mathbf{c}_{22}} \quad (9)$$

$$\mathbf{c}'_{66} = \mu_{12} = \mathbf{c}_{66} \quad (10)$$

$$[\mathbf{A}] = \sum_{k=1}^N (\bar{\mathbf{c}}_{ij})_k (\mathbf{z}_k - \mathbf{z}_{k-1}) = \sum_{k=1}^N (\bar{\mathbf{c}}_{ij})_k \mathbf{t}_k \quad (11)$$

where $[\mathbf{A}]$ is the extensional stiffness matrix which is calculated using above expression where $\bar{\mathbf{c}}$ is the transformed stiffness of the ply at the position (\mathbf{z}) at which the stresses are being computed [47]. The laminate is taken as symmetric with respect to the center ply. The laminate properties for $[0]_{17}$ and $[(0/90)]_{6s}$ specimens are calculated using the following formulas (12-16). [47],

$$\begin{aligned} \mathbf{E}_x = \frac{\mathbf{A}_{11}}{\mathbf{h}} + \frac{\mathbf{A}_{12}}{\mathbf{h}} \left(\frac{\mathbf{A}_{26}\mathbf{A}_{16} - \mathbf{A}_{12}\mathbf{A}_{66}}{\mathbf{A}_{22}\mathbf{A}_{66} - \mathbf{A}_{26}^2} \right) \\ + \frac{\mathbf{A}_{16}}{\mathbf{h}} \left(-\frac{\mathbf{A}_{16}}{\mathbf{A}_{66}} + \frac{\mathbf{A}_{26}\mathbf{A}_{12}\mathbf{A}_{66} - \mathbf{A}_{26}^2\mathbf{A}_{16}}{\mathbf{A}_{22}\mathbf{A}_{66}^2 - \mathbf{A}_{26}^2\mathbf{A}_{66}} \right) \end{aligned} \quad (12)$$

$$\begin{aligned} \mathbf{E}_y = \frac{\mathbf{A}_{22}}{\mathbf{h}} + \frac{\mathbf{A}_{12}}{\mathbf{h}} \left(\frac{\mathbf{A}_{26}\mathbf{A}_{16} - \mathbf{A}_{12}\mathbf{A}_{66}}{\mathbf{A}_{11}\mathbf{A}_{66} - \mathbf{A}_{16}^2} \right) \\ + \frac{\mathbf{A}_{26}}{\mathbf{h}} \left(-\frac{\mathbf{A}_{26}}{\mathbf{A}_{66}} + \frac{\mathbf{A}_{16}\mathbf{A}_{12}\mathbf{A}_{66} - \mathbf{A}_{16}^2\mathbf{A}_{26}}{\mathbf{A}_{22}\mathbf{A}_{66}^2 - \mathbf{A}_{26}^2\mathbf{A}_{66}} \right) \end{aligned} \quad (13)$$

$$\mathbf{G}_{xy} = \frac{\mathbf{A}_{66}}{\mathbf{h}} - \frac{\mathbf{A}_{26}^2}{\mathbf{h}\mathbf{A}_{22}} + \frac{2\mathbf{A}_{16}\mathbf{A}_{12}\mathbf{A}_{22}\mathbf{A}_{26} - \mathbf{A}_{12}^2\mathbf{A}_{26}^2 - \mathbf{A}_{16}^2\mathbf{A}_{22}^2}{\mathbf{h}(\mathbf{A}_{11}\mathbf{A}_{22}^2 - \mathbf{A}_{12}^2\mathbf{A}_{22})} \quad (14)$$

$$\mathbf{v}_{xy} = \frac{(\mathbf{A}_{12} - \frac{\mathbf{A}_{16}\mathbf{A}_{26}}{\mathbf{A}_{66}})}{(\mathbf{A}_{22} - \frac{\mathbf{A}_{26}^2}{\mathbf{A}_{66}})} \quad (15)$$

$$\nu_{yx} = \frac{\left(\frac{A_{16}A_{26}}{A_{66}} - A_{12}\right)}{\left(\frac{A_{16}^2}{A_{66}} - A_{11}\right)} \quad (16)$$

The laminate properties are both calculated under orthotropic and transversely isotropic assumptions and the values are found to be very similar. Only the decimals are different.

The lamina properties for pre-pregs and engineering constants used in laminate property calculation are tabulated in Table 3.1.2. After calculating the laminate properties for $[0]_{17}$ and $[(0/90)_6]_s$ and $[(90/0)_4, \overline{90}]_s$ lay-ups (Table 3.3.2), the stiffness matrices are calculating.

Table 3.3.2 Laminate properties calculated for three lay-up using in experiments.

	E_x (GPa)	E_y (GPa)	G_{xy} (GPa)	ν_{xy}	ν_{yx}
$[0]_{17}$	135.0	8.5	2.8	0.35	0.02
$[(90/0)_4, \overline{90}]_s$	68.5	75.9	2.8	0.04	0.04
$[0/90]_{6s}$	55.7	55.7	2.8	0.05	0.05

3.3.3. Material Wave Speed Calculation

The calculated stiffness components were used in the dilatational, shear wave speed and Rayleigh wave speed calculations where \mathbf{c}_l^{\parallel} denotes the dilatational wave speed parallel to fibers while \mathbf{c}_l^{\perp} denotes the dilatational wave speed perpendicular to the fibers, \mathbf{c}_s is the shear wave speed and ρ is density (1.59 gr/cm³).

The relations between wave speeds and stiffness components are as follow [48],

$$\mathbf{c}_l^{\parallel} = \left(\frac{\mathbf{c}_{11}}{\rho}\right)^{1/2}, \quad \mathbf{c}_l^{\perp} = \left(\frac{\mathbf{c}_{22}}{\rho}\right)^{1/2}, \quad \mathbf{c}_s = \left(\frac{\mathbf{c}_{66}}{\rho}\right)^{1/2} \quad (17)$$

For the Rayleigh wave speed calculation following formula was used

$$\left(\frac{c'_{11}c'_{22} - c'^2_{12}}{c'_{22}c'_{66}} - \frac{\rho v^2}{c'_{66}}\right) \left[\frac{c'_{22}}{c'_{11}} \left(1 - \frac{\rho v^2}{c'_{66}}\right)\right]^{1/2} - \frac{\rho v^2}{c'_{66}} \left(1 - \frac{\rho v^2}{c'_{11}}\right)^{1/2} = 0. \quad (18)$$

The real root of this formula gives the Rayleigh wave speed.

By using the above formulas with the laminate and material properties, the wave speeds of the material for three different orientations are calculated as follows,

Table 3.3.3 Wave speeds of L-shaped composite laminates.

	c_1^{\parallel} (m/s)	c_1^{\perp} (m/s)	c_s (m/s)	c_R (m/s)
$[0]_{17}$	9250	2320	1330	1224
$[(90/0)_4, \overline{90}]_s$	6567	6916	1330	1224
$[0/90]_{6s}$	6547	6547	1550	1510

3.3.4. Error Analysis Method for Velocity Calculation

In experiments, the high speed camera images are used to measure the crack length and calculate the crack tip speeds. In the high speed images, the crack initiation point is found and taken as crack origin. The left and right crack lengths are calculated with respect to the crack origin drawing spline on the crack. Since the crack length measurement is carried out visually, there is an uncertainty range in the data. So, this range again calculated visually which can be expressed as $a+\Delta a$ with respect to time $(t+\Delta t)$. The crack tip speed velocity is calculating with using backward difference method from crack length vs. time data. The measurement error of the crack length data is transferred the velocity by using the following procedure;

$$v = \frac{a}{t} \quad (19)$$

$$\frac{\Delta v}{v} = \frac{\Delta a}{a} + \frac{\Delta t}{t} \quad (20)$$

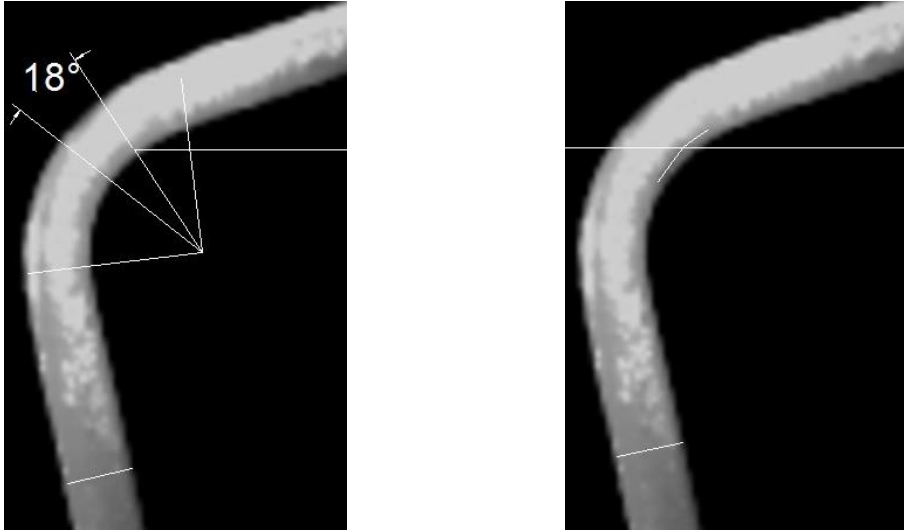


Figure 3.3.2 Example for crack length calculation.

3.4. Fixture and Experimental Setup

3.4.1. Fixture Design and Loading Condition

The L-shaped composite beam is subjected to the quasi-static shear loading perpendicular to the horizontal arm. The schematic of the experimental fixture that illustrates the loading condition for the L-shaped composite is shown in Figure 1.7.1a together with a photograph of the system in Figure 3.4.1b.

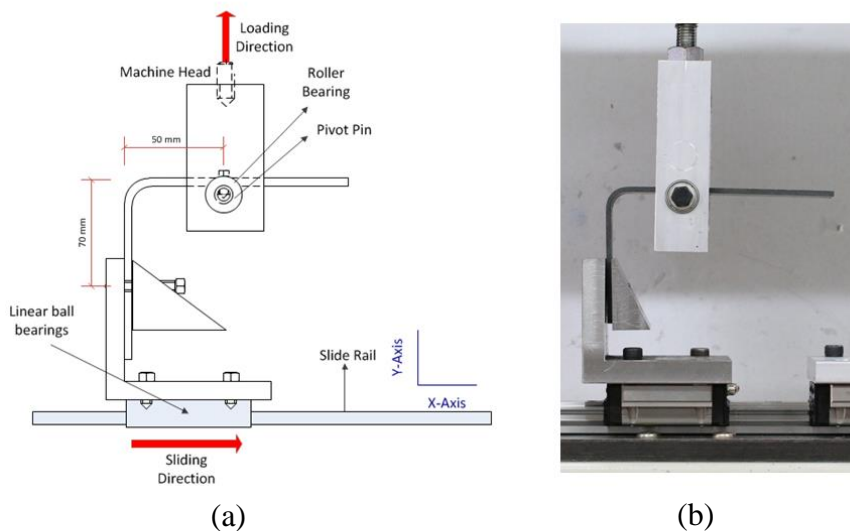


Figure 3.4.1 (a) Schematic of the loading fixture for perpendicular loading of the arm
 (b) Photo of the fixture and specimen before the experiment.

The vertical arm of the L-shaped specimen is clamped and bolted to the lower fixture. The fixture is mounted on a linear motion bearing system which is free to move along the x-axis. The sliding part of the fixture gives a smooth precise motion along the x-axis in order to avoid any reaction force along the x-axis to the upper arm [46]. The horizontal arm of the specimen is bolted to a pivot pin bearing system in order to fix the arm with respect to the corner of the specimen which is free to rotate around the z-axis. The fixture design is a challenge for providing pure shear loading. The previous numerical studies are considered to design the fixture [17,42]. The major point was to apply the exact boundary conditions in experiments. Therefore, a pure vertical load perpendicular to the upper arm is required to get rid of the horizontal forces and the moment at the contact point. In a previous study studying with same loading condition and boundary conditions, the development of fixture design was discussed [46]. Three different fixture types were used in experiments and the load-displacement data were compared with the simulation data.

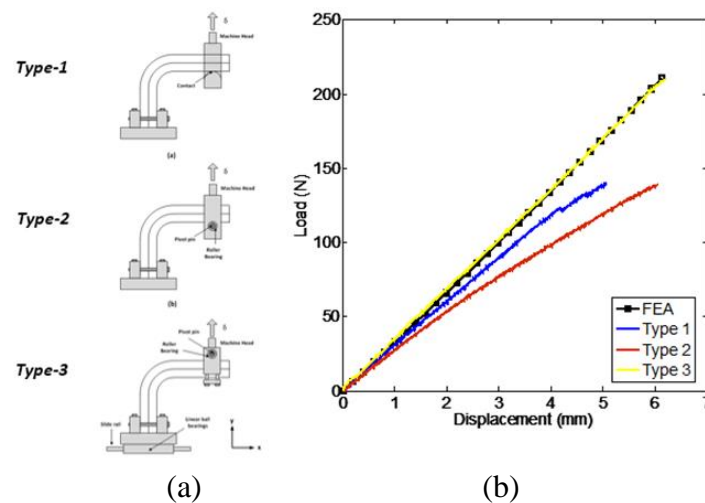


Figure 3.4.2 (a) Proposed and used loading fixtures to simulate the loading perpendicular to the upper arm of the L-shaped specimens. (b) Comparison of fixtures with the finite element analysis in terms of stiffness.

The load displacement curves and schematics of fixtures are shown in Figure 3.4.2a. Fixture Type#1 is designed so that the lower arm of the specimen is clamped while the perpendicular loading is applied to the upper arm with a line contact. The load displacement curve of this fixture (red line in Figure 3.5.1b) was found to be non-linear. The softening behavior was observed which was not fit to the brittle

characteristics of composites and it was due to the variable moment arm. Fixture Type #2, was similar to the shear loading fixtures in the literature [35, 38]. The lower arm of the specimen was clamped to the fixed part and at the upper arm of the fixture was mounted on a pivot pin system which is free to rotate. In these two fixtures, the loading application point changes as the arm rotates. So the same softening behavior was seen in fixture type #2 (blue line in Figure 3.4.2b).

Fixture Type #3 is designed so that the lower arm of the specimen is clamped on a slider platform to give a degree of freedom along the x-axis that removes the reaction force along the x-axis at the upper arm. And the upper part fixed to the fixture and the rotation was created with external pivot pin system on the same part. There was no softening behavior of the load displacement curve. Just as in the finite element model, the free movement of the platform prevented application of a horizontal force as the upper arm rotates. The slopes of load displacement curves were fit perfectly. Thus, Fixture Type #3 gives the boundary conditions represented in the finite element model accurately (Figure 3.4.2c), which is a perpendicular displacement applied to the upper arm [46]. In our study, same well-attested logic for lower arm of the fixture is used.

3.4.2. Experimental Setup

The experimental setup showing the fixture, loading and high speed camera system is shown in Figure 3.4.3. A Shimadzu Autograph AGS-J series with 10 kN capability screw-driven displacement controlled tensile-compression testing machine was used. All tests were conducted at a cross-head speed of 3 mm/min for quasi-static loading at the room temperature. Photron FASTCAM SA-5 high-speed camera system which records the images with framing rates of 7500 fps at full resolution of 1 MP and at 1,000,000 fps at reduced resolution were used. Since the delamination process had been expected to occur at least in the Rayleigh wave speed, the frame rates of 372,000, 420,000, 465,000 and 500,000 fps were chosen. A field of view of 17.5 mm x 15.7 mm is recorded using a 50 mm lens with 12.5 mm extension tubes during the experiment. Aerosol-Art Ral 9010 white color was used to paint the side of the specimen to create a contrast for better visualization of the delamination. The images are recorded continuously for about 4-5 seconds (2,000,000 frames at 120x64 pixels) and saved when the record button is triggered manually at the first crackling sound.

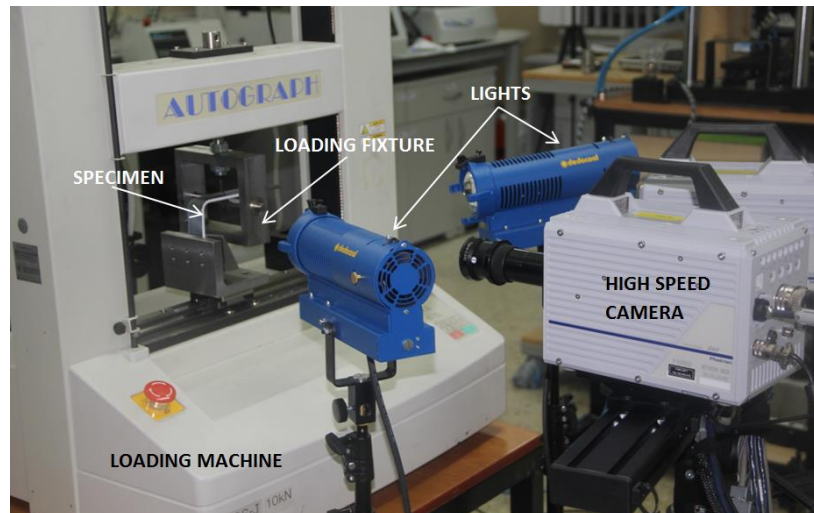


Figure 3.4.3 Experimental Setup

The time interval between the two pictures is from $2.7 \mu\text{s}$ to $1.9 \mu\text{s}$, where the complete delamination process lasts less than $20 \mu\text{s}$ in the camera records. The focused area can be captured by 64×120 pixels at the high frame rates. The detailed measuring parameters for each test are tabulated in Appendix A.

3.5. Microstructural Analysis

Another part of this study includes the micro-structural investigation of composites with an aim to understand their fracture mechanisms. Therefore, the tested specimens were prepared for a micro-structural analysis. The preparation of a specimen to find out its microstructure includes the following steps [50,51]:

-Sawing the section to be monitored: This process has a critical importance. The sawing process might be very slow in order to protect the fiber orientation in the epoxy and prevent the epoxy burnt. Diamond saw cutter was used in this process. The cracked specimen needs to be protected with plastic holders prior to cutting. Otherwise, the cracks can be enlarged or specimen can fall into pieces during the cutting.

-Mounting in resin: Cold mounting is used with vacuuming machine. Although the hot mounting process has the advantage of taking a lot shorter time than the cold mounting process, the hot mounting temperature exceeds the glass transition temperature of the composite. Hence, cold mounting is used despite the fact that its curing time is 24 hour. The air-bubble void, which affects the quality of the

visualization surface, was exploded under vacuum. A key factor for getting a good flat surface after the grinding process is to choose the strength of the epoxy and specimen holders close to the strength of the specimen.

-Grinding through coarse to fine the emery paper: This is a progressive process beginning with 400 grit waterproof SiC papers and finishing with 4000 grit emery papers. The whole process is lubricated with water to prevent the grinding surface from the epoxy burnt and to remove the grinding particles.

- Polishing with 3 μ and 1 μ diamond particle solution: To get clear pictures with high magnification factors (100x-200x) at small depth of field of a microscope is very difficult. The specimen has to be polished using rotating wheels that are covered with cloth and impregnated with a very fine abrasive solution. In our case, the filament diameter is 7.1- μ . Therefore; the abrasive compounds are chosen within the diamond paste interval of 3 μ to 1 μ .

-Washing with alcohol and drying with warm water: Clearing the finalized sample from lubricant and particles is important. The invisible marks can be very irritating under microscope. In the mid-steps, water is a good choice for cleaning up the product but in the final stage, it is critical to use a low-density fluid like alcohol, which dries quickly with warm air and prevents getting strained.

In Figure 3.5.1, the specimen preparation steps are shown. The tested specimens (Figure 3.5.1a) were cut through the width direction by using Micracut 101 high precision cutter (Figure 3.5.1b) and cold molding with epoxy in VACUMET cold molding vacuum extractor (Figure 3.5.1c). The several grinding and polishing processes were conducted with Minitech 223 grinding machine with cloths and emery papers (Figure 3.5.1d). The final view of microscope samples is shown in (Figure 3.5.1e).

The samples were analyzed with Leica DMi1 inverted microscope with 5x, 10x and 20x objectives and 10x camera magnification factor (Figure 3.5.2a). In the analysis, the whole crack, which is seen in the high-speed camera, was observed under the microscope. The aim was to clarify the crack position in the layers. For this reason, multiple pictures were taken on the cracked surface and stitched together to get the micrograph of the whole curved part. In Chapter 4, the pictures are discussed.

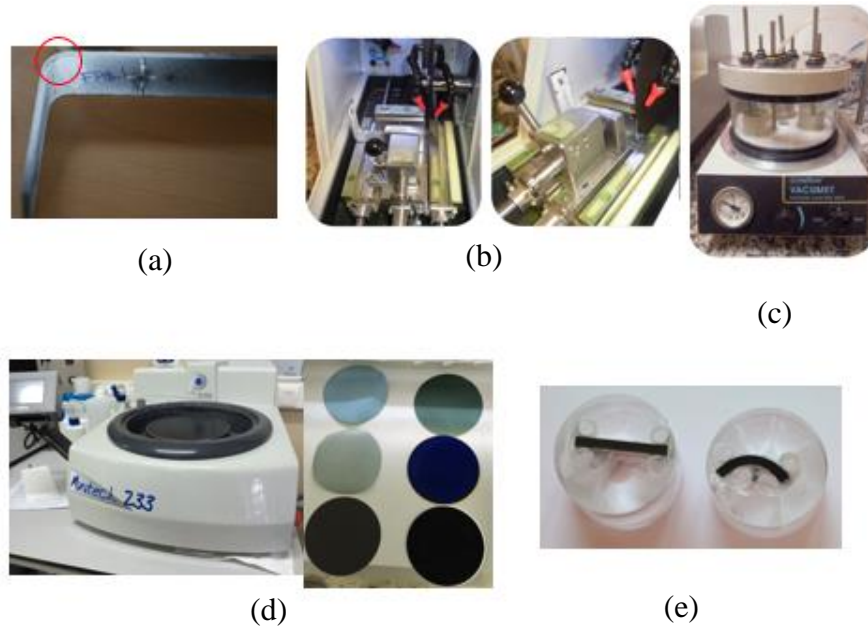


Figure 3.5.1 (a) Monitored area (b) Cutting process (c) Cold molding with vacuum extractor (d) Grinding and polishing process (e) The final view of microscope samples.

The fibers orientation into epoxy for three different lay-ups was seen in Figure 3.5.2b with 100x magnification.

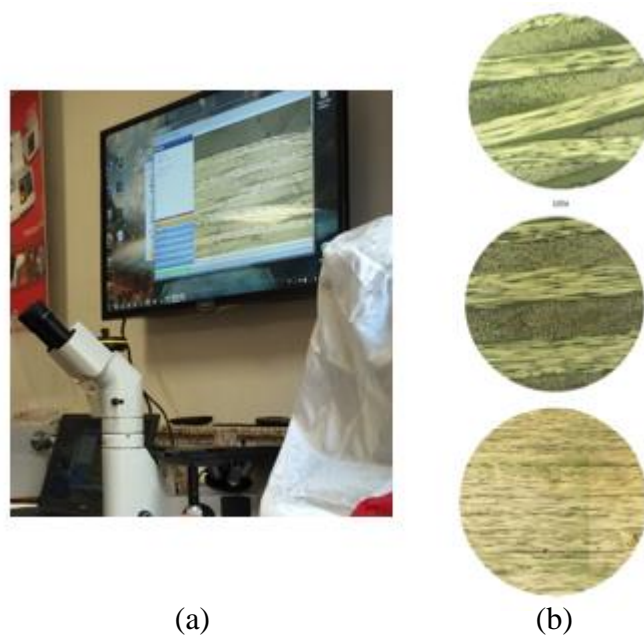


Figure 3.5.2 (a) Monitoring process with Leica DMI1 microscope (a) Micrographs of specimens.

CHAPTER 4

EXPERIMENTAL RESULTS

In this chapter, the results of quasi-static shear loading experiments that are conducted with the L-shaped CFRP specimens are discussed. Results for three different lay-up configurations: [0/90] woven fabric, [0] UD and [90/0] cross-ply specimens, are chosen for the testing procedure. The stress fields obtained from finite element simulation of L-shaped laminates are discussed in Sec. 4.1 to help in discussing the experimental results. The experimental results are first presented for (0/90) fabric lay-up in Sec. 4.2 followed by experimental results for [0] UD lay-up in Sec. 4.3. In Sec. 4.4, the experimental results of [90/0] cross-ply lay-up are discussed in three parts. In Sec. 4.4.1, detailed experimental results for 17-ply [90/0] cross-ply with a baseline ply number of 17 and inner radius of 10 mm is discussed. In Sec. 4.4.2, the effect of thickness on delamination behavior of [90/0] cross-ply is presented. Finally, Sec. 4.4.3, the effect of inner radius of 5 mm on a 17-ply [90/0] laminate is presented. In all sections, observations are discussed at three scales. At the macro scale, the load-displacement curves of the experiments are compared. At the mesoscale, the failure process and sequence are presented and the crack tip speeds are calculated. At the micro scale, the micrograph of cracked specimens are shown and discussed.

4.1. Stress Fields

The numerically predicted stress fields of the L-shaped specimen under shear loading are discussed in this section. It is important to be aware of the spatial distribution of the stress components before discussing the experimental results. The stress fields prior to the delamination initiation are taken from the recent numerical study about the same configuration and material of [0/90] fabric specimen [17]. The numerical study was conducted using explicit finite element method in conjunction with the

cohesive zone modelling in ABAQUS/Explicit FEA commercial code. For more information about the numerical study, please look at [17].

In Figure 4.1.1, the stress contour of the radial opening (normal) (S_{33}), shear (S_{13}) and longitudinal (S_{11}) stresses are shown for [0/90] fabric laminate prior to delamination nucleation. As it is seen in Figure 4.1.1, the opening stress is maximum (40 MPa) at the center of the curved region which is around 42% of the thickness measured from the inner radius [17]. On the other hand, the arms of the specimen are dominated by the shear stresses with the shear stresses reaching then maximum values at four distinct locations at the end of the curved region (42 MPa). For the longitudinal stresses, the maximum location as expected from beam bending theory is obtained at the inner side of the laminate to be 646 MPa. The stress distribution for the fabric laminate will be used to discuss [0] UD case, qualitatively, since, both lay-ups are taken to be transversely isotropic.

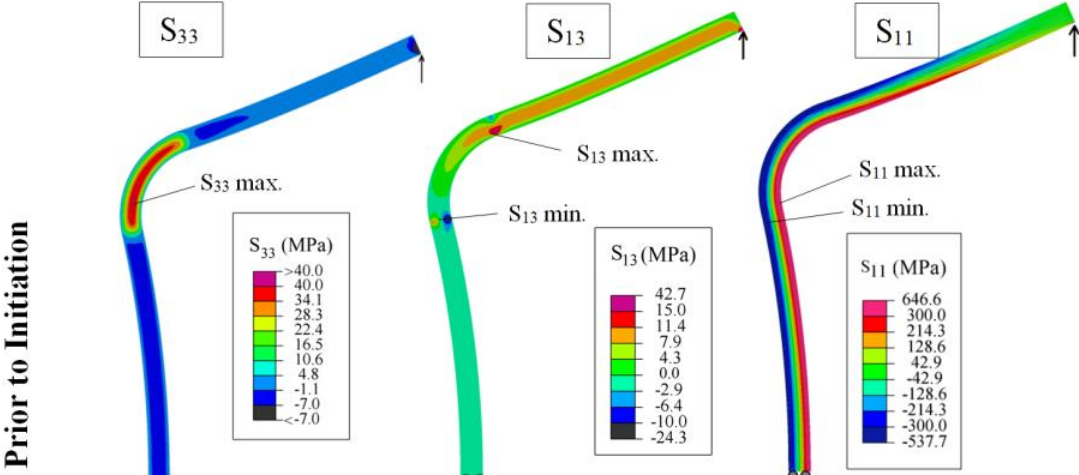


Figure 4.1.1 Numerically predicted normal (S_{33}), shear (S_{13}) and longitudinal (S_{11}) stress distributions in the [0/90] fabric L-shaped composite laminate prior to delamination initiation [17].

Stress distribution plots are presented for the [90/0] cross-ply case. In Figure 4.1.2, the stress contours of the radial opening (normal) (S_{33}), shear (S_{13}) and longitudinal (S_{11}) stresses are shown for the [90/0] cross-ply laminate prior to the delamination nucleation. Same distribution with the fabric case can be seen. The mid part of the curvature is dominated by the opening stresses, the arms are dominated by the shear stresses and finally the inner part of the curvature is dominated by the longitudinal

stresses. However, the maximum normal stress becomes 30 MPa whereas the maximum longitudinal stress increases to 980 MPa as compared to the fabric material. In the following sections, the experimental results will be discussed using these stress fields.

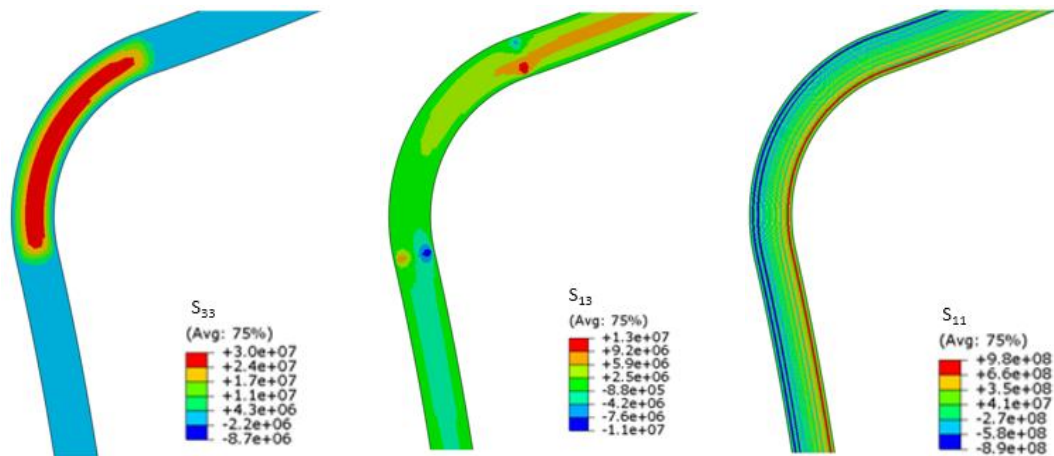


Figure 4.1.2 Numerically predicted normal (S_{33}), shear (S_{13}) and longitudinal (S_{11}) stress distributions in the [90/0] cross-ply L-shaped composite laminate prior to delamination initiation [53].

4.2. Experimental Results of [0/90] Fabric Lay-up

The first results belong to the [0/90] fabric L-shaped specimens. The lay-up details are explained in the method part. 8 different tests were conducted. In Appendix B, the load-displacement curves are tabulated. In this part, only three of the experiments are discussed.

The load displacement curves of the L-shaped composite laminates are shown in Figure 4.2.1. The results of the experiments F1, F2 (from 1st batch) and F6 (from 2nd batch) are presented in which the load increases with displacement in the linear elastic region before a sudden load drop is observed at the point of delamination. Both experiments F1 and F2 yielded similar stiffness and maximum load values of 38.8 N/m and 743 N, respectively, with a 20% variation. The result of F6 was slightly different than F1-F2 since it was from a different batch. Its maximum load and stiffness values were calculated as 931 N and 43.7 N/m, respectively. The sudden load drop is associated with the delamination initiation and propagation. It should be noted that, during the loading, a low level crackling sound, which is

attributed to matrix cracking, is heard at 60-70 % of the maximum load. However, no effect on the load-displacement curves is observed. At the instance of the load drop, a sudden high level breaking sound is heard in real time.

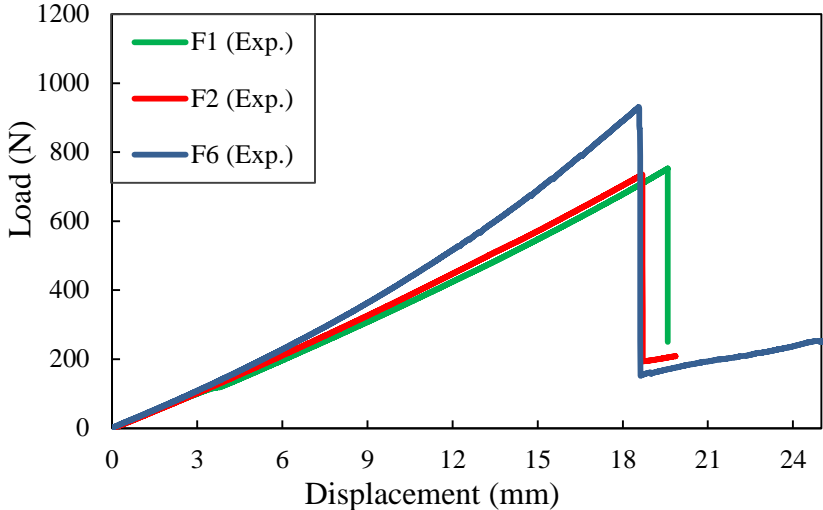


Figure 4.2.1 Load-displacement curves for [0/90] weave fabric tests.

After the crack propagation ended, single or multiple delaminations were seen on the specimen, starting at the curved part and propagating to the arms. After the load drop, load carrying capacity of the specimen decreased substantially to almost 30% of the maximum load and at that point the experiment was stopped. Both experiments yielded similar stiffness values and maximum load values of 38.8 N/m and 743 N, respectively, with a 20% variation. The general pictures of the specimen mounted on the fixture are seen in Figure 4.2.3. The specimen just before the loading is shown in Figure 4.2.3a and the specimen after the failure and before the unloading is shown in Figure 4.2.3b. The angle of the curvature of the failed specimen with respect to the non-failed specimen is calculated as 31°.



Figure 4.2.2 The cracked surface of F2 after failure.

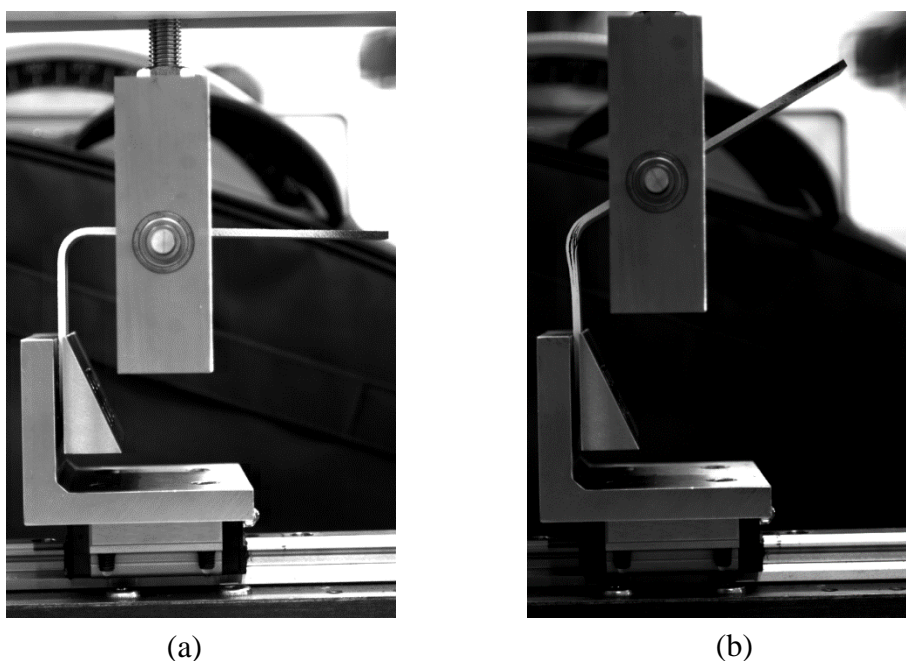


Figure 4.2.3 Photograph of the L-beam fabric specimen in the test fixture (a) before starting the shear loading test and (b) after the failure.

Figure 4.2.4 shows the high-speed images of the curved region during the initiation and propagation of delamination. The step between two frames is $1.9\mu\text{s}$. The crack initiates between the 5th and the 6th plies at 12° left from the center of the curved region and then grows to both arms (Figure 4.2.4b). During the crack formation, some fiber bridging can be observed at the crack surface (Figure 4.2.4e). The delamination, then, propagates rapidly in both directions into the arms, leaving the field of view in $10\mu\text{s}$ (5 frames). As the delamination grows, the separated plies are

seen to be oscillating and they are damped after 4 cycles. The oscillation frequency was calculated from the high speed images as 31.2 kHz in the curved region. A second crack nucleates at the right arm between the 10th and the 11th plies and comes into view at 510 μ s after the first crack nucleation (Figure 4.2.4g). The first seven pictures in Figure 4.2.4 belong to the experiment F2, where the camera was focused on the curved region. On the other hand, the last two pictures, which were captured when the camera was focused on the lower arm of the specimen, belong to the experiment F6. The major challenge of the experiments is the ratio between the capturing area and the recording speed. In higher frame rates, the capturing area is getting smaller (for detailed information—Ch. 3). Because of that, two different experimental results are merged in the solutions.

The crack lengths are measured from the images until the crack leaves the field of view. The crack tips are located by the naked eye, seeking the last black pixel of the crack area. The crack tip locations that are measured from the crack nucleation point as a function of time, for both the right and left crack tips, are shown in Figure 4.2.5. The data of the specimen used in the experiments F1, F2 and F6 are combined in Figure 4.2.5. However, the right crack tip could not be traced after a while because the arm leaves the field of view due to the rotation of the specimen. In Figure 4.2.5, it can be seen that the right and the left crack lengths for the specimen F2 follow the same pattern. The crack length evolution of the experiment F1 exhibited similar behavior to that of the experiment F2.

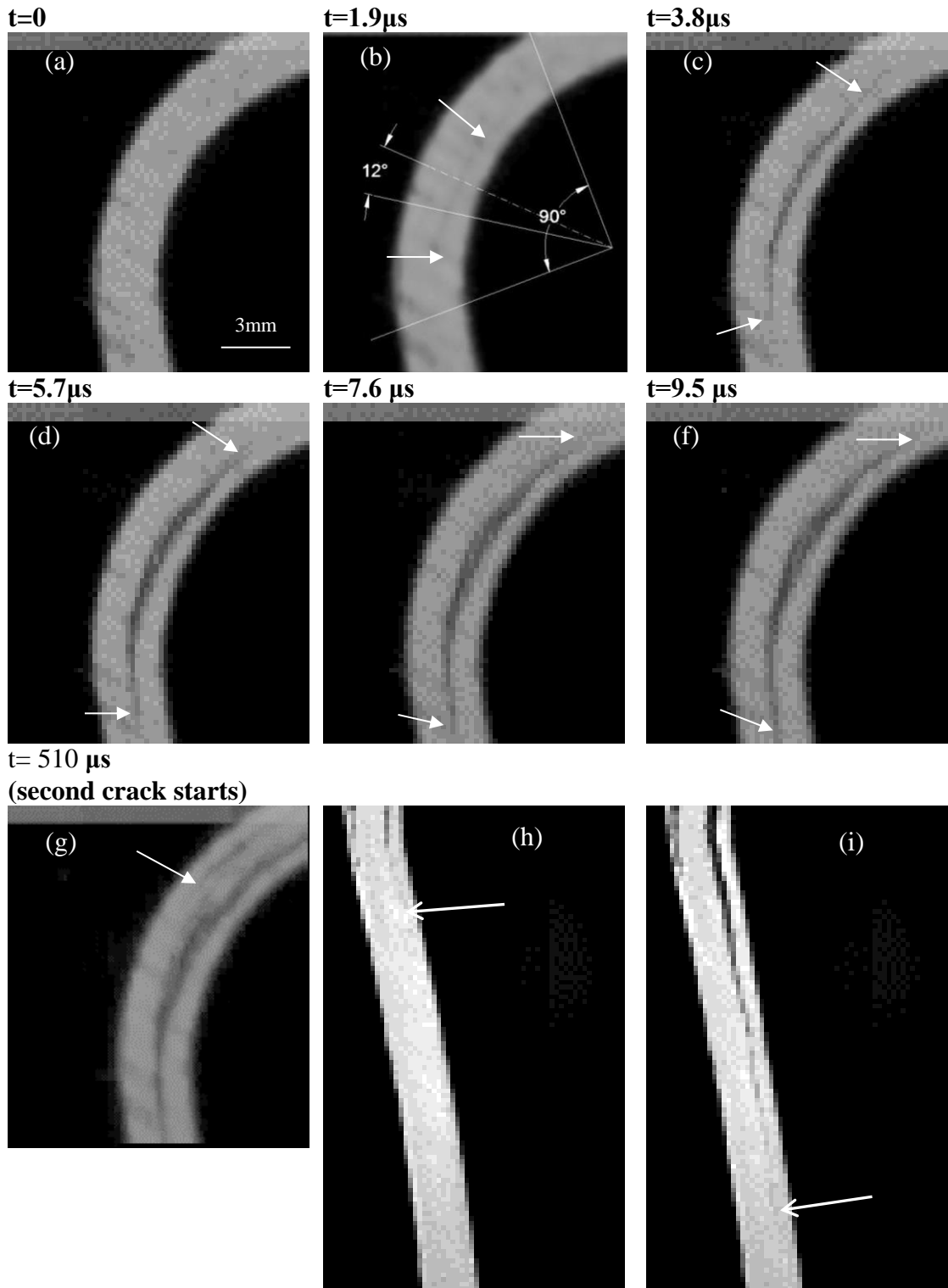


Figure 4.2.4. High speed camera images of the $(0/90)_{6s}$ fabric CFRP L-beam laminate: (a-g) 15.7 mm by 17.5 mm field of view in the curved region at 1.9 μ s time interval showing delamination initiation and propagation (experiment F2), (h-i) 32.0 mm by 16.4 mm field of view in the vertical arm with 2.7 μ s time intervals showing delamination propagation (experiment F6).

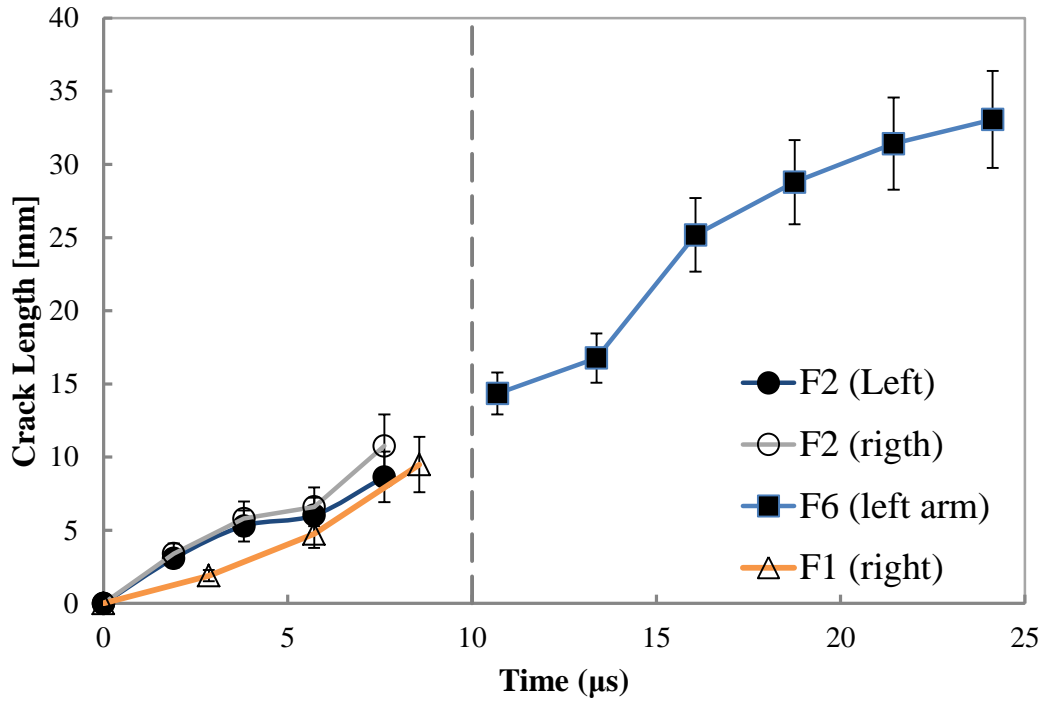


Figure 4.2.5. Crack length as a function of time for the left crack tip (solid symbols) in the curved region (Experiment F2) and the arm (Experiment F6) and the right crack tip (open symbols) in the curved region only (Experiments F1 and F2).

In the first image of the crack, the left crack tip is measured as 3.08 mm and the right crack tip is measured as 3.41 mm. In the following two frames, the crack propagation in both directions has unstable growth rate. In the last picture, just before leaving the field of view in the curved region at 10 μs , the crack growth has an upward trend for both experiments and crack tips. For a time greater than 10 μs , the results of a second experiment are superposed in the plot, where the camera is focused on the left vertical arm. The crack length difference between the two successive images increases up to 9 mm at this part. When it is compared with the curved region, the progression rate has higher values. The left and the right crack tip speeds are calculated from the crack length data, using backward difference method.

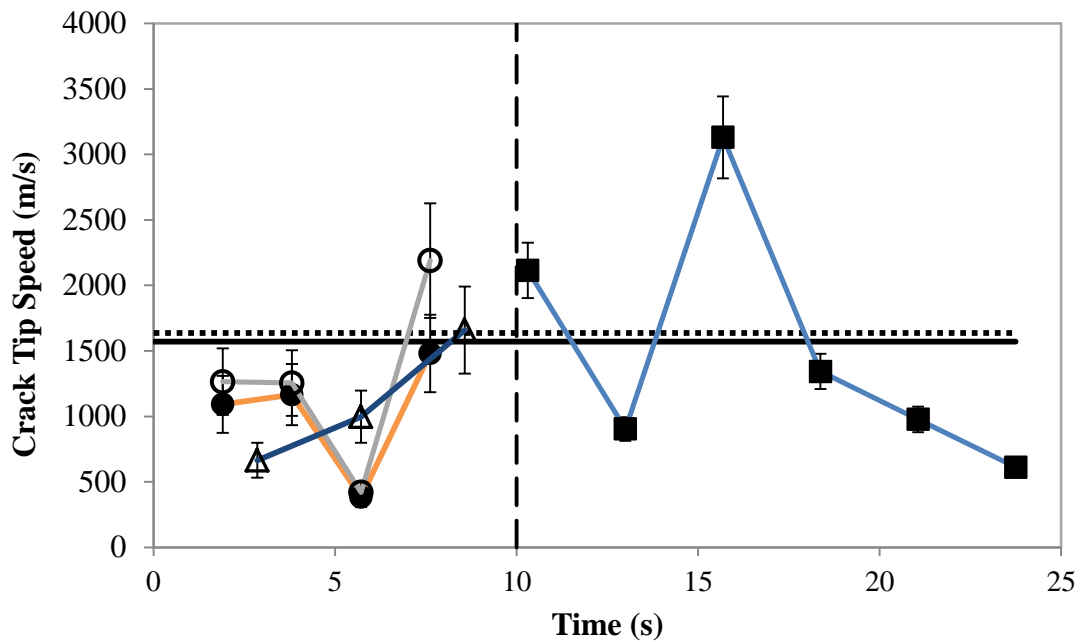


Figure 4.2.6. Crack Tip Speeds as a function of time for the left crack tip (solid symbols) in the curved region (Experiment F2) and the arm (Experiment F6) and the right crack tip (open symbols) in the curved region only (Experiments F1 and F2).

The crack tip speeds as a function of time are given in Figure 4.2.6 for the right and the left crack tips. In specimen F1, delamination initiated at 1200 m/s in both crack tips whereas in specimen F2 delamination initiated at 600m/s. But both experiments increased up to 2000 m/s at the end of the curved region. The crack tip speeds in the vertical arm were calculated for the specimen F6. The crack tip speed values increased from sub-Rayleigh to intersonic speeds around 2000 m/s at the vertical arm. In the third experiment (Exp. F6), the crack entered the field of view in the vertical arm at 2200 m/s, went up to 3200 m/s, and then slowed down to 500 m/s before arresting.

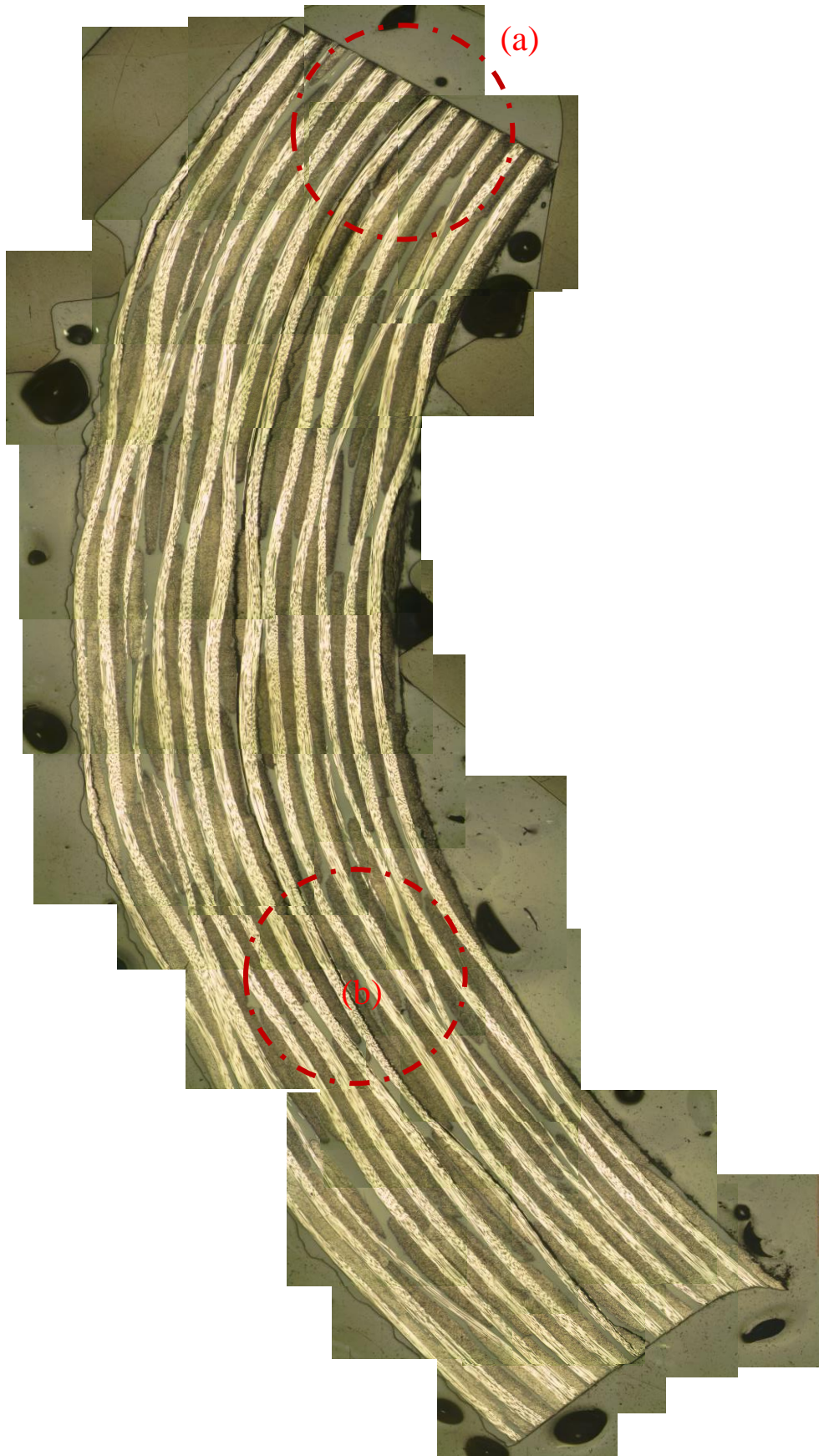
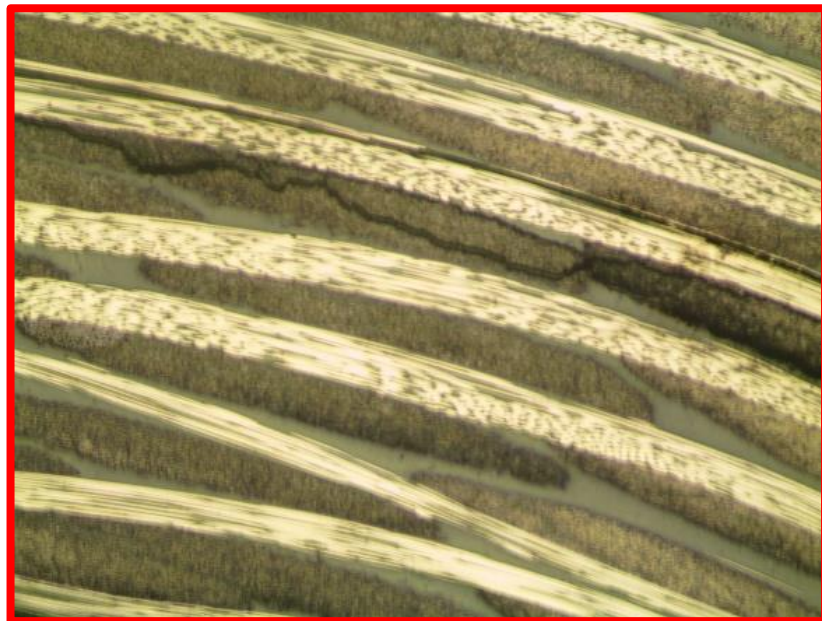


Figure 4.2.7 Micrograph of a [0/90] fabric specimen in general view.



(a)



(b)

Figure 4.2.8 Micrograph of a [0/90] fabric specimen with close-up of cracked regions (a) Cracked surface near the legs (b) Cracked surface near the middle part of curvature.

The tested specimen (F2) was cut through the width direction and the surface to be inspected was prepared for the microscope. The process was reported in section 3.4. Micrographs were taken through the cracked surface and merged to display the crack in the curved part. In Figure 4.2.7 and Figure 4.2.8, the micrograph result for the fabric specimen is shown. Before explaining the crack initiation details, some comments about the general view of the cracked surface are summed up in the following;

- The whole area contained in the field of view of the microscope was captured and stitched to see the crack that was discussed, using high-speed camera pictures. For this purpose, 60 microscope pictures were stitched.

- The dark parts in the laminate are 90° fibers and the light parts are 0° fibers. As it was discussed in the method part, the laminate has 12 plies and the waviness in the laminate is due to the 5HS weave of the fabric material.

In the upper part of Figure 4.2.8, it can be seen that the delamination is located at the 5th interface. The 90° and 0° group of plies form the texture of a single ply. Because of this, the light and the dark areas are counted as a single layer. The delamination had been in progress between the 90° and 0° interface. At the mid part of the curved region, another crack, which was placed one ply above the main crack, was seen. These two cracks move parallel to each other through the curvature. The second crack goes into the 0° plies and displays different behavior compared with the first crack. In the mid part of the curved region, the crack meanders in the 90° ply (Figure 4.2.7). But away from the mid part, the crack is parallel through the interface of 0° and 90° plies.

4.3. Experimental Results of [0] Uni-Directional Lay-up

The second lay-up to be investigated is the 17-layered 0° uni-directional L-shaped specimen. The lay-up details are reported in the method part (Ch. 3). The load-displacement curves of the three different $[0]_{17}$ experiments under quasi-static shear loading are shown in Figure 4.3.1, after a linear elastic loading behavior, a load drop occurs at failure, to less than 15% of the maximum value. An instant high level breaking sound was heard during load drop. After the crack propagation ends, multiple delaminations were observed post-mortem. After the load drop, the specimen lost all its load carrying capacity. In Figure 4.3.1, the loading stiffness shows a large variation.

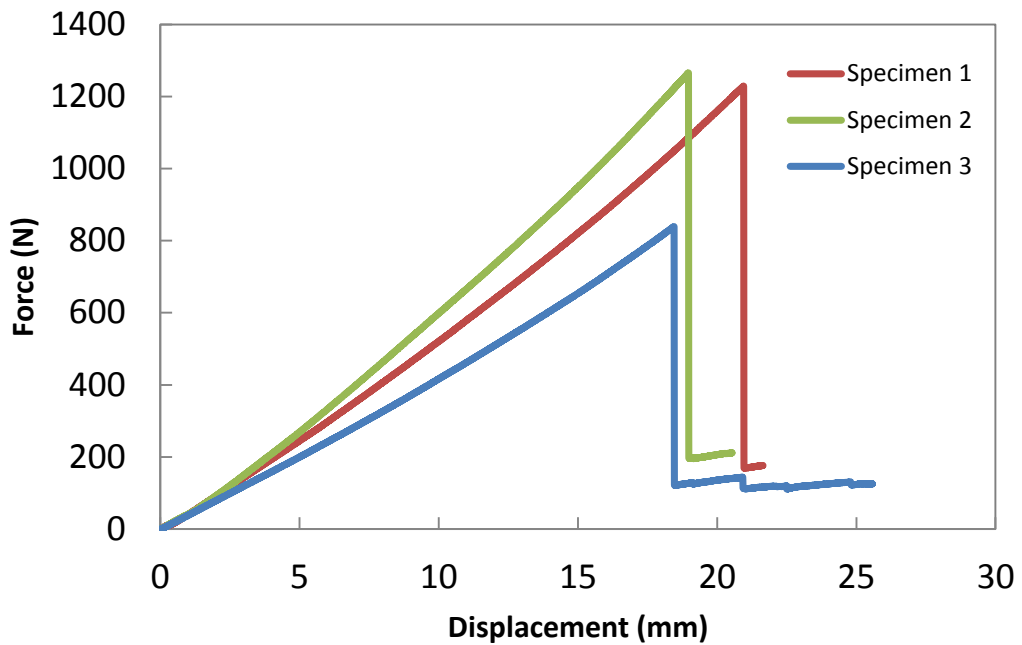


Figure 4.3.1 $[0]_{17}$ specimen load displacement curve under perpendicular loading.

In Figure 4.3.2, the high speed camera images of the Specimen 1, captured during delamination initiation and propagation, are shown. The time interval between the two pictures is $1.613 \mu\text{s}$, and the total time for process is approximately $20 \mu\text{s}$. There are several observations as a result of high speed monitoring. An initial crack occurs in the mid-part of the curved region (Figure 4.3.2b). After the initial crack grows to 17.5 cm, the second and the third delaminations (Figure 4.3.2c) start simultaneously and they are placed symmetrically with respect to the first crack tips. Secondly, the

multiple delamination process is observed for whole part of the curvature through the thickness (Figure 4.3.2f), which explains the loss in the load carrying capacity. In Figure 4.3.3, a general picture of the failed specimen is shown after the failure.

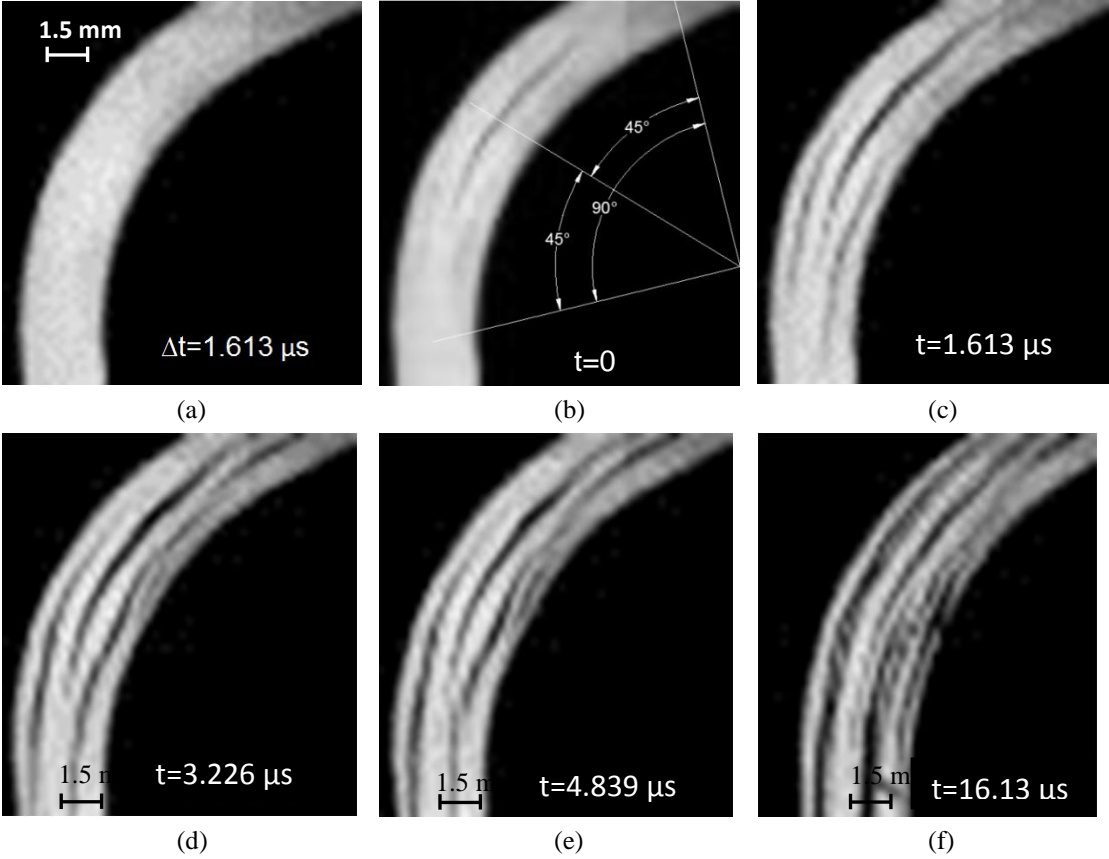


Figure 4.3.2 High speed images of Specimen 1 taken at 620000 fps.

The right crack tip location as a function of time was determined from the high speed pictures, starting from the nucleation point (Figure 4.3.4a). The average crack tip speeds are calculated using the backward difference method. In Figure 4.3.4b, the right crack tip speed is shown together with the material wave speeds (the shear wave speed (C_s), Rayleigh wave speed (C_R) and dilatational wave speeds parallel and perpendicular to the fiber directions (C_I^{\parallel} , C_I^{\perp})). The first calculated speed (1033 m/s) is already close to the Rayleigh wave speed of the material (1224 m/s) and then reaches the intersonic speed (2401 m/s) as the crack tip under mixed mode, which was discussed in [48].



Figure 4.3.3 Picture of the [0] UD specimen after failure.

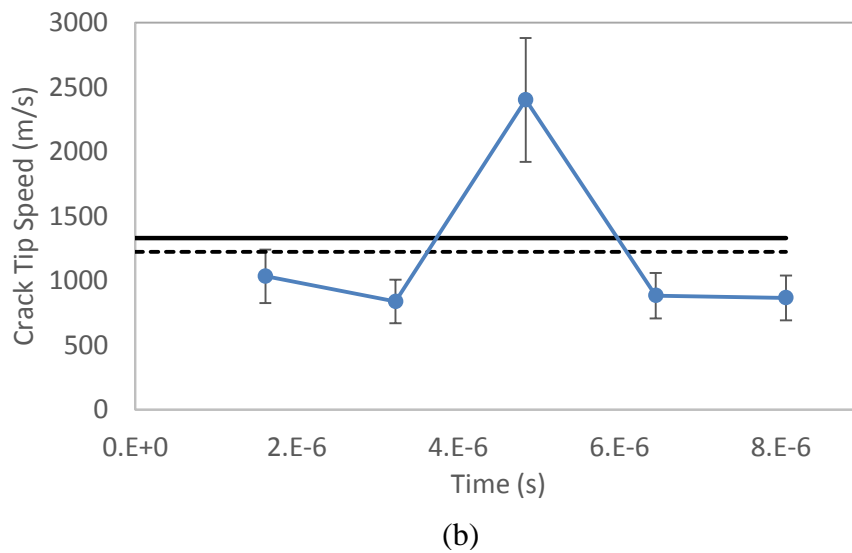
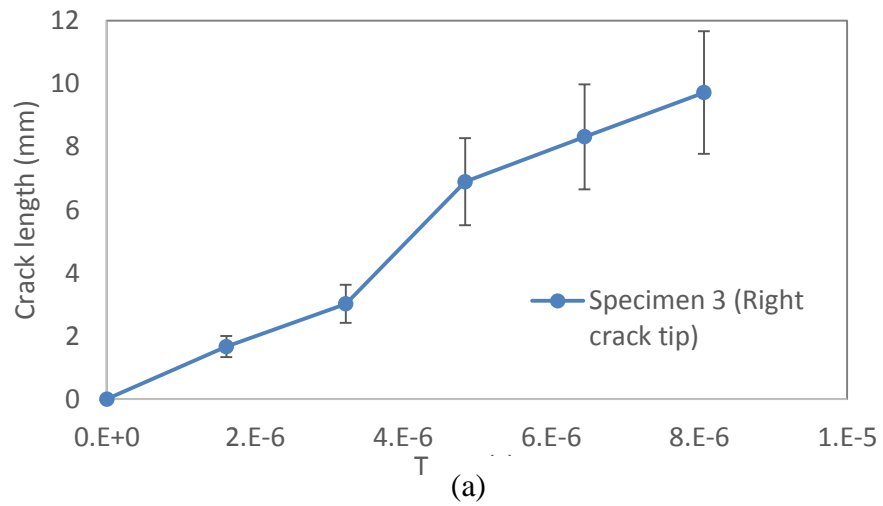


Figure 4.3.4 (a) The right crack tip progress during delamination propagation (b) Crack tip speed history for the initial crack of [0]₁₇ specimen under perpendicular loading.

4.4. Experimental Results of [90/0] Cross-ply Lay-up

4.4.1. [90/0] Cross-ply Lay-up with 17 plies and 10 mm inner radius

The same experimental procedure was conducted for the $[(90/0)_4, \overline{90}]_5$ cross-ply oriented laminates. In Figure 4.4.1, the load-displacement curves of the three different specimens are seen; there are three or four sudden load drops corresponding to the delamination initiation and propagation which is a different delamination propagation concept than the other specimens. When the failed composite specimens were reloaded, they continued carrying the applied load with a slightly lower stiffness. After reloading, it is seen that the maximum load before the next load drop reaches to 75 % of the un-damaged specimen's original load carrying capacity. During the loading, low-level crackling sounds were heard, which are thought to be corresponding to the matrix cracking. The "crackling sound" started at 65%-70% of the maximum load. But, the effect on the load-displacement curves of these small cracks is not observed in the load-displacement data.

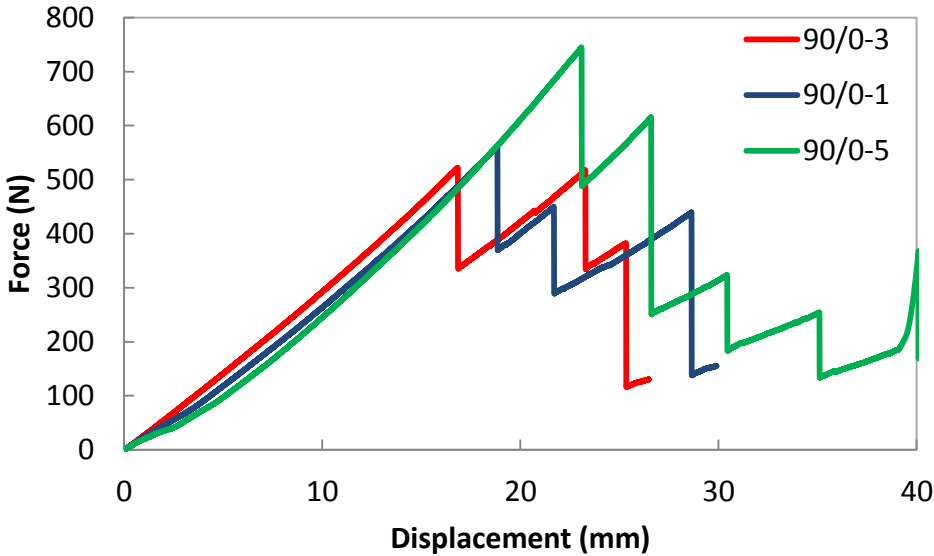


Figure 4.4.1 Load displacement of the [90/0] specimens curve under perpendicular loading.

The high speed camera results for the Specimen 3, taken at 465000 fps, show the failure details. In this case, a much more different failure mechanism was observed. In the first load drop (Figure 4.4.2a), a single delamination nucleates near the inner radius, 13° left of the mid part. This single delamination propagates all the way through, until the end of the first load drop. Since the specimen is loaded after the first load drop, a second delamination occurs when the load reaches to 435 N Figure 4.4.2b, albeit with a lower stiffness. Upon further loading, the stiffness of the specimen slightly decreased and the specimen can still carry load up to 430 N. Then the third and the fourth delaminations occur as shown in Figure 4.4.2c. This failure mechanism has also been explained in section 4.1. The longitudinal stress components are maximum at the inner part of the curved region, which causes small matrix cracks at the 90° oriented plies. Although, the shear and the normal stresses are maximum at different locations, the dominant stress type of this failure mechanism is longitudinal stress because of the 90° fibers. The reinforcement part of a composite material consists of fibers. The primary mission of the matrix part is to hold the fibers together and transmit the loads. Generally, the material properties of the adhesive materials are lower than the reinforcement material and this fact causes weaknesses in the longitudinal direction for this case. In Figure 4.4.3, a general picture of the failed specimen is shown after the failure.

The crack tip positions and speeds were calculated from the first five pictures of the delamination process, with respect to the crack initiation point shown in Figure 4.4.2b. The right and the left crack tip locations was determined as a function of time in (Figure 4.4.4a). Approximately the same amount of propagation through both of the arms was calculated. With the crack initiation point taken as the crack origin, the crack tip speeds are separated as the right and the left crack tip speeds with respect to this origin. The crack tip speeds were calculated with the 3-point backward difference method and are plotted in Figure 4.4.4b.

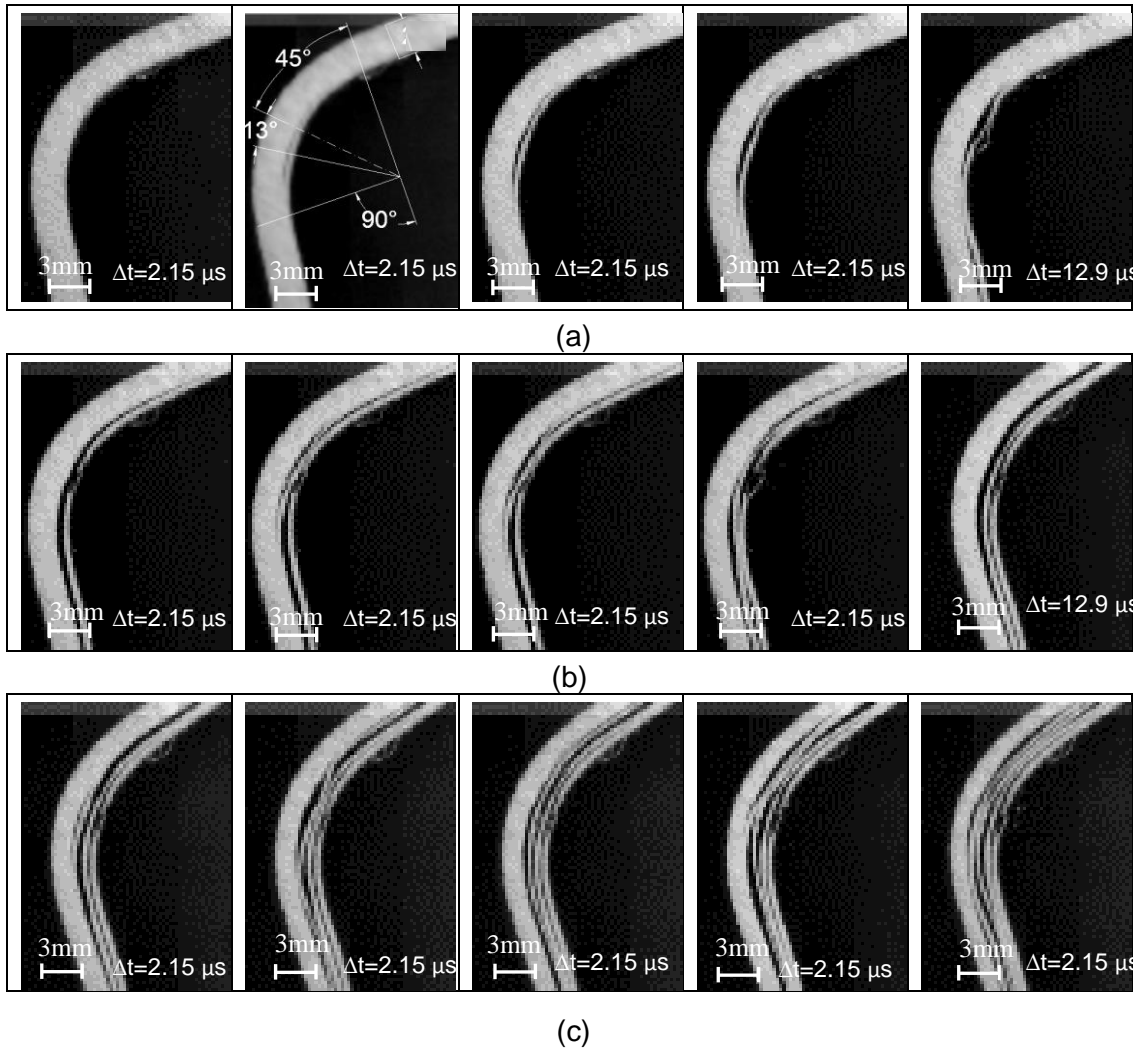


Figure 4.4.2 [90/0] cross-ply progressive damage pictures taken at 465000 fps (a) 1st load drop (b) 2nd load drop (c) 3rd load drop



Figure 4.4.3 Picture of the [90/0] cross-ply specimen taken after the failure.

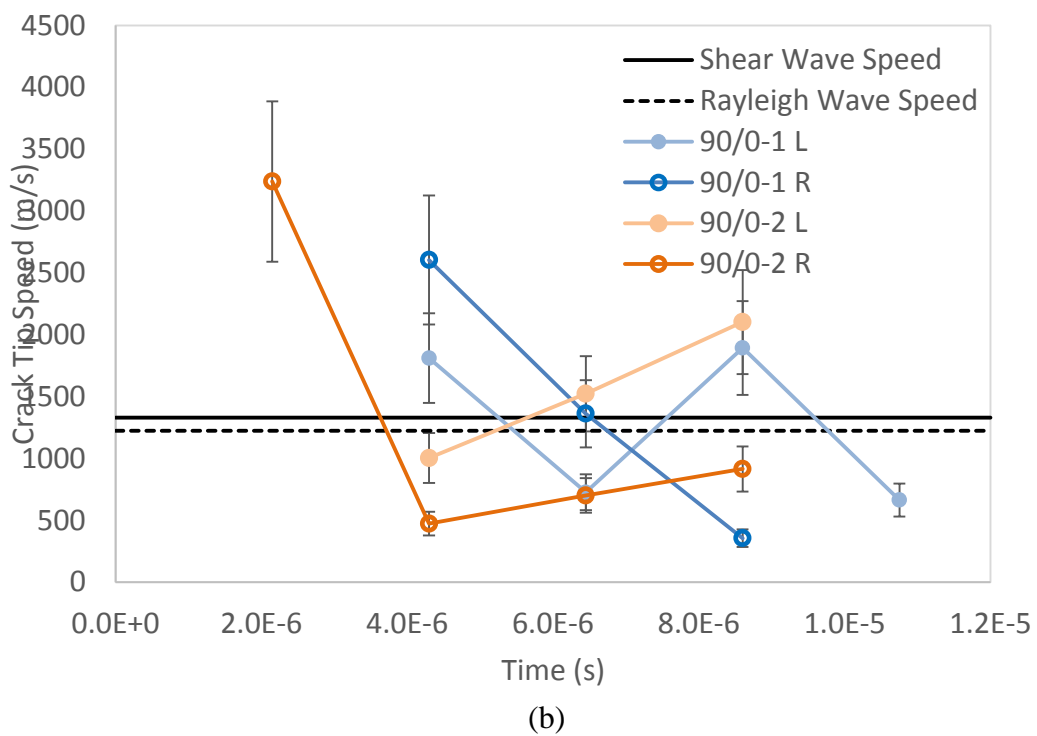
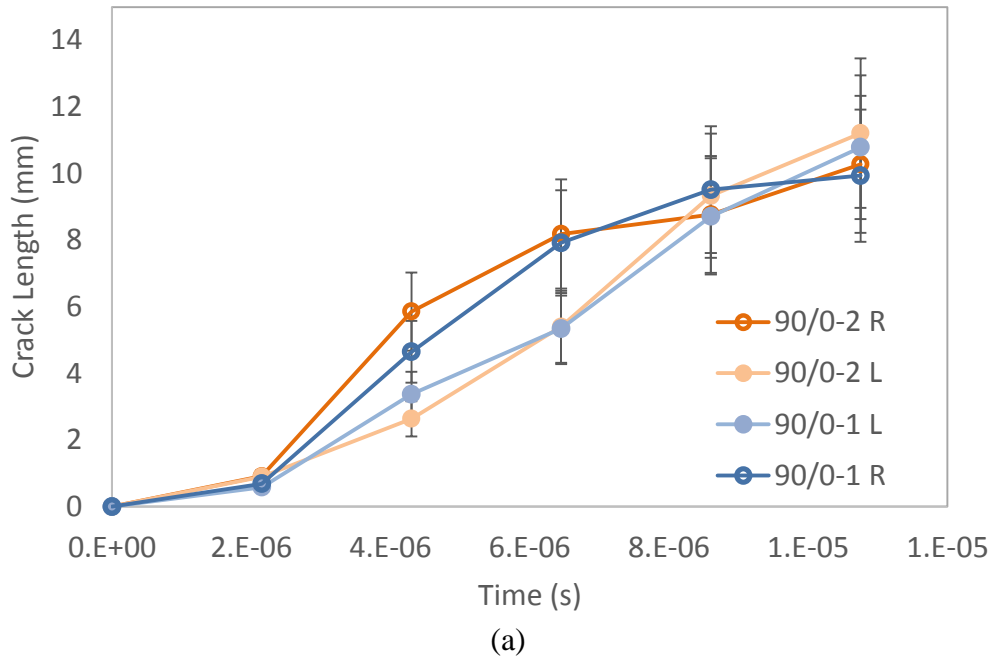


Figure 4.4.4 (a) The right and left crack tip progress during delamination propagation
 (b) Crack tip speed history for initial crack of [90/0] specimen under perpendicular loading.

In Figure 4.4.4b, the crack tip speeds are shown together with the material wave speeds (the shear wave speed (C_s), Rayleigh wave speed (C_R) and dilatational wave speeds parallel and perpendicular to the fiber directions (C_I^{\parallel} , C_I^{\perp})). The first

calculated speeds (391 m/s and 270 m/s) are smaller than the Rayleigh wave speed of the material (1224 m/s). The second point data (2340 m/s and 1810 m/s) exceed the wave speed levels, which prove that the crack nucleation part is shear dominated. Then crack tip speeds reach the intersonic speed of 1330 m/s. The fracture mode near the crack tip is mixed-mode as discussed in [48].

The tested specimen was prepared for a microscopic analysis, following the steps mentioned in the method section. The curved part of the laminate with 4 succeeding cracks was monitored with microscope (Figure 4.4.5). First, the locations of delamination are determined. First delamination is between the 3rd and the 4th plies, which corresponds to the 1st load drop. The second delamination is in the 5th ply, which corresponds to the 2nd load drop. And the following delaminations are located at the 7th and the 9th laminates through the curvature, which corresponds to the 3rd load drop (Figure 4.4.1). The first observation about the failure mechanism is that the failure modes are different at the center part and at the end of the curvature. In the curved part, vertical cracks in the first 90 ply are observed (Figure 4.4.5a,b). The crack lied between the fibers, and in the second 90 ply, vertical and 60 degree cracks are monitored. This fact proves the matrix crack observations. Thus, the cracks meander the 90 ply instead of causing delamination in the curved parts. The area under meandering behavior is getting smaller from the first crack to the last crack. Near the arms, the 90 degree cracks are transformed into the interlaminar delamination failure (Figure 4.4.5c). Thus, the cracks propagating between the 90° fibers changed their attitude to the interlaminar propagation, which propagate through the 0° and 90° interface.

In the section 4.1, the stress fields of the [90/0] cross-ply laminate was shown. In the simulations, the longitudinal stresses were found to be maximum at the inner part of the laminate whereas the shear stresses were maximum at the end of the curved region and opening stresses were maximum at the center part of the curved region. By using this stress field analysis, the failure mechanism of the 90/0 laminate was explained. In micrographs, the following statements are proven;

-At the inner part of the curvature, higher longitudinal stress distribution causes small matrix cracks, in the 90° laminate so the crack starts from this area. The angled

cracks and the meandering view show matrix cracking initiations followed by growth by coalescence of these cracks.

-This meandering behavior is getting smaller, going through the mid part of the thickness. At the mid-part, the dominant stress was found to be the opening stresses. The transferal of the dominant stress types causes the attitude of cracks.

-At the end of the curved region, cracks propagate at the interface between the layers and the crack tip speeds are increasing (Figure 4.2.6). These facts strengthen the observation related to the change of the dominant failure mechanism to shear dominated.

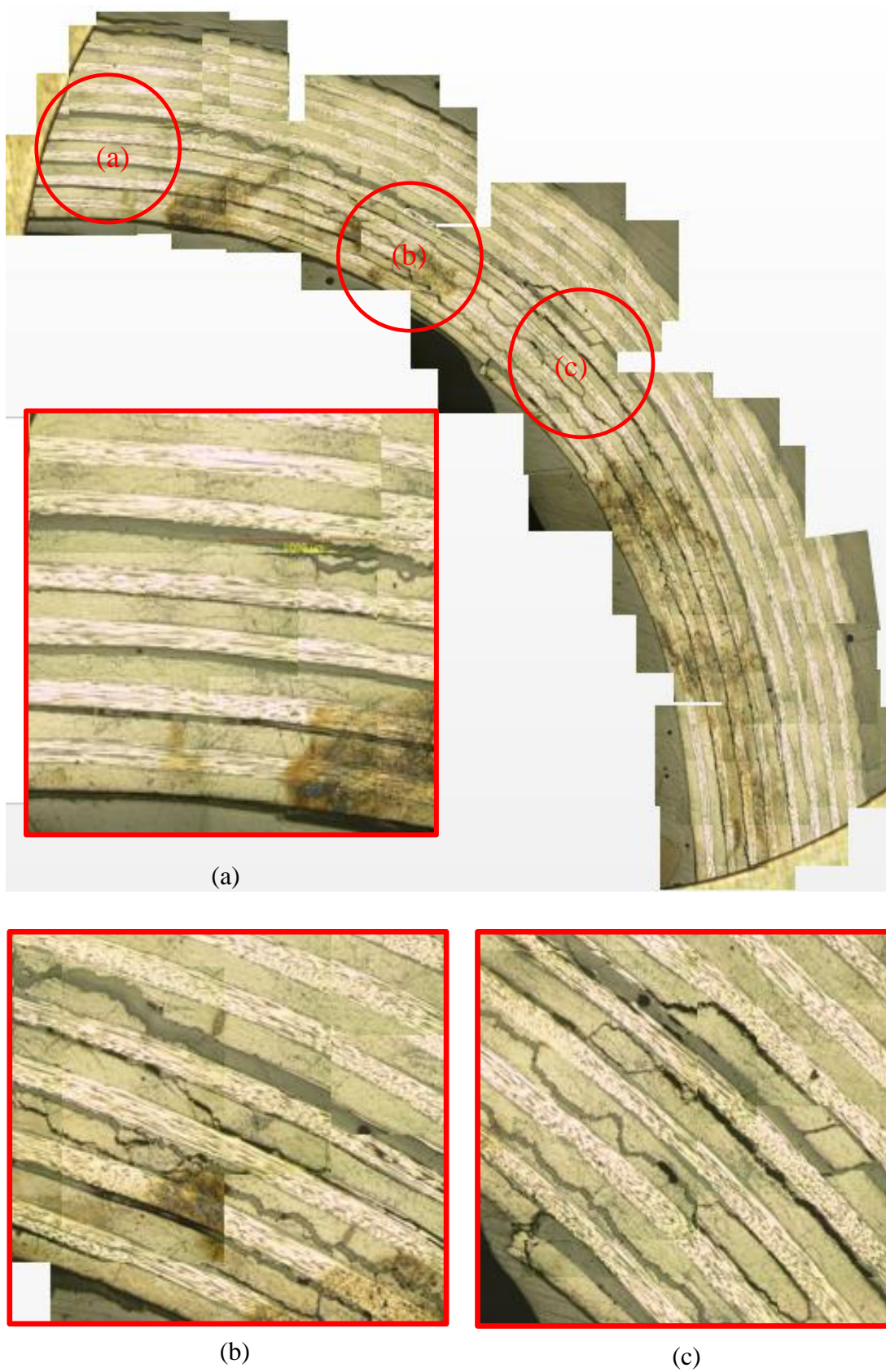


Figure 4.4.5 Micrograph of the curved region of the [90/0] cross-ply laminate

4.4.2. [90/0] Cross-ply Lay-up with 10 mm inner radius and different thicknesses

In the previous section, a single configuration for the [90/0] laminate was selected in order to compare the failure mechanism with other lay-ups. The failure mechanism was found to be different than the other cases. Furthermore, the initial failure mode that causes delamination starting at the inner part of the laminate was found to be matrix cracking. The next issue of doubt about this different failure mechanism concerns its “repetitiveness”. It is considered that the thickness is effective on the repetitiveness of the failure mechanism. So, the effect of thickness is investigated. In Figure 4.4.6 , the test specimens are shown with different ply numbers which are 7, 11, 21 and 25 plies. The results are discussed here and the thickness effect will be discussed in Ch. 5.

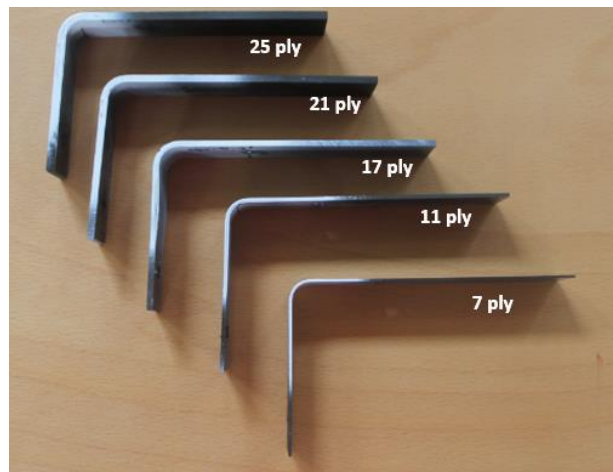
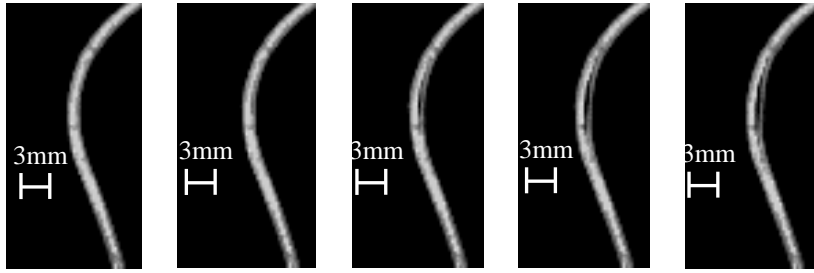
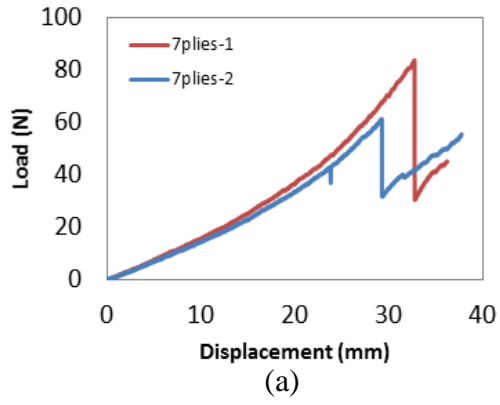


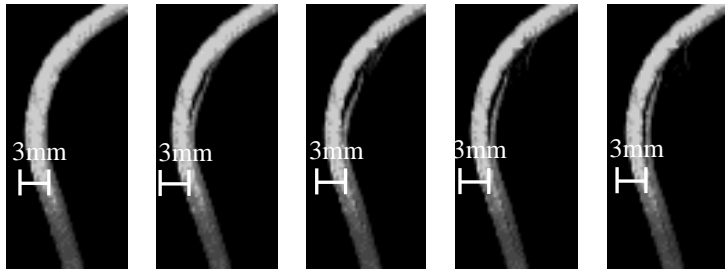
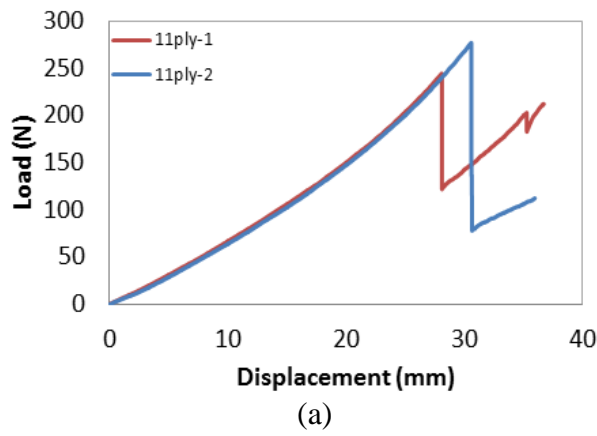
Figure 4.4.6 Specimens with variable thicknesses.

In the Figure 4.4.7, 7-ply specimen's results are shown. The first comment about the experiment is that the specimens lost their L-shape during loading. The angle of the curvature is more than 120° . The flexibility of the specimen causes too much extension before the failure. Also, the load displacement curve manifests softening behavior, which causes non-linearity, during the loading. However, the high speed camera pictures show that the delamination nucleates at the inner part of the curved region, which was observed previously for the 17-ply specimen. Only one crack is obtained before it lost its all geometric constraints.



(b)

Figure 4.4.7 7-ply specimen results (a) Load-displacement curves (b) High speed camera images ($\Delta t=2.38 \mu s$).



(b)

Figure 4.4.8 11-ply specimen results (a) Load-displacement curves (b) High speed images ($\Delta t=2.38 \mu s$).

In 11-ply specimens, the flexibility problem which was seen in the 7-ply specimen become less effective. It does not affect the elastic region of the load-displacement curves. Only one load drop is observed before the geometry lost its curved shape. But in this load drop, a single delamination nucleates from the inner part of the laminate, which shows similarity with the previous cases (Figure 4.4.8).

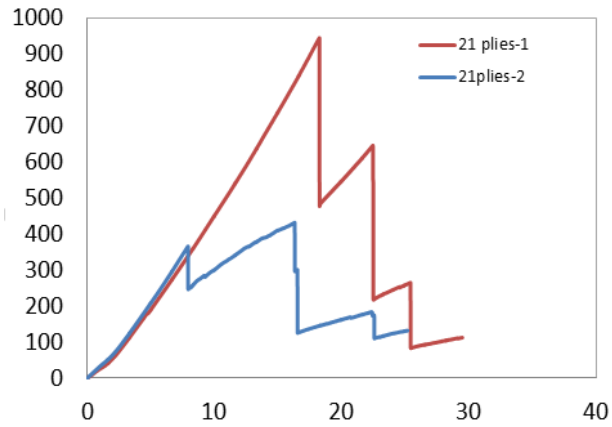


Figure 4.4.9 Load- Displacement curves of the 21-ply specimens.

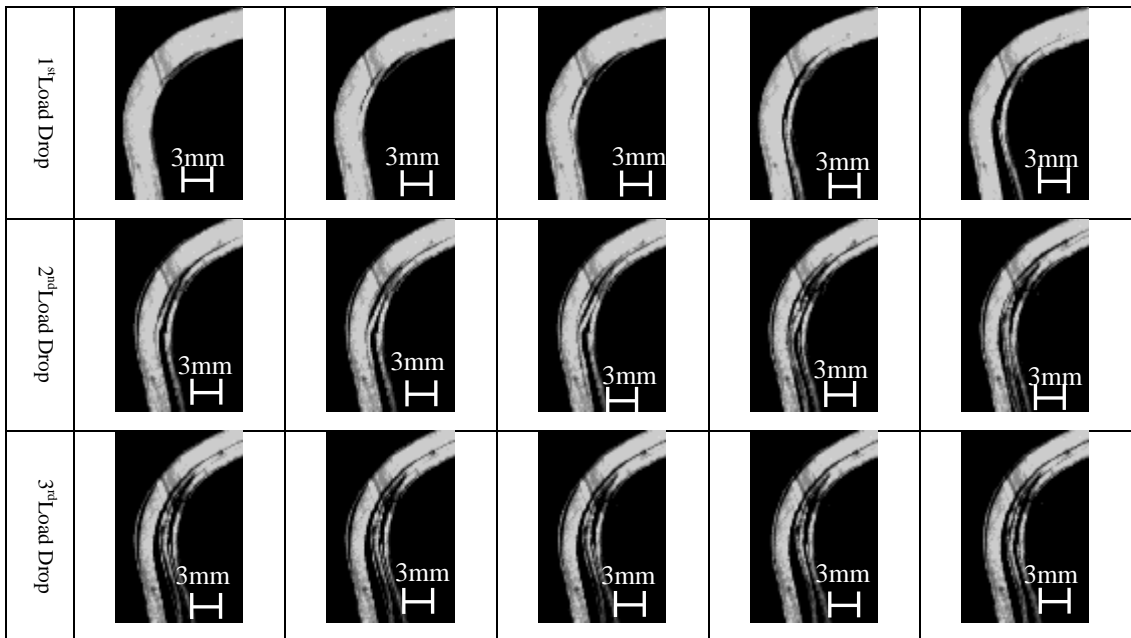


Figure 4.4.10 21-ply specimen results ($\Delta t=2.38 \mu s$).

The third lay-up is the 21-ply specimen. At this point, thicker options than the 17-ply laminates are discussed. In Figure 4.4.9, the 21-ply specimen load displacement curves are seen. The initial observation is related to the maximum load difference of the specimens, which can be due to the manufacturing defects. A small crack is observed before the experiment in specimen 2, which is shown in Figure 4.4.10, first frame. Because of this crack, the laminate fails before the expected load. But the maximum load difference does not affect the stiffness value. Also, the multiple load drop case is seen in the both specimens. The delamination formations corresponding to the load drops for specimen 2 are shown in Figure 4.4.10. In the first load drop, a single delamination nucleates at the inner part of the laminate. In the second load drop, two consecutive delaminations are seen. In the third load drop, a fourth delamination initiates. All delaminations nucleate at the curved region and propagate to the arms. This failure behavior is the same with the 17-ply cross-ply specimen.

In Figure 4.4.11, the load-displacement curves of the 25-ply L-shaped specimens are shown. Although, the same elastic modulus is seen in specimens, there are variations between the maximum loads of the specimens. When the specimens were analyzed before testing, the manufacturing defects and small delinking between the groups of 90° plies were seen. This situation affects the maximum load of the specimen by acting like a pre-crack. Therefore, the first delamination propagates from these initial-cracks at the inner layer of the specimen (Figure 4.4.12). This first delamination corresponds to the first load drop. In the second load drop, a second delamination initiates very close to the first delamination. And at the final load drop, the delamination nucleates very close to the outer part. It is noted that the number of plies affected the manufacturing disabilities in curing. So if the top and the bottom plies are not bonded well, the failure mechanism can also be affected. This can be another reason why the third delamination propagates very close to the other surface.

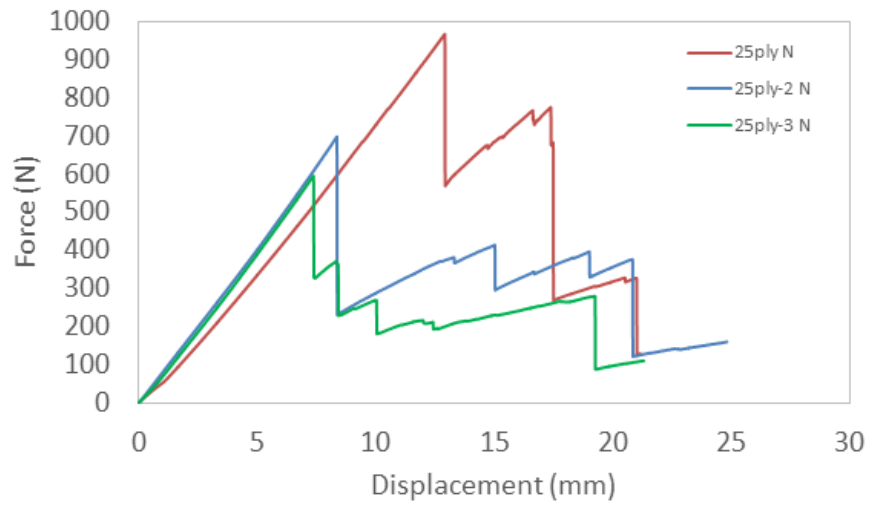


Figure 4.4.11 Load-displacement curves of the 25-ply specimen.

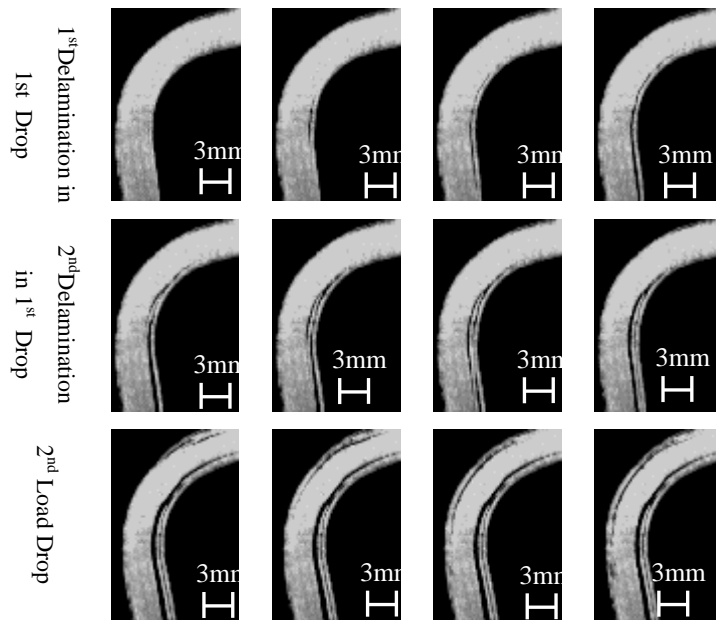
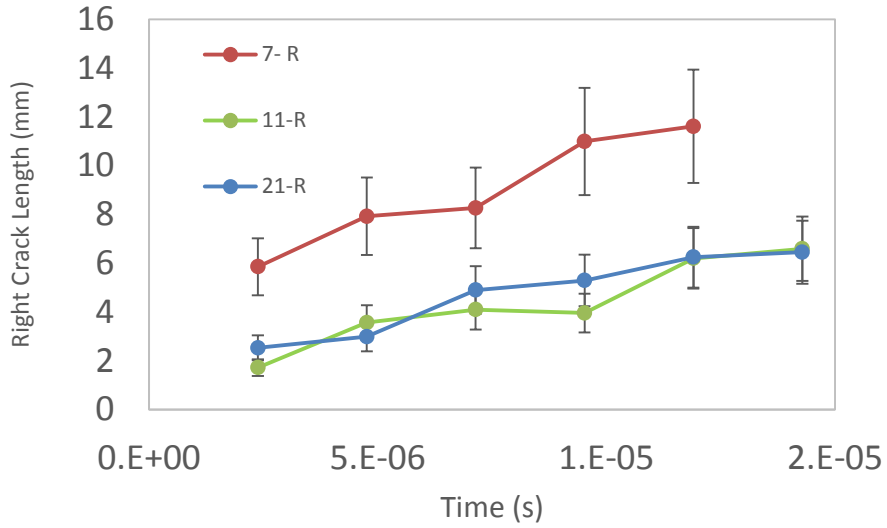
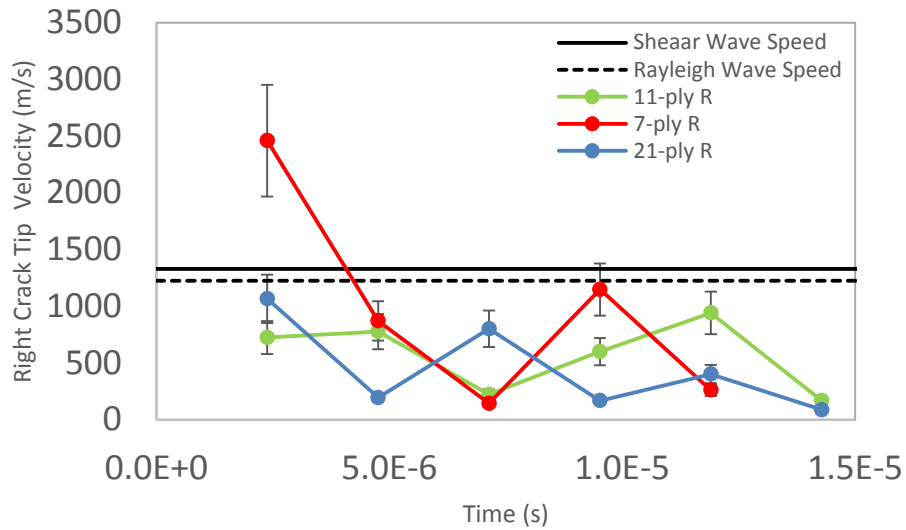


Figure 4.4.12 High speed camera results of the 25-ply specimens ($\Delta t=2.38 \mu s$).

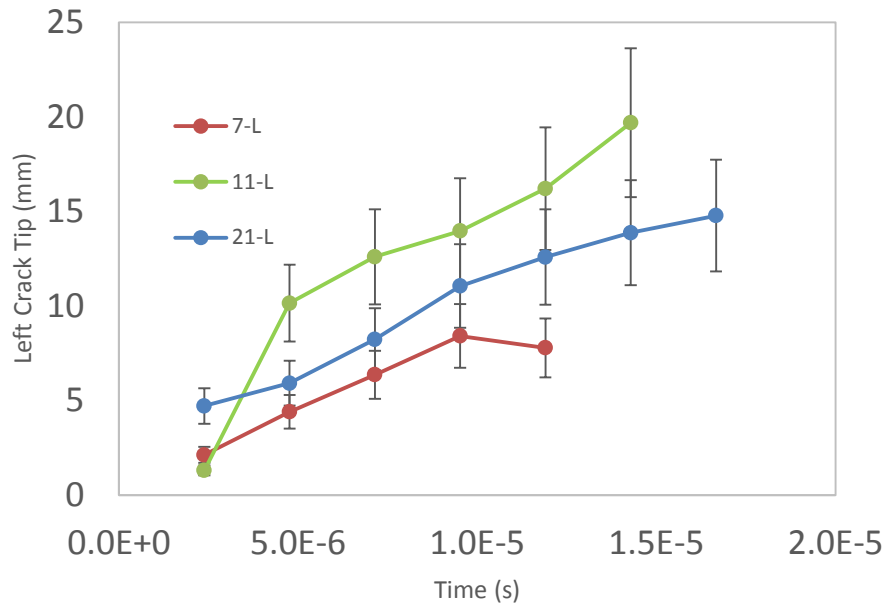


(a)

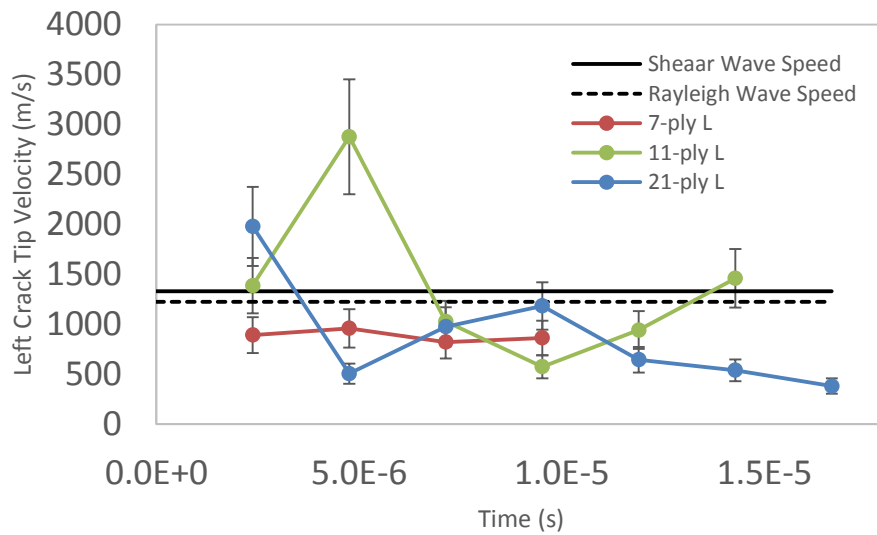


(b)

Figure 4.4.13 (a) Right Crack length vs. time graph with respect to the crack nucleation point for 7, 11 and 21-ply laminates. (b) Right crack tip speed for 7, 11 and 21-ply laminates.



(a)



(b)

Figure 4.4.14 (a) Left Crack length vs. time graph with respect to the crack nucleation point for 7,11 and 21-ply laminates. (b) Left crack tip speed for 7, 11 and 21-ply laminates.

The 5 or 6 pictures taken with the high speed camera after the crack became visible were used to calculate the crack lengths. In the first picture, the crack nucleation point was marked and the crack axes were placed at this origin. In the following images, the crack length was calculated with respect to this point. The crack, which lied through the right (upper) arm of the laminate, was referred to as the right crack tip and the same conversion was also used for the left (lower) arm of the laminate.

Same procedure was repeated for the 7, 11 and 21-ply specimens. The results are shown in Figure 4.4.13a and Figure 4.4.14a. When the two graphs are compared, it is seen that the left crack lengths are higher than the right crack lengths. In the right crack tip, the longest crack lengths are measured for the 7-ply laminate. On the other hand, in the left crack tip, the 11-ply specimen has the higher crack length value. For both crack tips, the crack tip speeds are calculated by using backward difference method. The right crack tip velocity of the 7-ply specimen has a higher value for right crack tip velocity (2460 m/s). On the other hand, the highest value for the left crack tip belongs to 11-ply specimen (2876 m/s). The slope of left crack tips is generally higher than the right crack tips. The 21-ply specimen velocities are smaller than the 7-ply and 11-ply laminate. The crack length data were not measured for the 25-ply case. If the high speed pictures are investigated, it is seen that the crack initiates from a pre-crack. So, the real crack length was not determined reliably. During the crack length measuring part, the crack initiation locations were found in the first place. The angular position of the crack formation points was also calculated. In Figure 4.4.15, the angular position of the crack nucleation points for the 11-ply and the 21-ply specimens are shown. In the 11-ply specimen, the crack nucleates 11° left of the center of the curvature and in the 21-ply specimen, the crack nucleates 9° right of the center. For the 7-ply case, the angular position was not calculated. Although the nucleation point was easily seen, the specimen lost its curved shape before the failure (Figure 4.4.7).

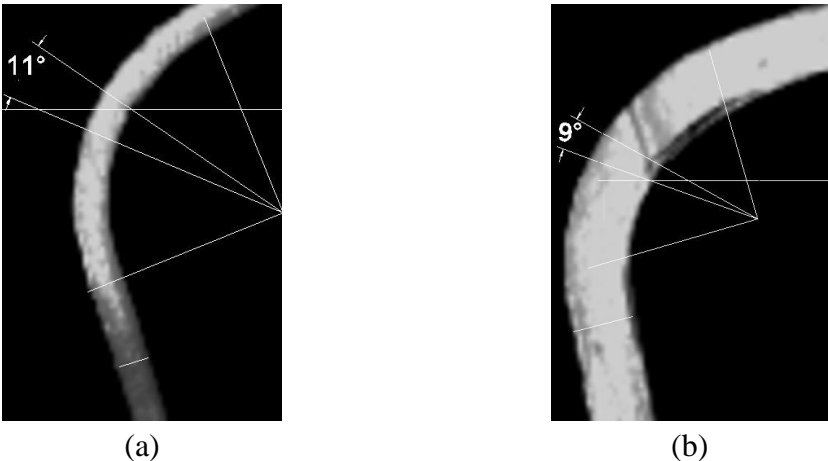


Figure 4.4.15 The crack initiation locations for (a) 11-ply specimen (b) 21-ply specimen.

4.4.3. [90/0] Cross-ply Specimen with 17 Plies and variable inner radii

In the [90/0] cross-ply laminate, the failure mechanism has been discussed for different ply numbers (i.e. thickness) of L-shaped geometry. Next, the radius of the curved part is changed and the effect of the inner radius on the failure mechanism will now be discussed. In order to monitor this effect, all the geometrical constraints except the inner radius were kept constant and 5 mm inner radius test batch were prepared. Three different tests were conducted under the shear loading and monitored with the high speed camera. The load displacement curves are shown in Figure 4.4.16. There was 200N difference between the maximum load values. But the stiffness values were in good agreement. A reason for this difference can be the initial cracks or voids in the structure due to the manufacturing disabilities. The variation between the maximum loads is investigated in future work in detail.

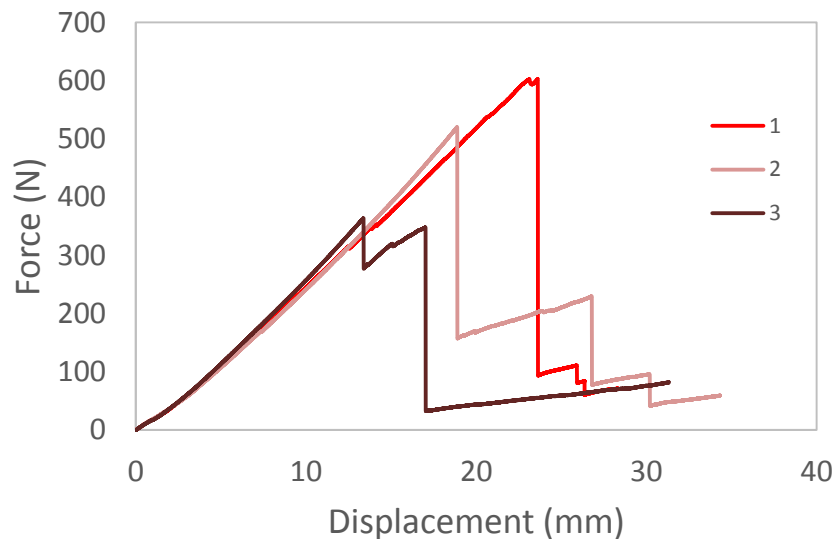


Figure 4.4.16 Load-displacement curves of 5mm inner radius experiments.

As it was discussed in the previous sections, cross-ply specimen curves have multiple load drops. The same tendency is seen in the 5 mm inner radius specimens. But, it is observed that the stiffness change is considerably high compared with the previous cases. The load decrease to 10-15 % of the maximum load. After the crack propagation, the smaller inner radius increases the sharpness of the specimen and increases the stress concentration in the curved area.

The high speed camera pictures show the delamination mechanisms. The experiment pictures of the experiment 2 are used for this purpose. In the first load drop, the load decreases from 500N to 150N and two delaminations nucleated and propagated successively. As it is seen in Figure 4.4.17, the first two cracks are formed at the inner part of the curved region. The specimen with two cracks cannot carry much load. The second maximum load is less than 220N. The stress concentration of the curved region is supposed to be higher than the 10 mm inner radius specimens. So, the damage tolerance of the specimen decreases with decreasing inner radius [54]. In the second load drop, a third delamination is nucleated very close to the first two delaminations. Although the cracked part is small compared with the whole thickness, the specimen lost its stiffness after this point. In the third load drop, the 4th and the 5th delaminations are seen.

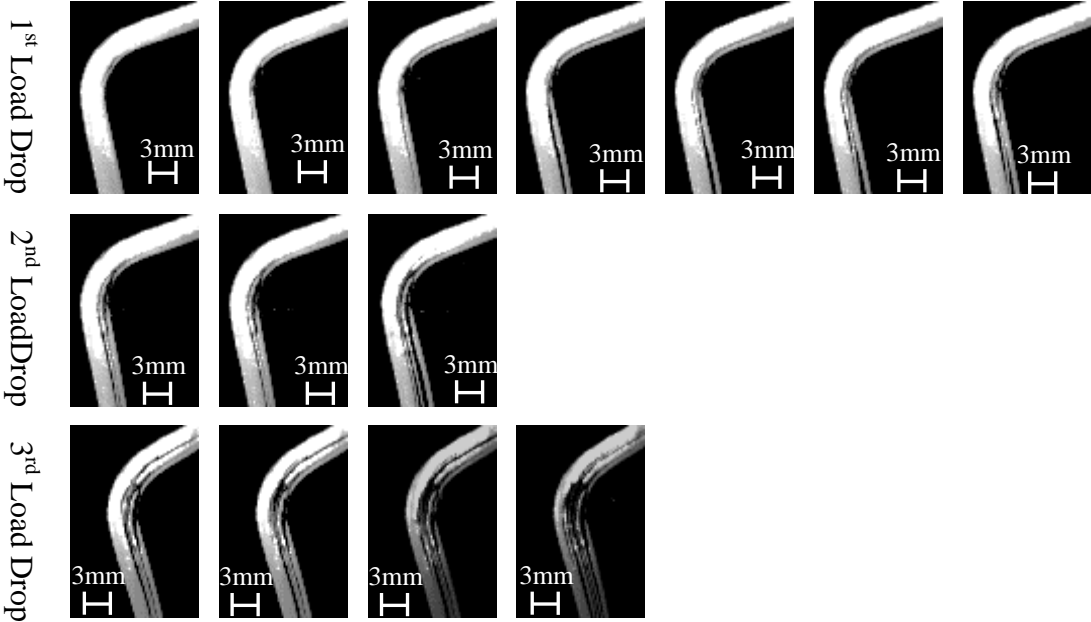


Figure 4.4.17 High speed camera pictures for specimen 2 ($\Delta t=2.38 \mu s$).

From the high speed images, the crack nucleation point was determined first, which is 18° left of the center of the curvature (Figure 4.4.18). By considering this point as the origin, the left and the right crack lengths are measured. In Figure 4.4.19a, the crack length data with respect to time are shown. The growth rate of the cracks is not the same. The left crack size is higher than the right crack size. Furthermore, the crack tip speeds are calculated by using backward difference method. The left and right crack tip speeds with respect to time are shown in Figure 4.4.19b. The

maximum value for left crack tip is calculated as 1716 m/s and the maximum value for right crack tip velocity is calculated as 881 m/s.

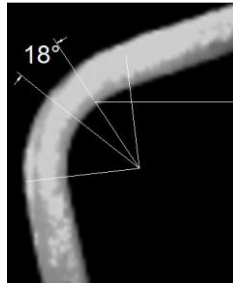


Figure 4.4.18 The angular position of the first delamination with respect to the center of the curvature.

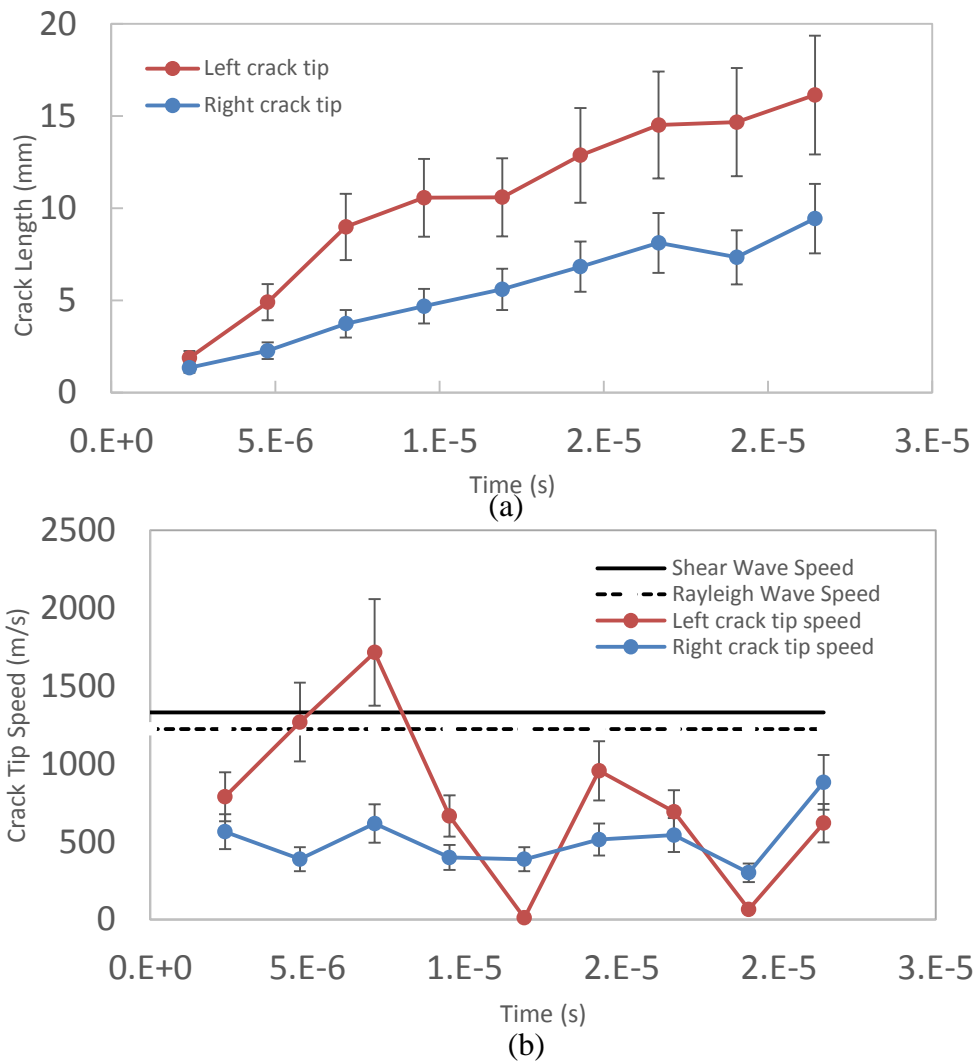


Figure 4.4.19 (a) Right and Left crack length vs. time (b) Right and left crack tip speeds vs. time for 5mm inner radius specimen-2.

CHAPTER 5

DISCUSSION

In this part, the results of quasi-static shear loading experiments conducting with [0/90] fabric, [0] UD and [90/0] cross-ply specimens that presented previous chapter are compared each other under four headings. In Sec 5.1, [0/90] fabric and [90/0] cross-ply experiment results are compare to discuss two different pre-peg types of same CFRP with same orientation in terms of microstructure, load-displacement curves and the failure mechanisms. On the other hand, the lay-up difference of same type of CFRP pre-peg is discussed in Sec. 5.2. For this purpose, the load displacement curves and failure mechanisms of the [0] and [90/0] oriented laminates are compared. In Sec 5.3, the thickness effect on failure mechanism of cross-ply composite laminate is discussed. In addition to the baseline ply number of 17, 7, 11, 21 and 25 ply specimen results are compared. In Sec 5.4, the effect of inner radius on failure mechanism of cross-ply L-shaped laminate is discussed by comparing 5 mm and 10 mm inner radius specimens of 17-ply baseline.

5.1. Effect of the Material

In aircraft industry, different types of carbon fiber pre-pregs are used in the reinforcement of the composite laminates. The two main types of pre-pregs are the unidirectional and the woven fabricated pre-pregs. In unidirectional (UD) pre-pregs, the majority of fibers run in one direction only. The angle represents the fiber direction. In woven pre-pregs, a group of fibers are combined to get an even reinforcement. The woven fabrics are produced by the interlacing of warp (0°) fibers and weft (90°) fibers in a regular pattern or weave style [55]. In this part, differences in the failure mechanism caused by using UD pre-pregs or weave pre-pregs are discussed.

For this purpose, the L-shaped structures are manufactured with the [0/90] UD pre-pregs and the [0/90] 5HS weave pre-pregs. To get the same laminate thickness, the

specimens are manufactured with different number of plies. The [0/90] UD laminate has 17 plies and [90/0] laminate has 12 plies. In Figure 5.1.1, the texture differences of the UD and weave fabrics are seen from the thickness perspective in micrographs.

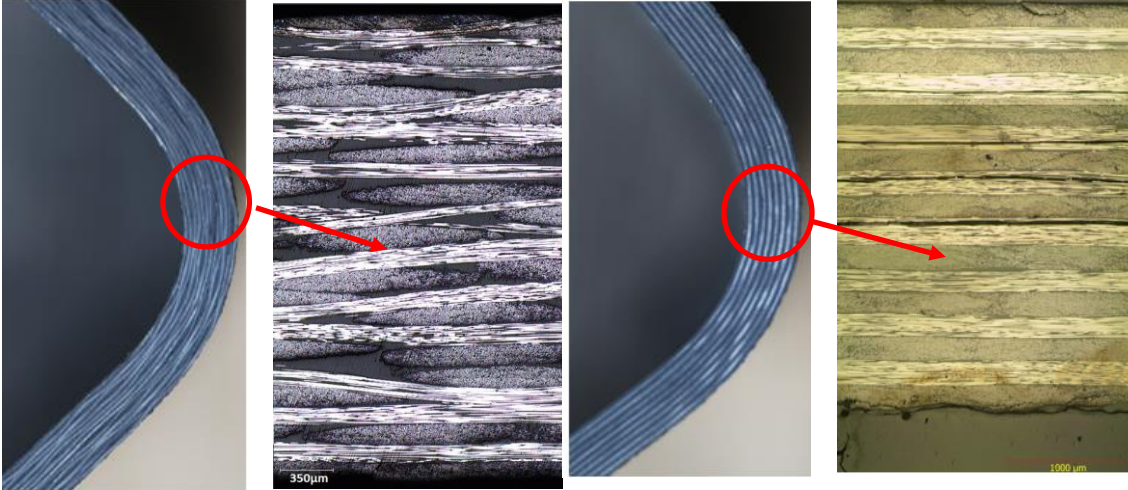


Figure 5.1.1 The texture difference between the Fabric and UD laminate for 90/0 orientation

The first comparison is related to the load-displacement curves as shown in Figure 5.1.2. The woven fabric (orange colored) resists higher loads than UD laminates (blue colored). In fabrics, a single load drop occurs which, corresponds to delamination. On the other hand, the UD 90/0 laminates have multiple load drops. Another significant difference between the curves concerns the load carrying capacity after the failure. In the woven case, the specimens do not resist to loading. But in the UD 90/0 case, the cracked specimens can carry load up to %75 percent of the maximum loading. The damage tolerance of the UD laminates is higher than the woven laminates.

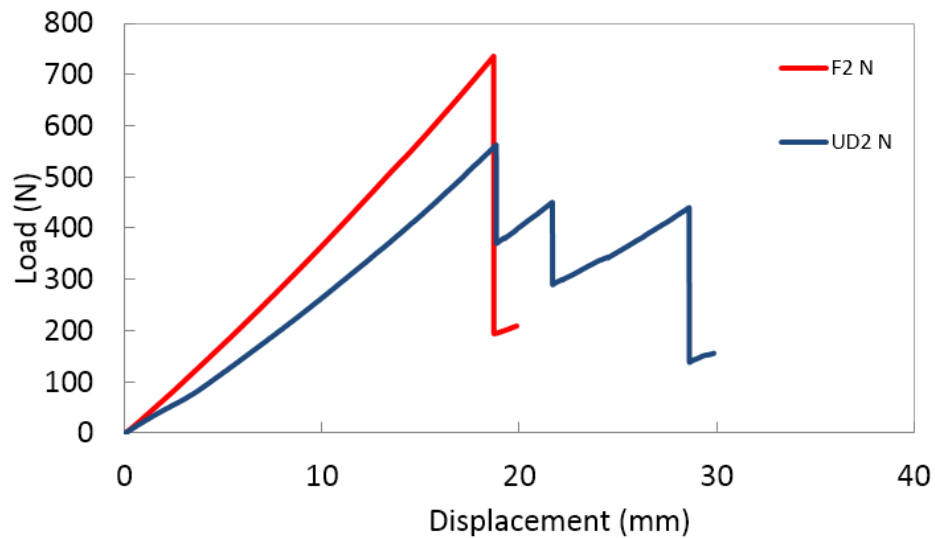


Figure 5.1.2 The load-displacement curves of the fabric and UD specimens.

The high speed pictures of the specimens are shown in Figure 5.1.3 and Figure 5.1.4. In the woven fabric laminate, only one delamination nucleation is observed. As it has been shown in the previous section, the delamination propagates between the 5th and the 6th plies. When the fracture surface is investigated with the microscope, it is seen that the crack follows the 5HS weave structure. Because of that, the crack is not seen as a clear interface in the high speed camera pictures. Although it is observed as a single crack, the crack appears to be branched and multiple cracks are seen in the micrographs. The weave pattern prompts to the fiber bridging during the crack propagation (Figure 5.1.3).



Figure 5.1.3 The high speed images of the Fabric [0/90] laminate with the micrograph of the curved region.

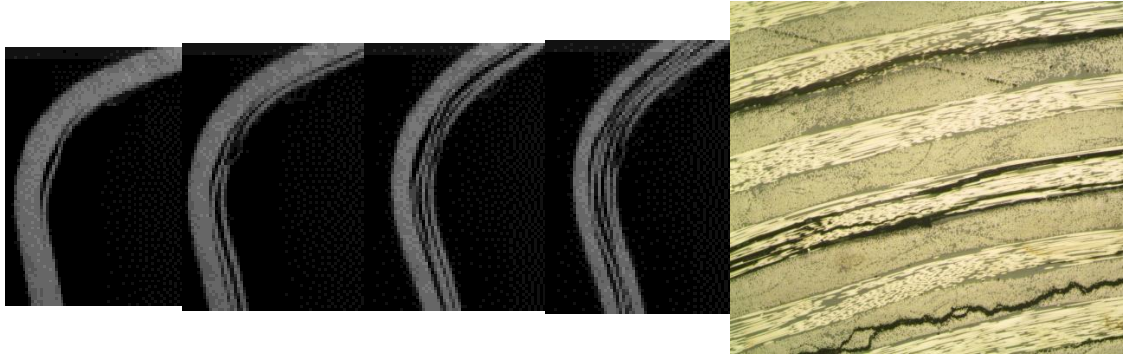


Figure 5.1.4 The high speed images of the UD [0/90] laminate with the micrograph of the curved region.

In the UD 0/90 laminate, the high speed camera pictures show sequential delamination growth. The detailed explanation for the failure mechanism has been given in section 4.4. But, as a reminder, the crack growth starts at the inner part of the curved region, at the 3rd interface. The cracked specimen keeps carrying the load and a second delamination initiates at the 5th interface. The subsequent delaminations propagate in the 3rd load drop, at the 7th and the 9th interface (Figure 5.1.4). The stiffness of the specimen decreases after each load drop but the specimen still carries load as far as its capacity. After the experiment, the failure surface was investigated with the microscope. The locations of the delaminations were obtained by this way (Figure 5.1.4). Also the crack types are classified. An example of the micrographs is shown in Figure 5.1.4. Three types of cracks are monitored. The first one shows the delamination while propagating, induced with the matrix cracking in the 90° ply. The second delamination propagates in the 0° layers and the final delamination goes straight between the 90° and 0° layers, which is called the interlaminar. From these observations, it is concluded that the weave of the fiber bundles can change the delamination mechanism, even though the loading, boundary conditions, dimensions, orientation and the material are kept intact. The weave fabric texture prevents the complex failure types when it is compared with the UD material. But the UD material can be more damage tolerant in the 90/0 orientation.

5.2. Effect of the Lay-Up

In order to discuss the orientation differences and the effect on failure mechanism of composite specimen under shear loading. The results of the [0] UD laminate and the [90/0] cross-ply laminate are discussed in this section. According to the results, a dynamic delamination process has been observed for the both cases. This condition proves that the lay-up differences do not affect the dynamic failure of the composites but they affect the load carrying capacity. In Figure 5.2.1, the [0]₁₇ laminates can carry up to 850 N, while the maximum load of the [90/0] cross-ply laminate is 500 N. The difference between the maximum loads can be explained with the difference between the longitudinal modulus of the composite laminate which makes the laminate stronger in the longitudinal direction (Table 3.3.2). Therefore, the [0] laminate is stronger than the [90/0] along the loading direction until the initiation of delamination. After the delamination process, the load carrying capacity of the laminates is different, either. In the [0] laminate, there is a single load drop where the structure loses most of its load carrying capacity. In the [90/0] laminate, three small load drops are seen until the loss of all load carrying capacity. After the load drop in the [0], the load carrying capacity reduces to one tenth of its initial value whereas in the [90/0] plies small decreases are observed after each load drop. The results show that the delamination process is different between the two plies. Multiple delaminations in one load drop are observed in the failure of unidirectional laminate whereas sequential delamination at each discrete load drop is seen in the cross ply laminates (Figure 4.3.2 and Figure 4.4.2).

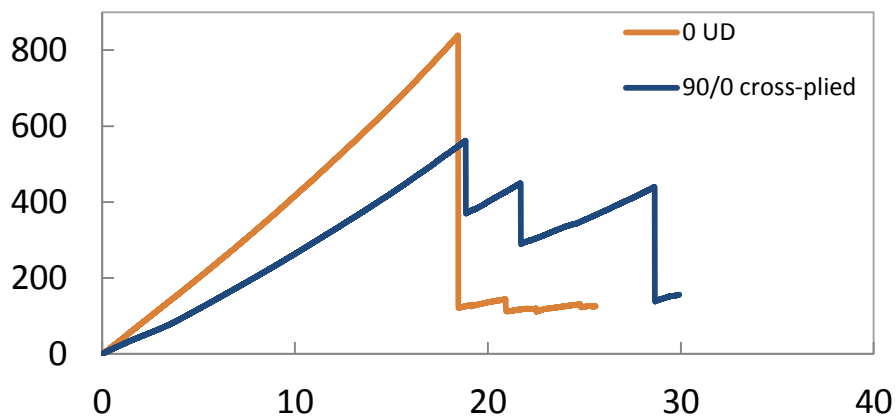


Figure 5.2.1 Load-displacement curves of [0] and [90/0] specimens.

In the $[0]_{17}$ plies, crack initiates near the center ply, followed by two cracks nucleated symmetrically around each of the tips of the original crack (Figure 5.2.2). In the $[90/0]$ laminate, the first delamination occurred between the third and the fourth plies from the inner radius. After the growth of the first delamination, other delaminations initiated from the inner radius to the outer radius successively (Figure 5.2.3). This difference supports the idea that the competing mechanism of different stresses at the curved region is affected by the ply orientation. As it was discussed in 0, the maximum opening stresses are located at the mid part of the curved region. The 0° layers are weak in that direction. The secondary cracks are nucleated symmetrical to the first crack at the end of the curved region. These four nucleation points are placed in the maximum shear stress region. On the other hand, the axial stresses are found to be maximum at the inner part of the laminate, where the cross-ply laminates started to fail. The 90° plies are weak against the the axial stress. Small matrix cracks are formed at the location of the high axial stress. These matrix cracks (seen in Figure 4.4.5b) weaken the lamina in the angular direction and the delaminations nucleate at these points (Figure 5.2.3). But the crack characteristics are different at the center part and at end of the curved region, which can be explained by the different maximum stress regions (section 4.4).

It is concluded that, the $[90/0]$ lay-up is more damage tolerant under the shear loading condition. Despite the crack formation, it can still carry loads without changing its stiffness value and this gives flexibility to designers in the structural design process.

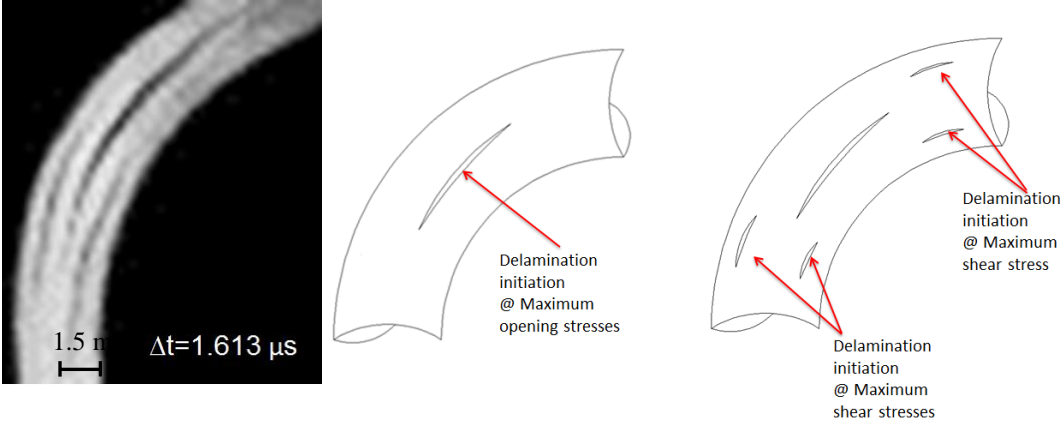


Figure 5.2.2 Failure mechanism of $[0]$ UD laminate.

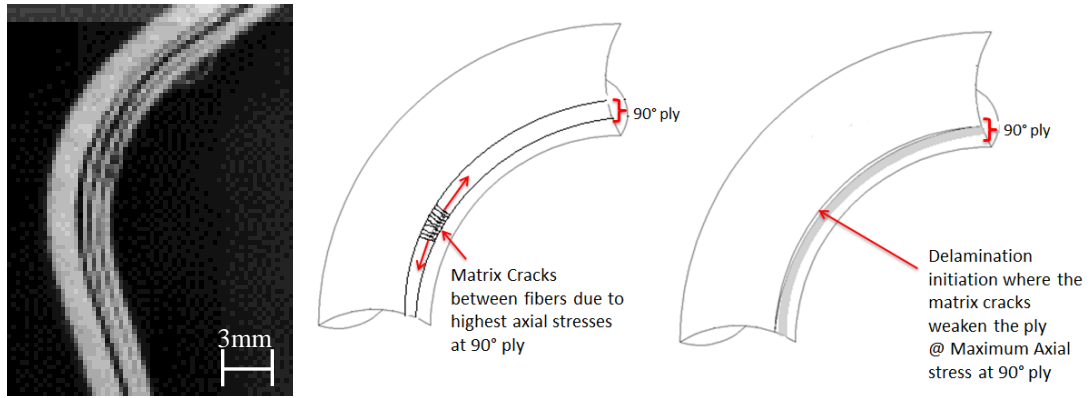


Figure 5.2.3 Failure mechanism of [90/0] cross-piled laminate.

5.3. Effect of Thickness

In previous section, the effect of ply orientation in same thickness has been discussed. In cross-ply case, a different failure mechanism has been determined. At this point, the next question is whether same failure mechanism is seen in specimens with different thicknesses or it is unique for the one combination of plies. For this purpose, [0/90] cross-ply laminates were manufactured as 7, 11, 21 and 25 plies with same manufacturing technique. The other dimensions were kept same with the original specimens. The results compared with the 17-ply [90/0] laminate.

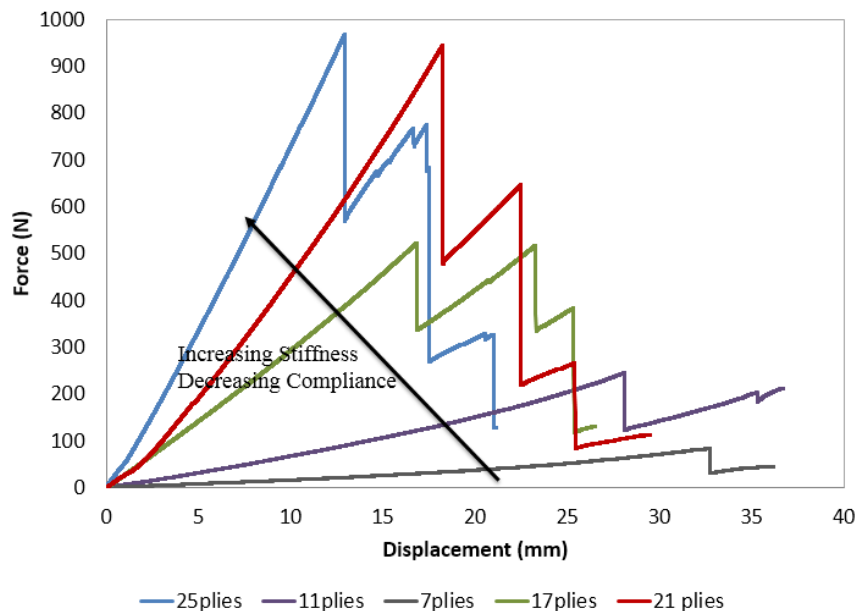


Figure 5.3.1 Load displacement curve of specimens with variable thickness

The first comparison is related to load displacement curves. One load-displacement for each group was chosen and the load-displacement data were drawn together (Figure 5.3.1). Increasing thickness increases the maximum load of the specimen. However, thickness does not affect the maximum load after a point. The maximum load values of 21 and 25-ply specimens are very close to each other. Therefore, thicker laminates are getting stiffer which limit the flexibility of the part. Although, the maximum load values of 21 and 25-ply specimens are very close, the displacement values at the same load decrease 30%. On the other hand, the flexibility is a problem in thin laminates. The maximum load of 7-ply specimen decreases up to 16% of the maximum load 17-ply specimen while the displacement value of 7-ply specimen corresponding to maximum load is two times bigger than 17-ply case. Similarly, 11-ply specimen has 25 mm displacement in z-direction before the first load drop whereas 17-ply specimen has 17 mm displacement. One of the important outcomes for 17-ply cross-ply experiments is multiple load drop characteristic. The multiple load drops in load-displacement are seen in 25, 21-ply specimens. After reloading, it is seen that the maximum load after the crack reaches 75 % of the undamaged specimen's original load carrying capacity. So, the first generalization for the cross-ply laminates can be the load carrying capacity of the specimens remains unchanged after the crack formation. In 7 and 11-ply specimens, one load drop occurs. The flexibility of the specimens is affected the load carrying capacity. Up to first load drop, the specimens are very close to lose their curved shapes. After the first delamination growth, the stiffness values of these specimens are getting lower and they do not resist the loading.

The load-displacement curves of experiments are normalized in accordance with stress terms. The load is divided by t^2 for determining the bending stress in a beam and the displacement is divided by the tangent of the angle between lateral and longitudinal displacement of the curved beam (Figure 5.3.2). Therefore, the effect of thickness is eliminated. The normalized stiffness of the specimens with variable thickness and maximum stress values are found as same. But, the failure behavior of the specimens after the first load drop do not look familiar (Figure 5.3.3).

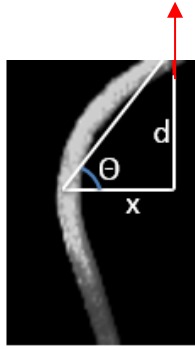


Figure 5.3.2 The angle between lateral and longitudinal displacement with respect to load application.

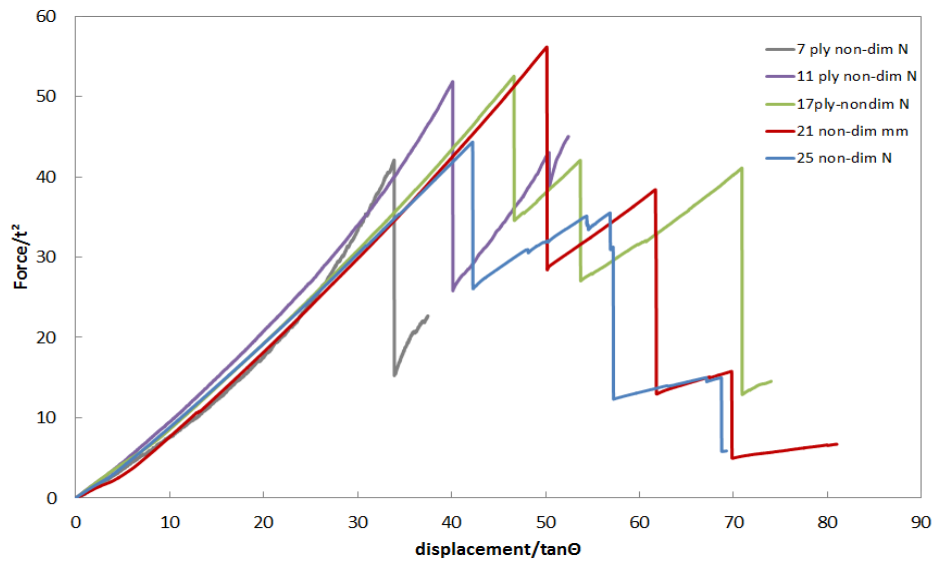


Figure 5.3.3 Normalized load displacement curve of specimens with variable thickness.

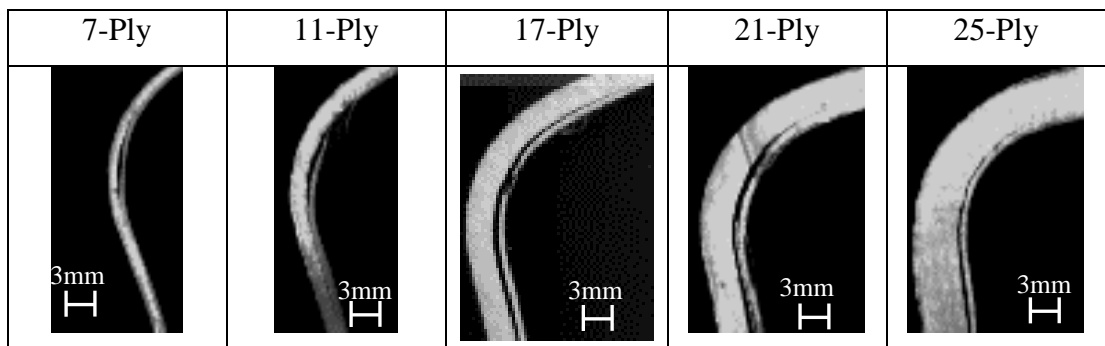


Figure 5.3.4 Comparison of initial delamination failure high speed pictures of [90/0] cross-ply specimens.

The high speed images of laminates have been shown in section 4.4.2 in detail. For comparison, one of the images for each laminate corresponding to initial load drop are chosen. In Figure 5.3.4, it is seen that the first delaminations nucleate at the inner part of the curved region. As discussed previous sections, the high longitudinal stresses at the inner part of the laminate cause matrix cracks in 90° layer that initiate the first delamination in the inner part of the laminate. It is concluded that, the failure mechanism of $[90/0]$ cross-ply specimens under shear loading do not depend on the ply number of the laminate either the load drops are multiple or single.

5.4. Effect of Inner Radius

In L-shaped composite laminates, the curved part is found critical under shear loading. In the experimental work, the inner radius of the specimens is considered as a variable and two different configurations have been prepared for experiments which have been chosen 17-ply laminate with 5mm and 10 mm inner radii.

In Figure 5.4.1, the load-displacement curve comparison for 5 mm and 10 mm specimens are shown. It is seen that the slope of the load-displacement curves do not depend on the inner radius. If this result compares with section 5.3, it is observed that the effect of the thickness is greater than of inner radius on the stiffness of the laminate. The multiple sudden load drops during failure are also seen in 5 mm inner radius case. The only big difference between these two cases is load carrying capacity after failure. In $[90/0]$ cross-ply laminate with 10mm inner radius, the failed composite specimens were reloaded and they continued carrying applied load with a slightly lower stiffness. But in this case, it is observed that the stiffness change is considerably high compared with the previous cases. The load decrease to 10-15 % of the maximum load. After the crack propagation, the smaller inner radius increases the sharpness of the specimen and increases stress concentration in the curved area. Therefore, the load carrying capacity decreases.

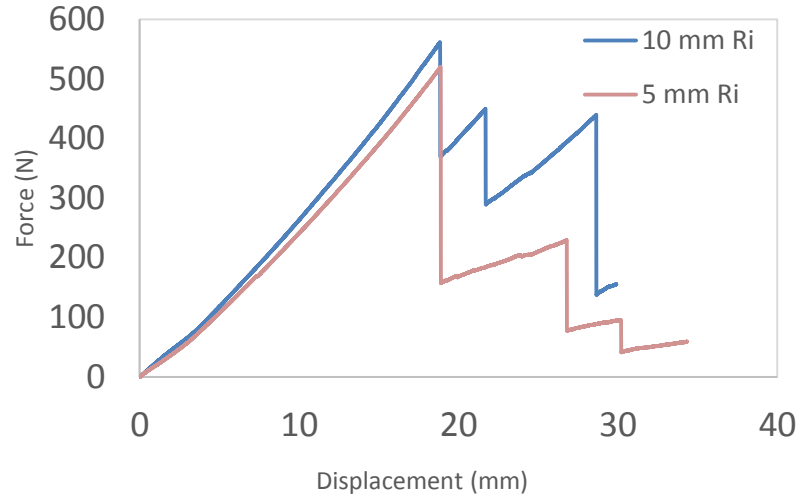
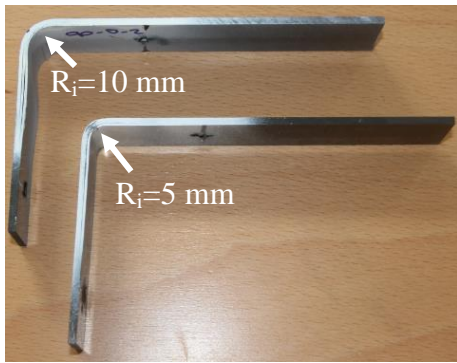


Figure 5.4.1 Comparison of load-displacement curves for 5mm and 10 mm inner radii.

In Figure 5.4.2a, specimens with different inner radius are compared after testing. In Figure 5.4.2b, the high speed pictures after first delamination growth are compared. The high speed pictures corresponding to each sudden load drop have been shown in section 4.4.3. In this part, only one picture is selected for each case to show the first delamination propagation regions. In both cases, the initial delamination nucleates at the inner part of the laminate. The cracked surface thicknesses are small compared with uncracked thicknesses. It is thought that this difference provides the slight change in stiffness. This argument is reliable for 10 mm inner radius specimens. However, in 5mm inner radius case, the high stress concentration in curved region is dominant on stiffness change. The load carrying capacity decreases after the first load drop even though the initial delamination nucleates at the inner part of the curved region (Figure 5.4.2b).

In summary, the failure mechanism for cross-ply laminate with different inner radii is found to remain similar. The slope of the load-displacement curve is not affected by the inner radius. However, the load carrying capacity after the delamination formation decreases because of higher stress concentration at the curved region.

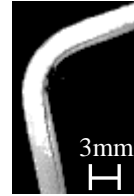


(a)

10 mm inner radius specimen



5 mm inner radius specimen



(b)

Figure 5.4.2 (a) 5-mm inner radius and 10-mm inner radius specimens after testing
(b) Snapshot of first delaminations during first load drop.

CHAPTER 6

SUMMARY AND CONCLUSIONS

6.1. Summary

In this thesis, the dynamic delamination mechanism of the L-shaped composite (CFRP) laminates under the quasi-static shear loading is investigated experimentally. In the first chapter, composite material usage in the aircraft industry, specific to the L-shaped geometry, is discussed. After a brief definition of composite materials, the material selection for this project is explained. The structures consisting of the composite materials are shown and the examples of the L-shaped parts in sub-structures are given. The external loads on the L-shaped parts are defined where the box structures in a wing are taken as reference. When the external loads on a wing structure are investigated, the loading in a typical L-shaped beam can be reduced to three simple loading cases namely, axial loading which is parallel to the arm (P), shear loading which is perpendicular to the arm (V), and moment loading (M). These loads cause delamination in the curved region of the L-shaped composites because of the low through-the-thickness strengths of the composites. Therefore, delamination in the L-shaped composite parts is a critical problem in the aerospace industry.

In order to focus on this problem, a literature review is conducted and the past studies related to the curved composite failure mechanism are summarized in the second chapter. To the best of author's knowledge, the pioneering studies about the delamination problem were started in the late 80s. Thus, delamination in the L-shaped beams can be considered as a new subject in the fracture mechanics community. When the studies are investigated, it is seen that the concentrated loading mechanism is the shear loading which is perpendicular to the arm. Also, the studies generally focus on the delamination initiation and report that the delamination

mechanism is unstable. But, the experimental procedures are limited. Since, the failure occurs unstably, the monitoring of the mechanism became a problem. In the studies, the pictures taken after the failure are reported. So, the experimental data are weak to explain the delamination initiation and propagation mechanism. To stay consistent with the studies in the literature, the loading case is chosen as the shear loading which is applied perpendicular to the arm. The fixture is designed to apply pure shear loading. Since there is no standard for the shear loading mechanism, the fixture was designed by looking at the counterparts in the literature. But, the innovator part of this fixture is the sliding lower part which gives a precise motion on the x-axis in order to avoid the reaction forces at the upper arm of the fixture. By this way, pure shear loading can be applied to the specimen. In the third chapter, the loading procedure and the fixture design are explained in detail. Since the failure is expected as dynamic, high speed monitoring system is used in the experiments, which can capture images up to 1.000.000 fps. The experimental setup is also shown in the method part. Another important aspect related to the experiments is the specimen configurations. Three different basic lay-up configurations are selected for the experiments and the UD and the fabric pre-pregs of the same material are used in the manufacturing process. The manufacturing process was conducted in cooperation with TAI. The measuring systems are also explained in the third chapter. In chapter 4, the results of the quasi-static shear loading experiments are explained. Same experimental procedure is conducted for three different L-beam lay-up configurations, namely, the [0/90] fabric, the [0] UD and the [90/0] cross-ply lay-ups. During the experiments, the load displacement curves are recorded and the subsequent dynamic delamination is captured with a million fps high speed camera. The failed specimens are analyzed under a microscope. It is seen that the layup differences change the failure mechanism in the composites. To look at the failure mechanism of the [90/0] cross-ply specimens, the specimens are manufactured with different ply numbers and inner radii. The results are also shown in chapter 4. Finally, in chapter 5, the experimental results are compared to the discussed the effect of the material, ply orientations, thickness and the inner radius of laminate.

6.2. Conclusions

In this thesis, dynamic delamination of L-shaped composite structures is investigated experimentally for three different lay-ups: [0/90] fabric, [0] UD and [90/0] cross-ply.

The macroscale observations are made which are maximum failure loads, stiffness of the load-displacement curves and load drops (single or multiple) in failure. The mesoscale observations related to experiments are the crack tip speeds, delamination locations and sequence, and the micrographs of failure.

In the experimental work, the crack initiation and propagation in L-shaped parts under quasi-static loading is observed as dynamic. In the load-displacement curves of the experiments, the crack growth corresponds to sudden load drops. The previous studies have been also obtained similar results. However, only the final failure patterns were shown experimentally because the crack initiation happens instantaneously and propagation speeds are high. Therefore, the initial goal of this thesis is to show the details of dynamic failure mechanism with capturing the delamination mechanism with a million fps high speed camera. [0/90] fabric specimens were manufactured and tested under quasi-static shear loading. A single or two delamination growths through the curvature is monitored in tests. From the high speed images, the crack tip speeds are calculated. The first calculated speed (1033 m/s) is already near the Rayleigh wave speed of the material (1224 m/s) and then reaches to the intersonic speed (2401 m/s).

The second goal of this thesis is show failure mechanism difference of different lay-ups. For this purpose, [0] UD and [90/0] cross-ply laminates are tested. In the [0] UD only one load drop is recorded corresponding to the delamination formation. After the load drop, the [0] UD specimens lost all their load carrying capacities. Although the highest maximum loads for the geometrically identical specimens belong to the [0] UD specimen, they have the lowest stiffness values after the delamination formation. In the [0] UD case, a multiple delamination formation that corresponds to a single load drop is observed. An initial crack nucleates in the mid-part of the curved region. Four small cracks are initiated at the end of the curved region, symmetrical with respect to the first crack tips. After these delaminations, multiple small delaminations initiate through the thickness.

In the [90/0] cross-ply experiments, multiple load drops are recorded corresponding to the sequential delamination growth. The lowest maximum loads, compared with the other lay-ups, are recorded in the [90/0] experiments. But, when the failed composite specimens are reloaded, it is seen that the maximum load before the next

load drop reaches to 75 % of the un-damaged specimen's original load carrying capacity in the [90/0] cross-ply case. In the [90/0] cross-ply case, unlike the other layups, a sequential delamination growth is seen corresponding to the multiple load drops. The first delamination nucleates in the 3rd interface, near the inner radius and 13° left of the mid part. This single delamination propagates all the way through, until the end of the first load drop.

The failure mechanism differences are explained by looking at the numerical stress fields of the specimens. In [0/90] fabric and [0] UD cases, the opening stresses which are maximum at the mid-part of the curved region are causing the delamination initiation and propagation. On the other hand, in [90/0] cross-ply case, the longitudinal stress components are maximum at the inner part of the curved region, which are 10 times bigger than the opening stress values, causes the small matrix cracks at the 90° oriented plies. Although the shear and the normal stresses are maximum at different locations, the dominant stress type of this failure mechanism is the longitudinal stress because of the 90° fibers. The small matrix cracks weaken the 90° plies and the delaminations nucleate from these locations, and propagate through the arms.

The next issue of doubt about this different failure mechanism concerns its “repetitiveness”. It is considered that the thickness and inner radius of the specimen are effective on the repetitiveness of the failure mechanism. In order to investigate the failure mechanisms, specimens are manufactured with different thickness and inner radius for [90/0] cross-ply laminate. although, the stiffness, maximum carried loads or load- carrying capacities after failure are change, the sequential delamination growth behavior beginning in inner part of the laminate is not changed.

6.3. Future Work

In the future, the experimental procedure should be fully extended to conduct different configurations of the curved composite laminates. The stiffness variations between the load-displacement curves of the same type specimens will be investigated. In the first step, an analytical solution for 2-D curved composite laminates are conducted by applying shear loading. Then, the solution methods are

extended to the numerical solutions and a 3-D analysis. It is thought that the solution method should be applicable for each different configuration of the composite laminates easily. The experimental results are compared with the numerical modeling. The other types of loadings, such as the axial load, which is parallel to the arm (P) and the moment (M), should be studied experimentally and numerically for the same composite configurations and the failure mechanisms should be obtained. In order to strengthen the curved structure, solution methods should be improved without making it heavier.

REFERENCES

1. Online Etymology Dictionary,
<http://www.etymonline.com/index.php?term=composite>
2. Waterman, P. J., "The Life of Composite Materials", Desktop Engineering Magazine, April, 2007, retrieved from,
<http://composite.about.com/od/aboutcompositesplastics/a/HistoryofComposites.htm>
3. Kopeliovich, D. Carbon Fiber Reinforced Polymer Composites, retrieved from;
http://www.substech.com/dokuwiki/doku.php?id=carbon_fiber_reinforced_polymer_composites, last visited on 02/06/2012
4. Harper, H.C.J.; Composite history, Flight, November 11, 1937. Retrived from; <http://www.flightglobal.com/pdfarchive/view/1937/1937%20-%203093.html>
5. Yancey R., 'Why Composites are Taking Off in the Aviation Industry' Retrived May 22,2012 from <http://insider.altairhyperworks.com/composites-aviation-industry/>
6. Australian Transport Safety Bureau (ATSB) 2007b, *Safety Investigation Guidelines Manual – OH&S (v. 1.00)*, report prepared by B Leyshon, M Squires & M Stallbaum, ATSB, Department of Transport and Regional Services, Canberra, p.89-93.
7. Werfelman, L., 'The Composite Evolution', *AeroSafety World*, March 2007, p.17-21
8. Federal Aviation Administration (FAA) 2006, *Operation of New Large Aircraft Research*, FAA, Atlantic City, NJ, viewed 25 Feb 2008, <http://www.airporttech.tc.faa.gov/safety/patterson2.asp>
9. Niu MCY. Composite Airframe Structures, 1st Edition. Hong Kong Conmilit Press Ltd, 1992, ISBN 962-7128-06-6. Print, pp. 453-490.

10. Freissinet, S. 'Worries about new composite made airplane', Retrieved from <http://www.1001crash.com/index-page-composite-lg-2.html>, last visited on October 2011.
11. Massengill, H., 'Applied Aerodynamics – Commercial Flight', *Aerospace America*, December 2005, p. 7
12. Rakow, J & Pettinger, A, 'Failure Analysis of Composite Structures in Aircraft Accidents', 2006, *Proceedings of the ISASI 2006 Annual Air Safety Seminar*, International Society of Air Safety Investigators (ISASI), Cancun, Mexico.
13. University of Southern California Viterbi School of Engineering, retrieved from <http://composites.usc.edu/projects/automated-defect-evaluation-software-for-ultrasonic-ndi.htm>, last visited on August 2014.
14. Banks, J. 'Obsolete Means Incomplete', *Aerospace Manufacturing*. Retrieved from <http://www.aero-mag.com/features/38/20126/1431>, last visited on 2012.
15. Federal Aviation Administration (FAA) 2006, *Operation of New Large Aircraft Research*, FAA, Atlantic City, NJ, viewed 25 Feb 2008, <http://www.airporttech.tc.faa.gov/safety/patterson2.asp>
16. Niu MCY. Airframe Structural Design. 2nd Edition. Hong Kong Conmilit Press Ltd, 2002, ISBN 962-7128-09-0.
17. Gozluclu B. Modeling of Intersonic Delamination in Curved-Thick Composite Laminates under Quasi-Static Loading. PhD Thesis, March 2014.
18. Boeing 787 Rescue & Firefighting Composite Structure Retrieved April 2013 retrieved from http://www.boeing.com/assets/pdf/commercial/airports/faqs/787_composite_arff_data.pdf
19. Vantinen, A., Strength prediction of composite rib foot corner, M.S. Thesis, Helsinki University of Technology, 2008.
20. Martin, R.H., Delamination failure in a unidirectional curved composite laminate, *Composite Material Testing and Design* 1992;10:365–83.
21. Martin, R.H. and Jackson, W.C., Damage prediction in cross-ply curved composite laminates, NASA Technical Memorandum 104089, USAAVSCOM Technical Report 91-B-009, 1991.

22. Clark N. 'New Cracks Found in the Wings of Some Airbus Planes' Retrieved January 2012 from
http://www.nytimes.com/2012/01/20/business/global/a380-jets-may-get-closer-inspections.html?_r=1&adxnnl=1&adxnnlx=1330264957-YWtr4fefgIvKExc6rrqAtA
23. Sridharan S. Delamination behaviour of composites. CRC Press LLC, 2008.
24. O'Brien T K. Composite Interlaminar Shear Fracture Toughness, GIIC: Shear Measurement of Shear Myth?. ASTM-STP 1330, American Society for Testing and Materials, 1998:3-18.
25. Reeder, J R, Composite Materials Handbook (CMH-17-1F), Vol. 1, Chapter 6, section 6.8.6, 2002.
26. Russell, A J, 'On Measurement of Mode II Interlaminar Fracture Energies', Defense Research Establishment Pacific, Victoria, British Columbia, Canada, Materials DREP Report, 82-0, 1982.
27. Davidson, B. and Sun, X., 'Geometry and Data Reduction Recommendations for a Standardized End Notched Flexure Test for Unidirectional Composites', Journal of ASTM International, 3, (9), 2006.
28. Ratcliffe, J. G., Characterization of the Edge Crack Torsion (ECT) Test for Mode III Fracture Toughness Measurement of Laminated Composites, NASA TM-2004-213-269, September 2004.
29. Lee, S. M., 'An Edge Crack Torsion Method for Mode III Delamination Fracture Testing', J. Comp. Tech. and Research, 15, (3), 193-201, 1993.
30. Li, J, Lee, S. M. Lee, E. W. and O'Brien, T. K. , 'Evaluation of the Edge Crack Torsion (ECT) Test for Mode III Interlaminar Fracture Toughness of Laminated Composites', Jnl. Comp. Tech. and Research, 19, (3), 174-183, 1997.
31. Chang F and Springer GS. The strength of fiber reinforced composite bends. Journal of composite materials 1986;20:30-45.
32. Sun CT and Kelly SR. Failure in Composite Angle Structures Part I: Initial Failure. Journal of Reinforced Plastics and Composites 1988 7:220-232.
33. Wang, A.S.D., 'Strength, Failure and Fatigue Analysis of Laminates' Composites, Engineering Materials Handbook, Vol.1, 1987, pp 236-251.

34. Johnson W.S., *Delamination and Debonding of Materials*, ASTM STP 876, American Society for Testing and Materials, Philadelphia, PA, 1985.
35. Feih S. Shercliff HR. Composite failure prediction of single-L joint structures under bending, *Composites: Part A* 2005 ;36:381–395.
36. Lekhnitskii SG. *Theory of elasticity of an anisotropic body*. Mir Publishers. Moscow. 1981.
37. Kroll, L., Hufenbach, W., A Physically Based Failure Criterion for Laminated Composites. *Mechanics of Composite Materials*, 1999; Vol. 35, No. 4,
38. Wimmer G, Kitzmüller W, Pinter G, Wettemann T, Pettermann HE., Computational and Experimental Investigation of Delamination in L-shaped Laminated Composite Components. *Engineering Fracture Mechanics* 2009;76:2810-2820.
39. Garg AC. Delamination – a damage mode in composite structures. *Engng Fract Mech* 1988;29:557–84.
40. Bolotin VV. Delamination in composite structures: its origin, buckling, growth and stability. *Compos Part B* 1996;27B:129–45.
41. Hild F. *Discrete versus continuum damage mechanics: a probabilistic perspective*. Oxford (UK): Elsevier Science Ltd.; 2002.
42. Gozluclu B and Coker D. Modeling of the dynamic delamination of L-shaped unidirectional laminated composites. *Composite Structures* 2012;94:1430–1442.
43. Zhang J., Liu L., and Wang H., Failure analysis of woven fabric curved laminate with variable thickness, the 19th International Conference on Composite Materials, July 28-August 2, 2013, Montreal, Canada.
44. AMT Airframe Handbook Volume 1 (FAA-8083-31) Ch. 7 Advanced Composite Material Retrieved May 2014 from https://www.faa.gov/regulations_policies/handbooks_manuals/aircraft/amt_airframe_handbook/media/ama_Ch07.pdf
45. Marlett K. Hexcel 8552S AS4 Plain Weave Fabric Prepreg 193 gsm & 38% RC Qualification Material Property Data report. National Institute for Aviation Research, Wichita State University, CAM-RP-20110-006 April 14, 2011.

46. Yavas D. Experimental and Computational Investigation of Crack Growth along Curved Interfaces. M.S. Thesis, Middle East Technical University, 2013.
47. Nettles A.T., Basic Mechanics of Laminated Composite Plates, 1994, NASA Reference Publication 1351
48. Coker D and Rosakis AJ. 'Experimental observations of intersonic crack growth in asymmetrically loaded unidirectional composite plates.' Philosophical Magazine A 2001;81(3):571-595 119.
49. Cooke, John. "High speed photography: a guide to imaging rapid movement and transient events." Retrieved April 7, 2005 from <http://www.hidden-worlds.com/highspeed/index.htm>
50. Personal Communication METKON, 2014
51. Lecture Notes, ME 3701, Materials of Engineering, LSU, Cornell University Retrieved from, <https://www.ccmr.cornell.edu/sites/default/files/facilities%20equipment/Polishing%20Guidelines.pdf>
52. Amadori, M., Design and Development of the New Composite-Metal Mainplane of Dallara T12 Race Car', 2012
53. Personal communication with Burak Gözlüklü, TAI.
54. Hao W., Ge D., Ma Y., Yao X. and Shi Y., Experimental investigation on deformation and strength of carbon/epoxy laminated curved beams. Polymer Testing 2012; 31: 520-526.
55. Kumar S.R., Textiles for industrial applications. CRC Press LLC, 2014.

APPENDICIES

A. MEASUREMENT DETAILS OF EXPERIMENTS

Table A.1 Measurement details of experiments.

	Frame Rate (fps)	Measuring Area (px x px)	Shutter Time (s)	Total Rec Time (s)
$[(0/90)_6]_s$ -F1	350,000	128x88	1/frame rate	2.9
$[(0/90)_6]_s$ -F2	525,000	64x72	1/1000000	4.73
$[(0/90)_6]_s$ -F3	620,000	64x56	1/1000000	5.15
$[(0/90)_6]_s$ - F4-7	465000	64x88	1/1000000	4.4
$[0]_{17}$ - spc1	525,000	64x72	1/1000000	4.8
$[0]_{17}$ - spc2	620,000	64x56	1/1000000	5.2
$[0]_{17}$ - spc3	700,000	64x40	1/1000000	6.4
$[(90/0)_4, \overline{90}]_s$ spc1-7	465,000	64x88	1/1000000	4.4
$[(90/0)_5, \overline{90}]_s$ - all tests	420,000	64x96	1/frame rate	4.4
$[(90/0)_6, \overline{90}]_s$ - all tests	420,000	64x96	1/frame rate	4.4
$[90/0]_{11}$ -all tests	420,000	64x96	1/frame rate	4.4
$[90/0]_7$ -all tests	420,000	64x96	1/frame rate	4.4

Calibration area =250x250 mm

The distance between specimen and camera=785 mm

B. LOAD-DISPLACEMENT CURVES OF EXPERIMENTS

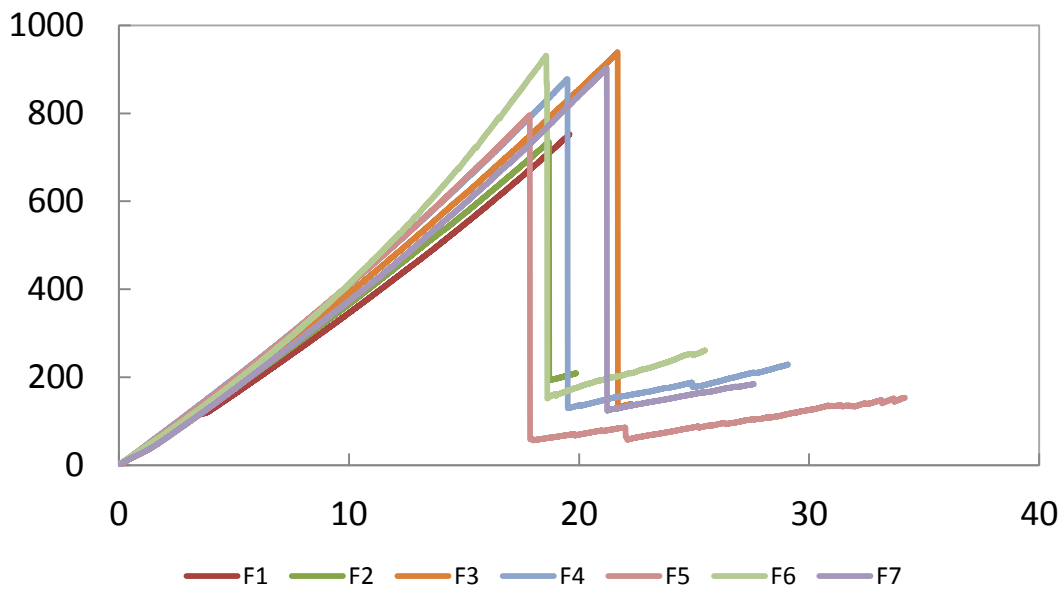


Figure B.1 [0/90] fabric lay-up experiments.

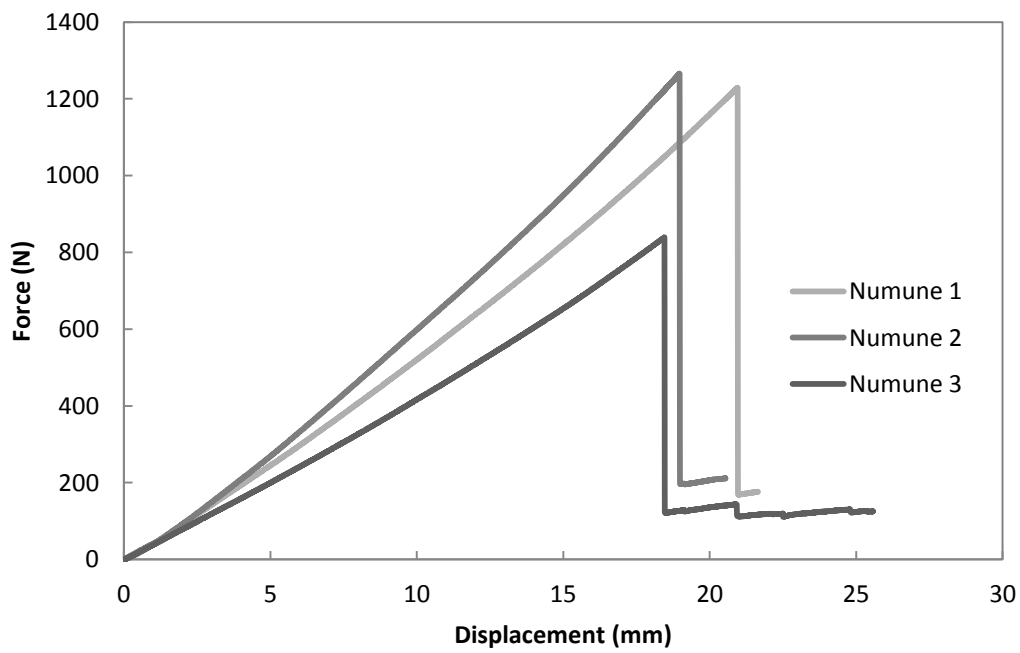


Figure B.2 [0] uni-directional lay-up experiments.

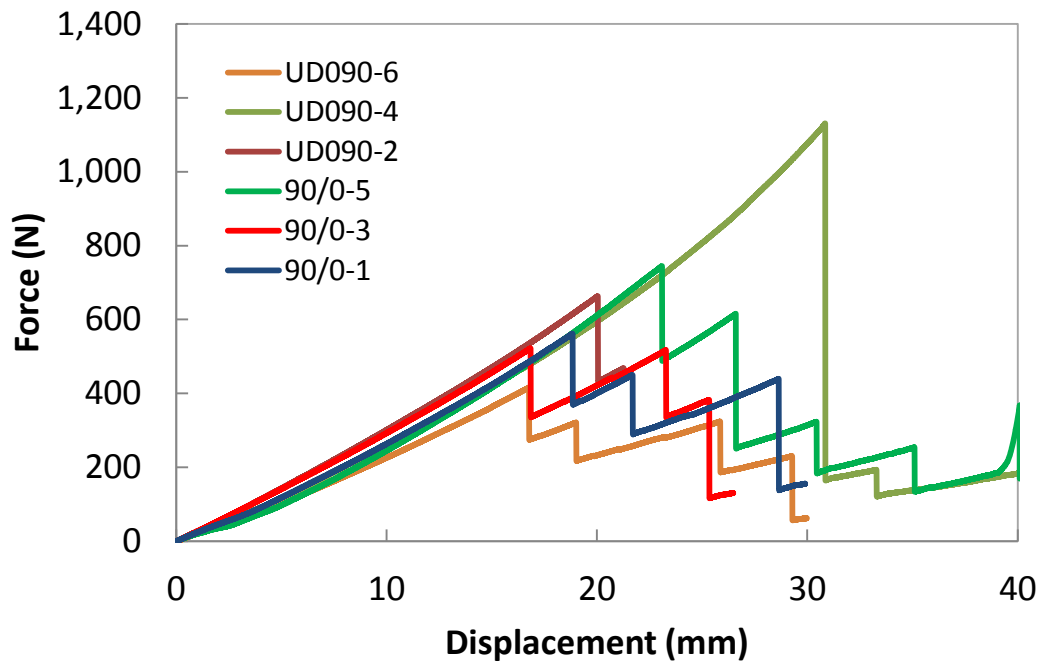


Figure B.3 [90/0] cross-ply lay-up experiments.